

**Optimization of Rotating, Range-gated,
Fanbeam Scatterometer for Wind
Retrieval**

Task 1 Technical Report

Review of the Requirements and Scatterometer Concept

ESA/ESTEC Contract No.: 14383/00/NL/DC
MPBT Shop Order No.: 562S
MPBT Report No.: MPBT-562SR001

Submitted to :
European Space Research and Technology Centre
P.O.Box 299, 2200 AG Noordwijk
The Netherlands
Atten'n: Mr. C.C. Lin

Submitted by:

MPB Technologies Inc
151 Hymus Boulevard
Pointe-Claire, Quebec
Canada, H9R 1E9

October 17, 2000

European Space Agency Contract Report

The work described in this report was done under ESA contract. Responsibility for the contracts resides in the authors or organization that prepared it

Prepared by:

C. Liu and P. Park

MPB Technologies Inc.
151 Hymus Boulevard, Pointe-Claire, Quebec, Canada, H9R 1E9

A. Stoffelen

KNMI
Royal Netherlands Meteorological Institute
Postbus 201, 3730 AE de Bit, The Netherlands

And

V. Wismann

Ifars
Institute for Applied Remote Sensing
Am Josefsberg 2, 79100 Freiburg, Germany

Approved:

Dr. A.K. Ghosh
Director, Space and
Photonics Division

Dr. P.S. Park,
Project Manager

Table of Contents

1. INTRODUCTION.....	5
2. BRIEF SURVEY OF EXISTING SCATTEROMETER (MPBT)	6
2.1 SEASAT, NSCAT AND SEAWINDS.....	6
2.2 ERS SCATTEROMETERS AND ASCAT.....	9
3. REVIEW OF RFSCAT PRODUCT REQUIREMENTS	13
3.1 REVIEW OF NEAR SURFACE WIND USER REQUIREMENT AND APPLICATION	13
3.1.1 <i>Introduction</i>	13
3.1.1.1 WMO Requirements	14
3.1.1.2 Atmospheric Analysis	15
3.1.1.3 Observation Needs and Capabilities.....	20
3.1.2 <i>Near-Surface Wind Requirements</i>	22
3.1.2.1 Horizontal Scale	22
3.1.2.2 Vertical Scale	23
3.1.2.3 Temporal Domain	24
3.1.2.4 Accuracy	24
3.1.2.5 Bias	25
3.1.2.6 Reliability.....	25
3.1.2.7 Data Delivery	25
3.1.3 <i>RFSCAT Application</i>	26
3.1.3.1 Geophysical Relationship.....	26
3.1.3.2 Wind Retrieval and Atmospheric Analysis	29
3.1.3.3 Accuracy	29
3.2 EXPECTED FUTURE SYSTEMS	30
4. REVIEW OF RFSCAT CONCEPT	35
4.1 REVIEW OF THE PROPOSED INSTRUMENT CONCEPT	35
4.1.1 <i>Instrument Concept</i>	35
4.1.1.1 Measurement Geometry	36
4.1.1.2 Instrument parameters	40
4.1.2 <i>Instrument Design</i>	43
4.1.2.1 Baseline Design.....	43
4.1.2.2 Doppler Compensation.....	43
4.1.3 <i>Preliminary Analysis of RFSCAT Performance Issues</i>	44
4.1.4 <i>Preliminary Analysis of System Risk</i>	45
4.1.4.1 Baseline system.....	45
4.1.4.2 Enhancements	46
4.1.5 <i>System Equipment Enhancements</i>	46
4.1.5.1 General	46
4.1.5.2 Equipment Design and Performance	46
4.1.5.3 Potential Enhancements	49
4.2 REVIEW OF SCATTEROMETER PERFORMANCE	55
4.2.1 <i>Literature survey to extend the GMF</i>	57
4.2.2 <i>NRL Airborne Data</i>	57
4.2.2.1 Airborne X-Band Data of the Radio Research Laboratory, Tokyo	57
4.2.2.2 DUTSCAT	58
4.2.2.3 SAXON-FPN	58
4.2.2.4 SIR-C/X-SAR	58
4.2.2.5 HELISCAT	58
4.2.3 <i>Extending CMOD4 to HH-polarisation</i>	59
4.2.4 <i>Extending NSCAT2 and CMOD4H to Polarimetry</i>	64
4.2.5 <i>A first impact study</i>	68
5. DISCUSSION ON CRITICAL ISSUES IN SIMULATION TOOL DEVELOPMENT	82
6. CONCLUSION	88
7. REFERENCES.....	92
8. ACRONYMS.....	96

1. INTRODUCTION

The present technical report describes the results obtained during the Task 1 of the ESA/ESTEC contract titled "Optimization of Rotating, Range-gated, Fanbeam Scatterometer for Wind Retrieval". The objectives of the Task 1 activity are the following:

- Critical review of the scatterometer wind product requirements and suggestions for improvements,
- Comprehensive review and analysis of the scatterometer concept
- Consideration of system enhancements, review of system feasibility and risk

As an introduction to scatterometer and its techniques, a brief survey of existing scatterometers is given in Section 2. In Section 3, a review of RFSCAT product requirements is presented which is based on the requirements provided in Attachment II of the SOW. The rotating fanbeam scatterometer instrument concepts are reviewed in terms of performance, feasibility, risk as well as possible enhancements in Section 4. Critical issues in simulation tool development as an introduction to the Task 2 is discussed in Section 5 followed by Conclusions in Section 6.

2. Brief Survey of Existing Scatterometer (MPBT)

2.1 SeaSat, NSCAT and SeaWinds

The first scatterometer in space was the NASA SeaSat-A Scatterometer System, SASS, that flew in 1978 for three months. SASS had four antennae, two on both sides of the satellite, as depicted in Figure 2.1. Each set of two antennae covered a swath; one to the right of the subsatellite (ground) track and one to the left. In the horizontal plane, the fore and aft beams were pointing at respectively 45° and 135° with respect to the ground track. A location in the swath was first hit by the fore beam, and a few minutes later by the aft beam. Thus, each node in the swath revealed two backscatter measurements obtained with a 90° difference in azimuth. Figure 2.2 illustrates the analysis of two such measurements. For each measurement it shows the wind speed solution as a function of all possible wind directions. Given the basic harmonic wind direction dependency of the backscatter signal, four solutions exist in this general case. This ambiguity poses a strong limitation to the usefulness of the SASS wind data, and extended manual ambiguity removal efforts were needed to obtain an acceptable wind product [*Peteherych et al.*, 1984]. With this product the usefulness for NWP could be shown (see, e.g., *Stoffelen and Cats*, 1991).

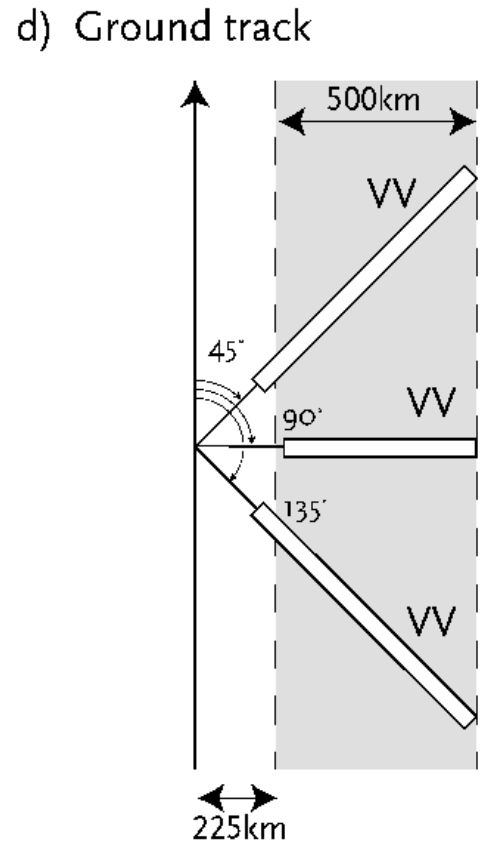
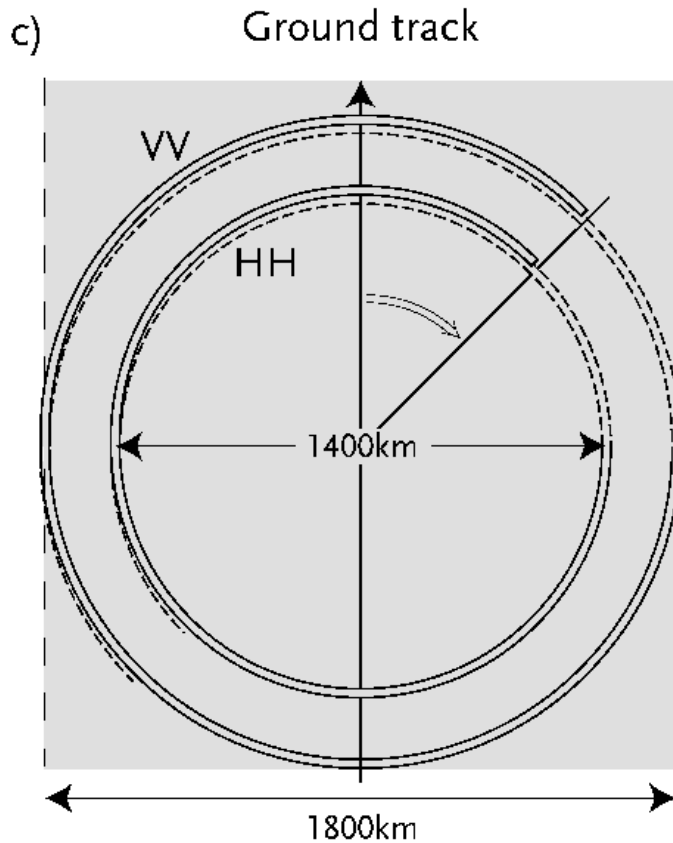
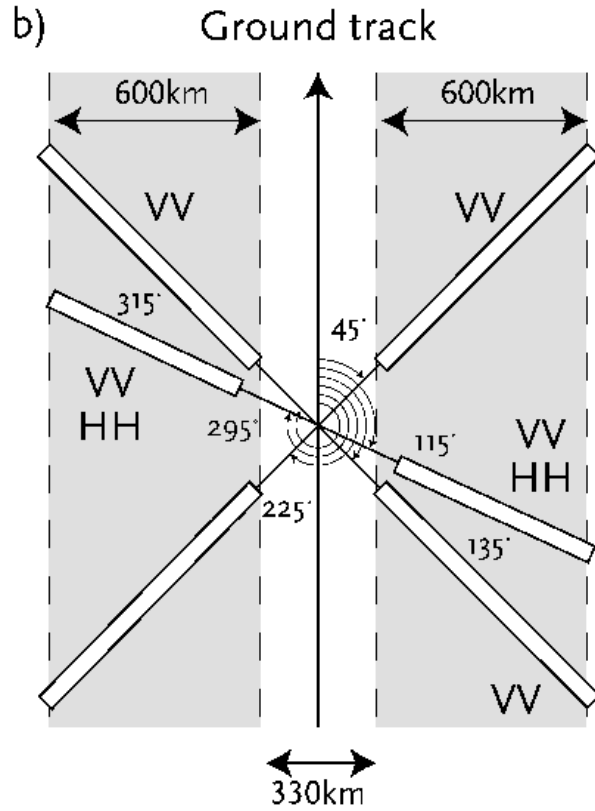
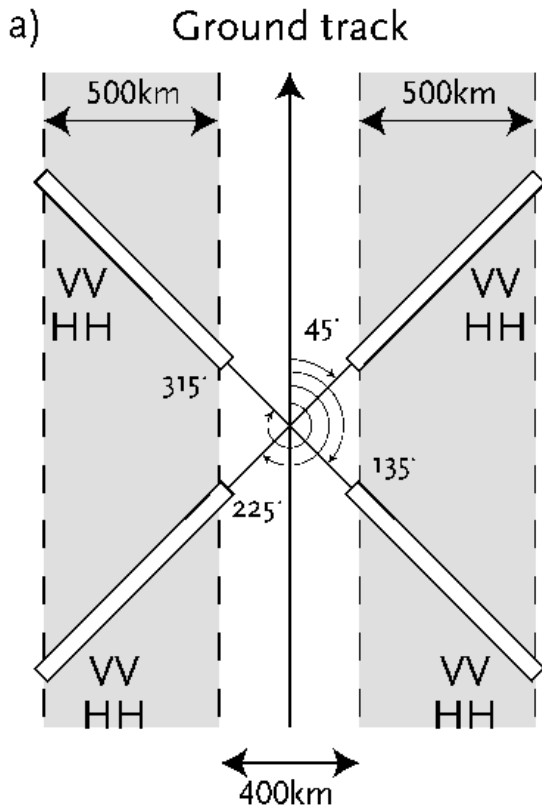
In a follow-on design, i.e., NSCAT, a beam was added in between the fore and aft beams to both sides of the swath, as shown in Figure 2.1. The polarization of the microwave radiation emitted and received by the mid beam was both vertical, called VV, and horizontal, called HH. For the other antennae and instruments only VV polarization is used. For HH polarization, the relationship between backscatter and wind differs from VV, and as such the HH polarization provides useful complementary information, in particular on wind direction. The addition of an antenna with two polarizations makes that at each location in the swath four independent measurements are available. The two additional measurements help resolve a unique wind vector solution. However, an azimuth direction of the mid beam precisely in between the azimuths of the fore and aft beams would have better sampled the harmonic wind direction dependency. This was not done for technical reasons.

NSCAT was mounted on the Japanese Advanced Earth Observation Satellite, ADEOS. After nine months with useful NSCAT data, at the end of June 1997, the Japanese space agency, NASDA, lost control of the ADEOS after a complete power loss. This dramatic event has been a severe set-back for Earth Observation, and scatterometry in particular.

QuikSCAT, which is a quick recovery mission after NSCAT with the SeaWinds instrument on board was launched in June 1999. SeaWinds is the first scanning scatterometer as depicted in Figure 2.1, featuring a VV and HH polarisation pencil beam. A scanning scatterometer accommodates a broad swath. However, a disadvantage of such a concept is that at the extreme ends of the swath, the earth surface is only illuminated from a single azimuth direction. Moreover, in the middle of the swath, at the so-called subsatellite track, the ocean is only illuminated from two exactly opposite directions. The limited azimuth sampling means that wind direction can only be poorly resolved at these locations. Fortunately, the total QuikSCAT swath width of 1800 km guarantees that the full wind vector can be determined accurately over a large range across-the swath.

ADEOS-II will also carry the SeaWinds scatterometer and is planned for launch in early 2002.

SASS, NSCAT, QuikSCAT, and SeaWinds use a microwave wavelength of 2.1 cm (14.6 GHz frequency; denoted Ku-band). This frequency is affected by atmospheric attenuation due to rain. Furthermore, rain droplets hitting the ocean surface distort the gravity-capillary waves, and may complicate the backscatter-wind relationship. Latter effects become substantially smaller for a higher wavelength. To avoid such effects and focus on reliable wind data below all cloud, the ESA scatterometers on board the ERS-1 and ERS-2 satellites, and the ASCAT scatterometer planned on the European METOP satellite series use a wavelength of 5.7 cm (5.3 GHz frequency, denoted C-band).



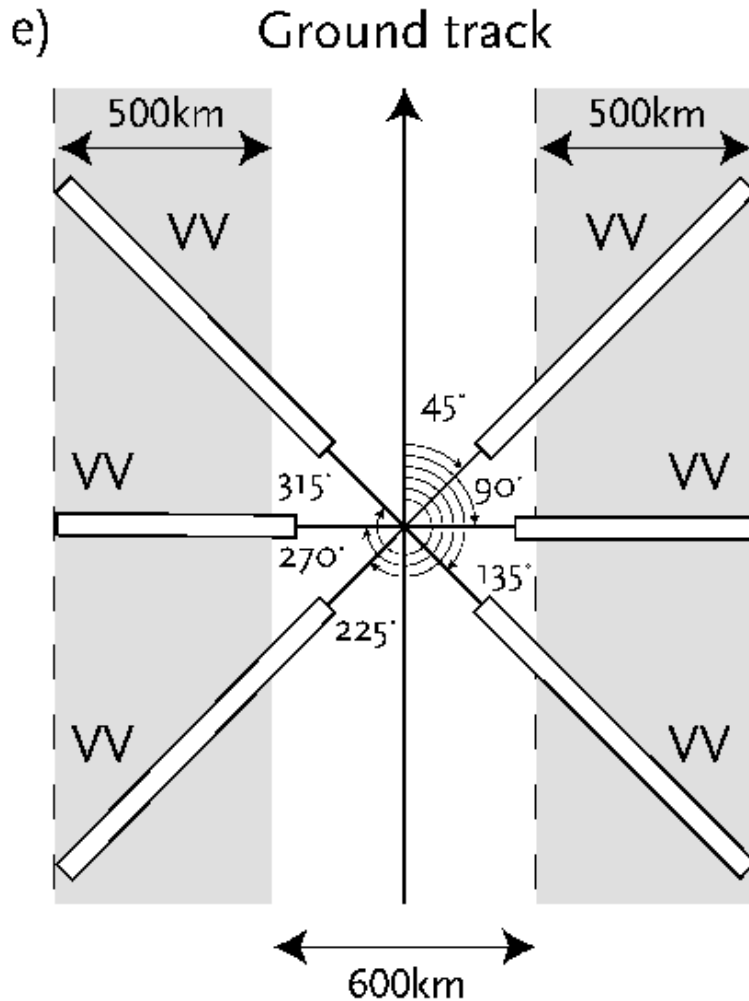


Figure 2.1: Sketch of the surface microwave illumination pattern for a) SeaSat, b) NSCAT, c) SeaWinds, d) ERS-1 or ERS-2, and e) ASCAT. The grey areas denote the swath and the arrow the direction of the ground track (Stoffelen, 1998).

2.2 ERS Scatterometers and ASCAT

The first ESA remote sensing satellite, ERS-1, was launched on 17 July 1991 into a polar orbit of 800 km height. In 1995 the ERS-1 follow-on, ERS-2, was launched. The ERS-1 and ERS-2 scatterometers, which are identical and denoted SCAT here, each have three antennae, that illuminate the ocean surface from three different azimuth directions, as shown in Figure 2.1. A point on the ocean surface will first be hit by the fore beam, then by the mid beam and at last by the aft beam. In Stoffelen (1998, Chapter II) it is shown that this measurement geometry generally results in two opposite wind vector solutions. In Chapter V of Stoffelen (1998) it is discussed how a unique wind vector solution may be selected from the two optional ones. The SCAT wind product has a high quality and shows small scale meteorological structures, as shown in Figure 2.3.

A limitation of the SCAT is its coverage. In contrast to the NASA Ku-band scatterometers, SCAT only views at one side of the subsatellite track. Moreover, the microwave source is shared with a SAR instrument, so that the operation of SCAT is often not possible in meteorologically interesting regions (e.g., in the Norwegian Sea). With ERS-1 and ERS-2 two working SCAT instruments have been in orbit for a few years, but for different reasons only operated simultaneously for 8 months (in shared mode with ERS SAR). Tandem ERS-1 and ERS-2 SCAT numerical weather prediction impact experiments by ECMWF [*Le Meur, 1997*] and KNMI [*Stoffelen, 1997*] have shown that two scatterometers have more than twice the value of one.

The ASCAT (advanced) scatterometer due on METOP, which is planned for launch in 2003, will use the same radar wavelength as SCAT, but will be double sided and have a dedicated microwave source. Figure 2.1 depicts the measurement configuration of ASCAT and Figure 2.4 shows the coverage that would be obtained by ASCAT over a period of 12 hours. The interpretation of ASCAT will benefit much from the knowledge gained during the ERS missions. The extreme outer part of the ASCAT swath, however, corresponds to microwave incidence angles that were not available in the SCAT swath, and may need further investigation.

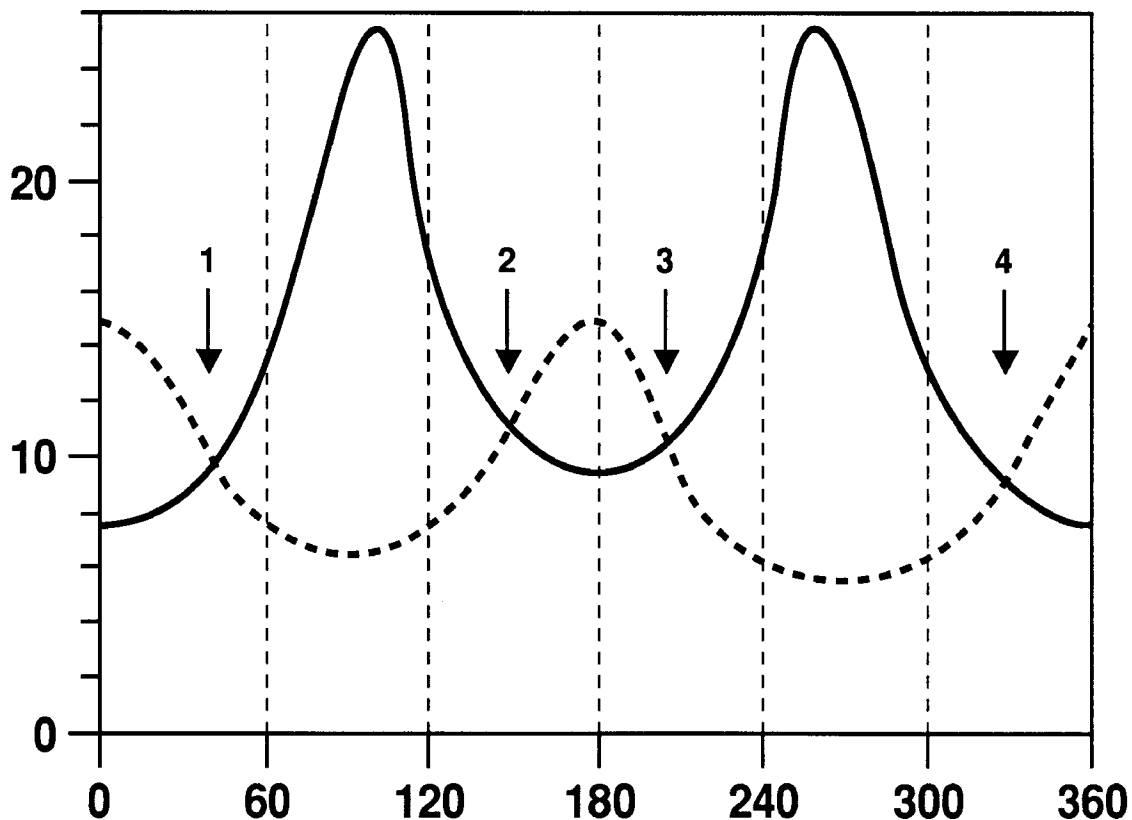


Figure 2.2: Wind speed as a function of wind direction for a fore and aft beam measurement of backscatter from SASS (Stoffelen, 1998).

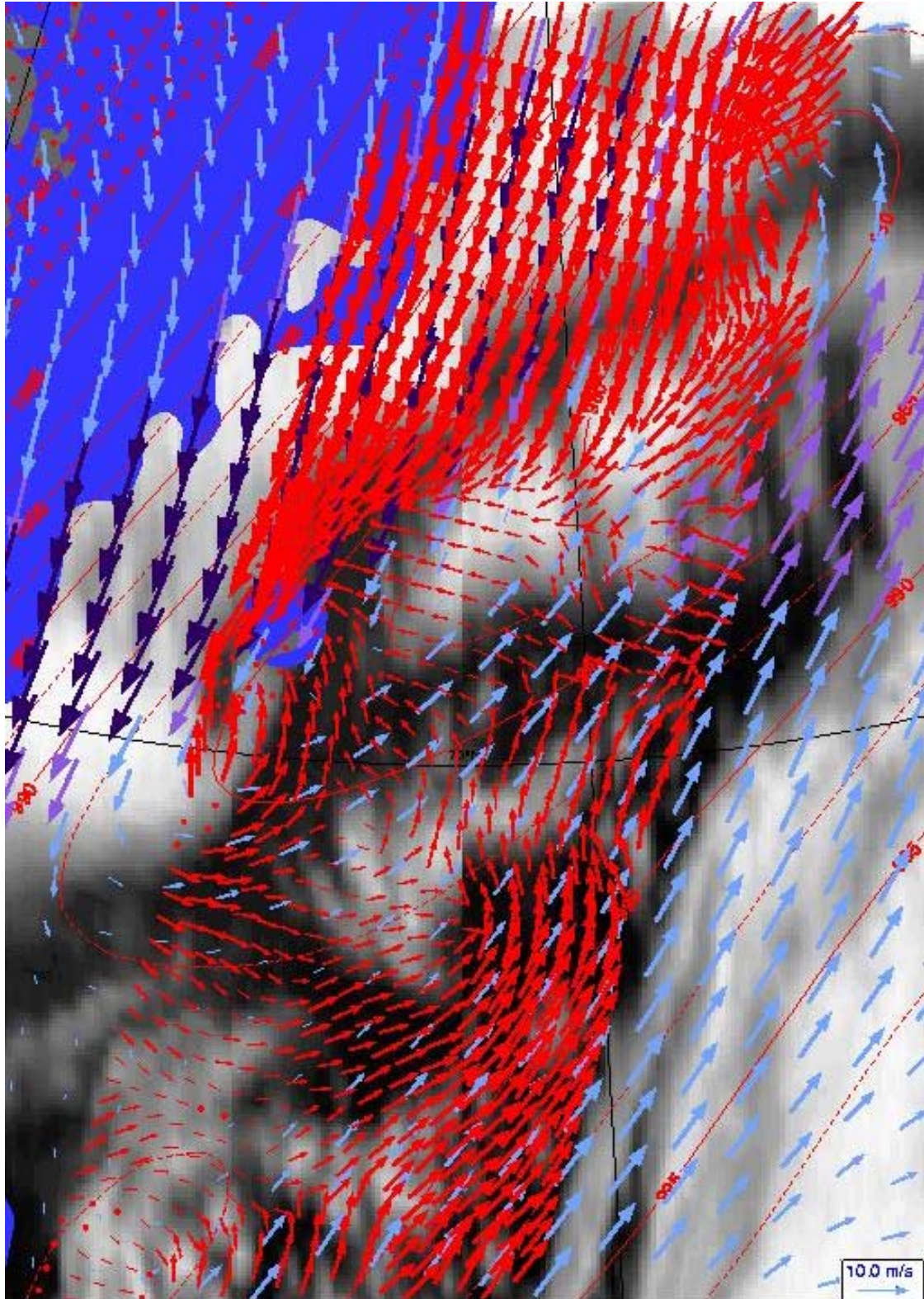


Figure 2.3: High quality ERS product in red with much spatial detail in an area close to the ice edge (blue) where cold air flow from the north interacts with warm and humid air from the south. In the background a METEOSAT infrared cloud image (grey) coherent with the SCAT data is shown, and HIRLAM analysis winds (blue) with much less spatial detail (KNMI, 2000).

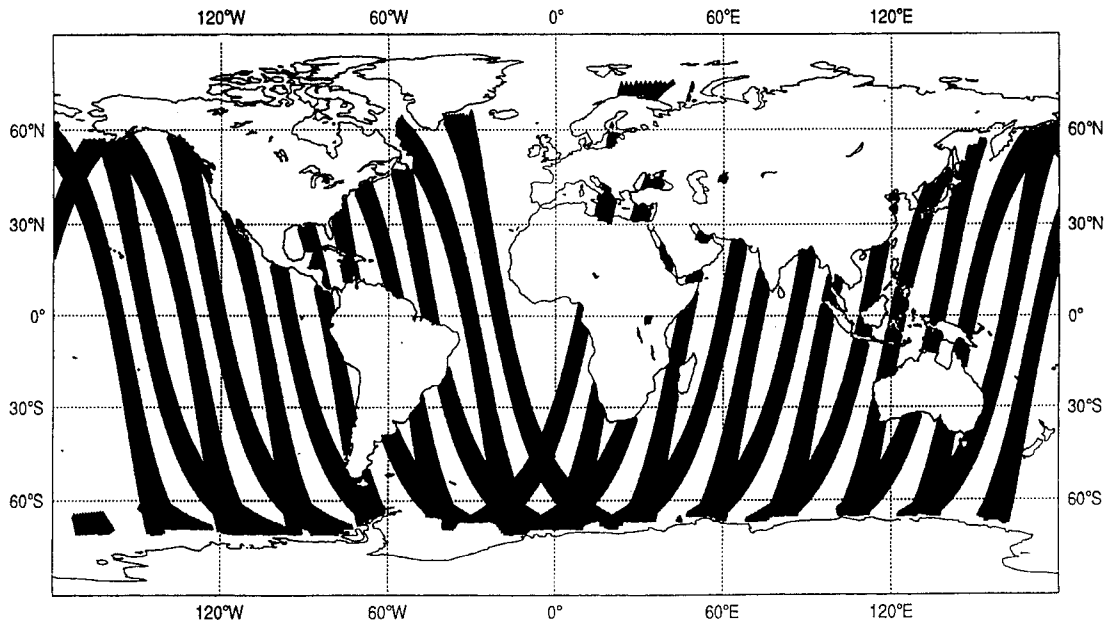


Figure 2.4: ASCAT swath coverage after half a day (Stoffelen, 1998).

3. Review of RFSCAT Product Requirements

3.1 Review of Near Surface Wind User Requirement and Application

3.1.1 Introduction

Many meteorological observations are contained in the current Global Observing System, GOS. Nevertheless, the European Space Agency, ESA, is investigating a mission to further extend the capabilities of the GOS by a rotating fan-beam scatterometer, RFSCAT, measurements. RFSCAT may provide near-surface wind data over the oceans, and ancillary information over land or ice surfaces. In this document we assess the requirements for these data, the way such data could be modelled and ingested, and merged with the existing information on the atmospheric and oceanic state. The WMO publishes documents on the capabilities of the current GOS and the requirements for improving meteorological analyses (WMO, 1996, 1998). It is stated in these documents that near-surface wind data temporal and spatial coverage is lacking in the current GOS as detailed below. Here we discuss this in the light of existing and future scatterometer missions (ERS SCAT, SeaWinds on QuikSCAT, SeaWinds on ADEOS-II, and ASCAT on METOP/EPS), and the experience with their assimilation in meteorological analyses.

The atmospheric analysis problem is briefly described in order to introduce the discussion on requirements. This is, from an understanding of the data assimilation procedure, remaining limitations are summarised and an assessment is made of how RFSCAT can overcome these limitations. Then, observation capabilities and needs are evaluated to be able to summarise what remains unknown. Requirements on, e.g., accuracy, reliability, and temporal and spatial coverage are derived from these unknowns. Possible additional parameters from RFSCAT, such as wind sub-footprint variability or wave parameters, are briefly reflected upon as well.

	Global analysis		Nowcasting	
	Wind vector (ms^{-1})		Wind vector (ms^{-1})	
	Min	Max	Min	Max
Sampling (km)	50	250	5	50
Sampling (hour)	1	12	0.25	3
Max. Delay (hour)	1	4	0.25	1
Accuracy	0.5	3	1	5
Confidence	High		High	

Table 3.1: WMO requirements for near-surface wind for two application areas (WMO, 1998).

The meteorological observations and models that exist and help in defining the near-surface wind conditions are used synergistically in atmospheric data assimilation systems that provide comprehensive analyses. In principle, any observation that can be expressed as a function of the analysis variables, and of which the error properties are known can be assimilated. Empirical models can be derived to establish or verify the precise functional dependencies. However,

problems of non-linearity in combination with (geophysical) uncertainty can complicate the application of new observing systems as detailed later. Issues such as empirical tuning, inversion, Quality Control (QC), and biases, are then discussed, since these may be particularly relevant for RFSCAT.

3.1.1.1 WMO Requirements

The WMO issues critical reviews on the capabilities of and requirements for the GOS, including satellite capabilities and requirements (WMO, 1998). Under the auspices of the WMO also the ocean (GOOS) and climate (GCOS) GOS are evaluated. These critical reviews are followed by a statement of guidance that draws out key issues for several application areas, amongst which NWP and synoptic meteorology. The WMO states that “Surface wind measurements are provided by both passive and active microwave instruments. Passive imagers provide an acceptable coverage but provide information only on wind speed. The current scatterometers provide direction information also, but only with marginal coverage due to 12-hour repeat cycles and narrow swaths. The accuracy is acceptable for NWP. Planned instruments will have better coverage. There is no redundancy in the present system and there may be a complete loss of data before the launch of METOP.” It must be noted however that passive sounders provide acceptable wind speeds in fair weather. In the more dynamic and interesting weather, where often cloud or rain occurs, the interpretation of wind speed from passive measurements is less accurate. For the area of synoptic meteorology the WMO states “Wind vector at the ocean surface, as derived from scatterometer data, are also important for detecting small-scale features and help with providing advice to marine users.” In this document a further analysis is provided of how current and planned satellite capabilities, i.e., in particular scatterometers, meet the near-surface wind requirements. From this we conclude that current and planned scatterometers provide:

- Wind vector quality;
- Spatial consistency; and
- Continuity from METOP onwards,

but lack:

- Coverage.

These issues have also been addressed at a recent ESA/EUMETSAT workshop on “Emerging scatterometer Applications” (ESA, 1999). For example, at this meeting a dedicated tropical cyclone mission was proposed that would appropriately sample their life cycle and allow accurate forecasts.

In WMO (1998) we find the requirements for the near-surface wind (at 10-m height) as provided in table 1. Minimum requirements are such that these at least have to be met to have impact on the application under consideration. On the other extreme, capabilities beyond the maximum requirement are thought to be not very effective. For global NWP both wind vector and wind speed requirements are specified by the WMO, but only the wind-vector requirement is specified here since this is the most general. Wind speed requirements can be derived from wind vector

requirements by transition of a Cartesian to a polar co-ordinate wind vector representation system. Wind vector requirements are specified for global NWP, regional NWP, synoptic meteorology, and nowcasting. From these the global NWP and nowcasting requirements are the most diverse and repeated in the table. For nowcasting the time and space requirements are much more stringent, but at a relaxed accuracy requirement.

In the tropics major uncertainty remains on the atmospheric circulation. Wind observations are of major importance to define the fluxes of humidity and heat in the tropics, but yet insufficient near-surface wind observations are available here. Processes at various scales, relevant to climate studies, are thus not well-defined. Climate studies often rely on meteorological analyses (ERA15, ERA40, NCEP) and for many studies requirements apply similar to those in NWP. However, for the study of some (local) processes also high-resolution requirements exist, particularly in the coastal areas. A question remains how improved coverage near-surface wind data can improve the spatial representation of meteorological analyses. However, since, the general requirements for climate analysis and monitoring are very similar to those for weather prediction, we will focus on the Numerical Weather Prediction, NWP, requirements in this document. NWP skill depends critically on the quality of atmospheric flow analysis.

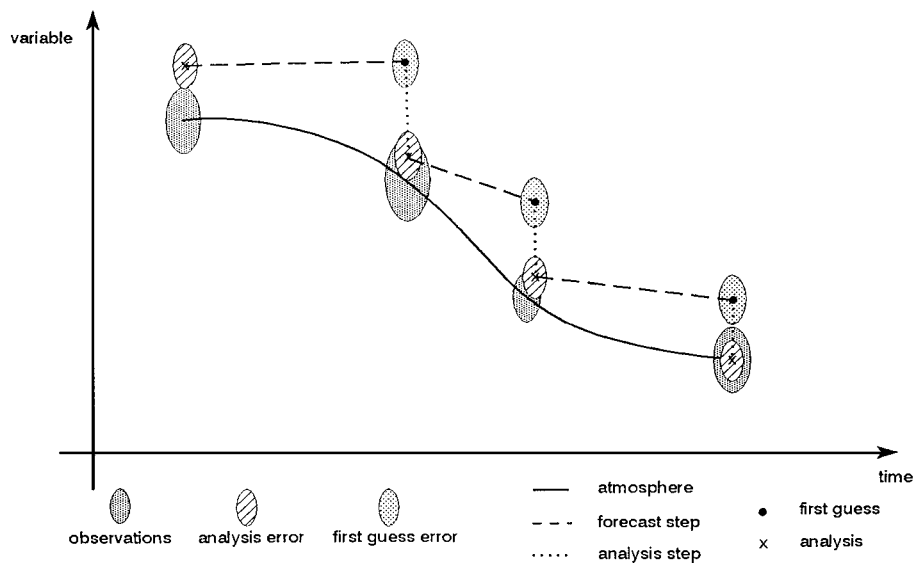


Figure 3.1: Data Assimilation.

Obviously, the observations that are needed in near-real time must have high confidence and usually monitoring and Quality Control (QC) schemes are implemented before data are used operationally in the meteorological community. The above requirements can be further clarified by a discussion of the meteorological analysis problem (Stoffelen, 1998).

3.1.1.2 Atmospheric Analysis

Since a long time it has been realised that a dense GOS is a prerequisite for providing accurate weather analyses and thus forecasts. Moreover, atmospheric flow analyses form a basis to

monitor and understand climate processes. So, how is the information contained in the GOS projected into a spatially and temporally consistent atmospheric state?

Figure 3.1 illustrates the process of data assimilation. The vertical axis represents the atmospheric state. The atmospheric state is usually discretised on a 3D grid. The ECMWF global model has an effective grid distance (sampling) of 60 km in the horizontal and about 500-1000 m in the vertical. This is compatible with many, also regional, numerical weather prediction (NWP) models. A sample of the atmosphere has thus substantial spatial dimensions and only sample-mean quantities are analysed and represented in a NWP model. The NWP model first guess (typically a 6-hour forecast) is not perfect and data assimilation schemes somehow estimate its error size and error structure. Atmospheric circulation models describe the evolution of the atmospheric state. Its chaotic behaviour causes small-scale uncertainties to grow fast in amplitude and size, i.e., like unstable small-scale atmospheric perturbations. Moreover, the NWP model may under- or overestimate atmospheric developments. It is clear that observations are needed to determine the precise atmospheric dynamics. The observations obviously follow the atmosphere, but may contain detection or processing (interpretation) uncertainties and be in a different spatial and temporal representation than the NWP model variables (vertical axis). Note that the first guess contains information on pasts observation, which are, after incorporation into the analysis, projected forward in time by the atmospheric circulation model.

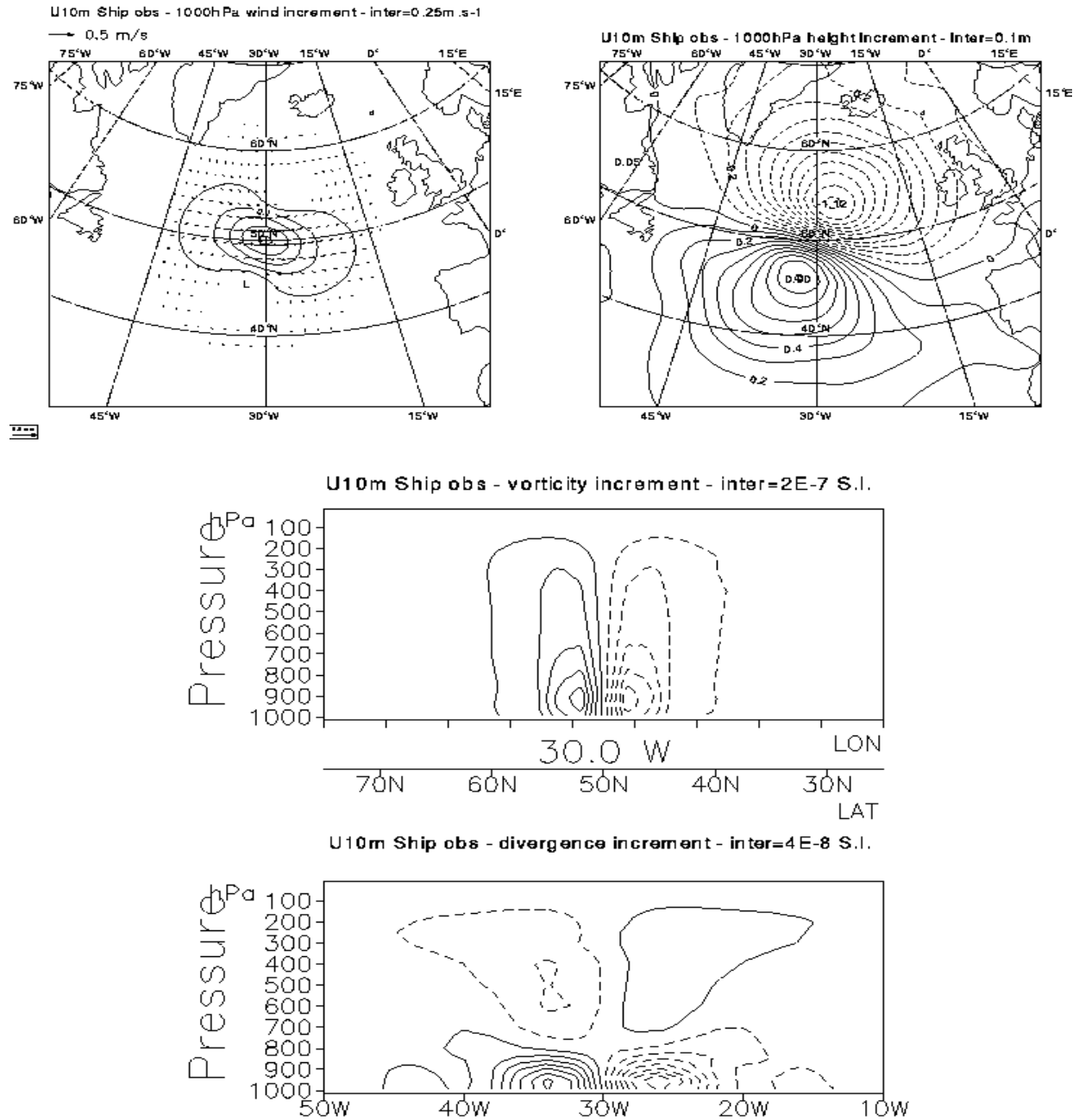


Figure 3.2: Structure of increment due to a ship wind observation at a height of 1000 hPa. The wind increment is directed towards the east and inflicts a relatively broad wind structure along the increment direction (longitudinal) and a smaller one along the transverse direction (meridional; top panels), but where a turning away from the westerly increment is observed due to the surface friction (Ekman spiral). The increment is balanced with a vorticity and divergence structure of which a vertical cross-section is provided in the lower two panels respectively (Courtesy Erik Anderson, ECMWF).

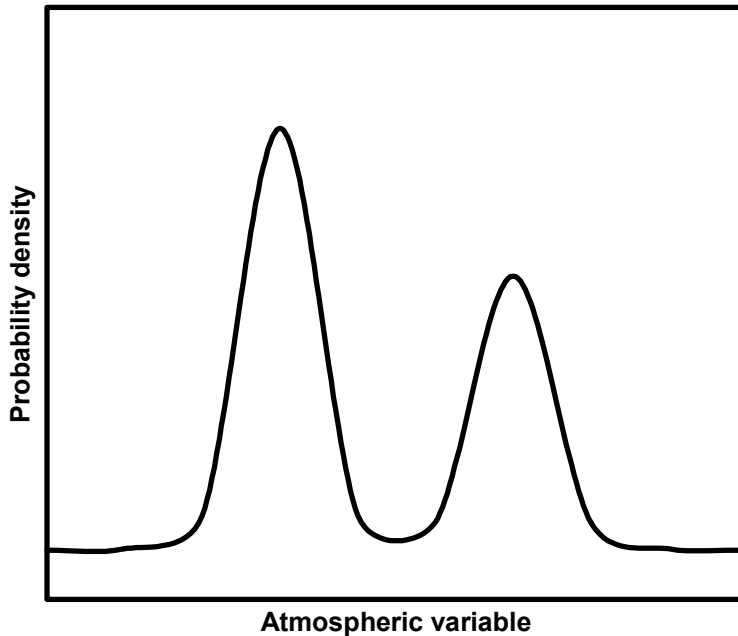


Figure 3.3: The probability density of an atmospheric variable given a meteorological measurement. In a variational analysis the derivative of this probability with respect to the atmospheric control variable determines the impact of the observation in the analysis. The measurement has no impact on the final analysis when the control variable resides in the flat part of the curve (no gradient); in this case the observation is effectively rejected.

The analysis step of the data assimilation cycle combines the knowledge on the atmospheric state from observations and first guess. It maximises the probability of the atmospheric state, given the current observations and the first guess, where the atmospheric state is varied until the probability is maximal (Lorenç, 1986; Courtier, 1996), thus compromising the current observations and the first guess. So, if at a particular location the observation and the first guess disagree, then the model state is adapted, such that a more likely state results. The amplitude of the modification depends on the estimated error covariance of the observation relative to the estimated error covariance of the model. The lower the estimated observation error is, the more impact it has. In order to predict the first guess error, the expected analysis error is computed and projected forward in time to match the first-guess lead time. The errors of the observations and the first guess are by approximation independent.

From statistical studies (e.g. Hollingsworth and Lönnberg, 1987) it is well known that errors in the first guess are spatially correlated. The analysis includes a spatial filter consistent with these error correlation scales. Moreover, errors in the mass (pressure, temperature) and wind fields are in geostrophic balance approximately, which suggests that a multivariate analysis is necessary. This means that mass observations impact the wind field and vice versa, through the geostrophic balance. Examples of the first-guess multivariate spatial error structure are given in Figure 3.2. The vertical depth is relatively small which prevents the vertical projection of surface data into the free atmosphere. This means that surface data alone can not provide an accurate 3D

tropospheric analysis. On the other hand, upper air data does not define the surface flow too well, and a complement of surface and upper air data is needed for an appropriate analysis. NWP model wind errors are lateral in nature and small-scale in the transverse direction, typically 250 km, but slightly depending on latitude and height.

Any observation that can be simulated from the NWP-model atmospheric state can be assimilated in principle after assessment of its error covariance properties. In the multivariate analysis, the wind vector variable is decomposed into two independent horizontal wind components. These two components may be taken relative to an instrument line of sight, LOS. The provision of only one wind component, or of two components with different accuracy, is thus of no limitation to the data assimilation process, just as it is no problem to assimilate a temperature measurement without a wind measurement, or with one of arbitrary quality. A measurement of any one variable leads to a balanced impact on all assimilation variables. If many variables are observed, the most likely compromise is computed.

In many observing systems large random errors can occur during the measurement process, data read-out, or transmission. In other occasions, e.g., anomalous sea state, a measurement is not representative of the atmospheric model state (wind). Traditionally these errors are termed gross errors and detected in a Quality Control step prior to the analysis. The threshold for acceptance depends on the observing system and more specifically on its probability of producing gross errors.

However, for scatterometer data the internal consistency of the data is used for QC prior to the analysis. This QC step has the main advantage that it is independent of the NWP model state.

In variational analysis it is possible to merge the QC step and the analysis step in a fundamental way. Figure 3.3 illustrates this. The fundamental information needed on a meteorological observation is the probability of the atmospheric state given a measurement value. At any point, the analysis will seek a state of high probability using the gradient of the total probability with respect to the atmospheric state. If the most likely atmospheric state resides in an area where an observation probability gradient is zero, then this particular observation does not contribute to the total gradient and has no impact on the analysis, i.e., the first guess state is identical to the analysis. This happens when the first guess is equal to the observation, but also when the observation is effectively rejected because it is too far from the first guess. The probability of (a) measurement(s) given the atmospheric state is used to construct a so-called observation operator for each type of observation. The relationship between measurements and atmospheric state may be non-linear or even ambiguous. In that case the cost function has to be specified carefully such that the observations do not cause a bias in the analysis (Stoffelen, 1998, Chapter 6).

RFSCAT would measure ocean-scattered power at a set of particular azimuth direction and other geometrical parameters. This quantity depends in a non-linear way on both the wind components, or on wind speed and direction, as for existing scatterometers. For these scatterometers, retrieved winds are assimilated rather than backscatter measurements (Stoffelen, 1998), because of the noise transformation in the non-linear projection from wind to backscatter. If backscatter was assimilated this transformation would implicitly be used in order to represent the first guess wind error as an uncertainty in the simulated backscatter. The non-linear

transformation of a normal distributed uncertainty in the wind, gives rise to systematic bias effects which depend on both wind speed and direction and measurement geometry. Since the backscatter measurements are relatively accurate, the non-linear transformation is much less detrimental and good quality wind retrievals with normal error characteristics result (Stoffelen, 1998). However, as depicted in Figure 3.3, the observed information is ambiguous. In a following section we come back on the issue of ambiguity, non-linearity and uncertainty.

Moreover, a measurement may depend on more than one variable of the atmospheric state. If the observation operator $H(\mathbf{x})$ determines the functional dependency of the measurement y on the analysis state vector \mathbf{x} , then $y - H(\mathbf{x}_B)$ is the innovation with respect to the first guess state \mathbf{x}_B . The inverse of the derivative of H with respect to \mathbf{x} , $[H'(\mathbf{x})]^{-1}$, then determines the effect of the innovation on the atmospheric variables. For RFSCAT measurements the procedure of data assimilation is similar to the one described above.

3.1.1.3 Observation Needs and Capabilities

It turns out that wind rather than mass is the determining factor at the unresolved scales (250 km). Figure 3.4 illustrates this. Moreover, the relative importance of wind and mass observations varies with latitude, such that at the equator wind is the all-dominating factor (ESA, 1996, 1999).

Equatorial humidity convergence and momentum and heat exchange processes critically depend on a proper definition of the atmospheric flow. Climate process studies, e.g., to understand the El Niño Southern Oscillation (ENSO) phenomena, include atmospheric dynamics, such as Westerly Wind Bursts (WWB) (CLIVAR, 1998), that are not resolved by the wind measuring capability of the current GOS.

Figure 3.5 shows an overview of the current GOS. Many observing systems are available, but more uniform time and space coverage would be very helpful. Many observing systems observe only aspects of the atmospheric mass distribution, and do not provide direct wind information. Table 3.1 provides a synthesis of current needs in atmospheric near-surface wind sensing.

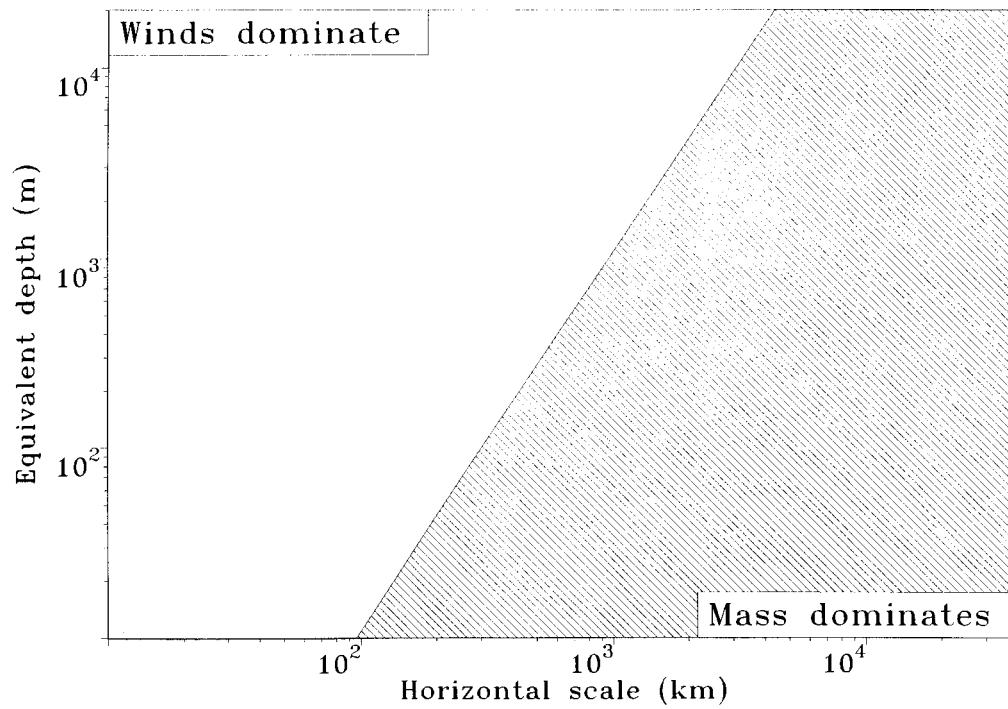


Figure 3.4: The Rossby radius of deformation versus atmospheric depth for a latitude of 45 degrees. For scales larger than the Rossby radius the mass field dominates the dynamics, whereas for smaller scales the wind field is more relevant (ESA, 1999).

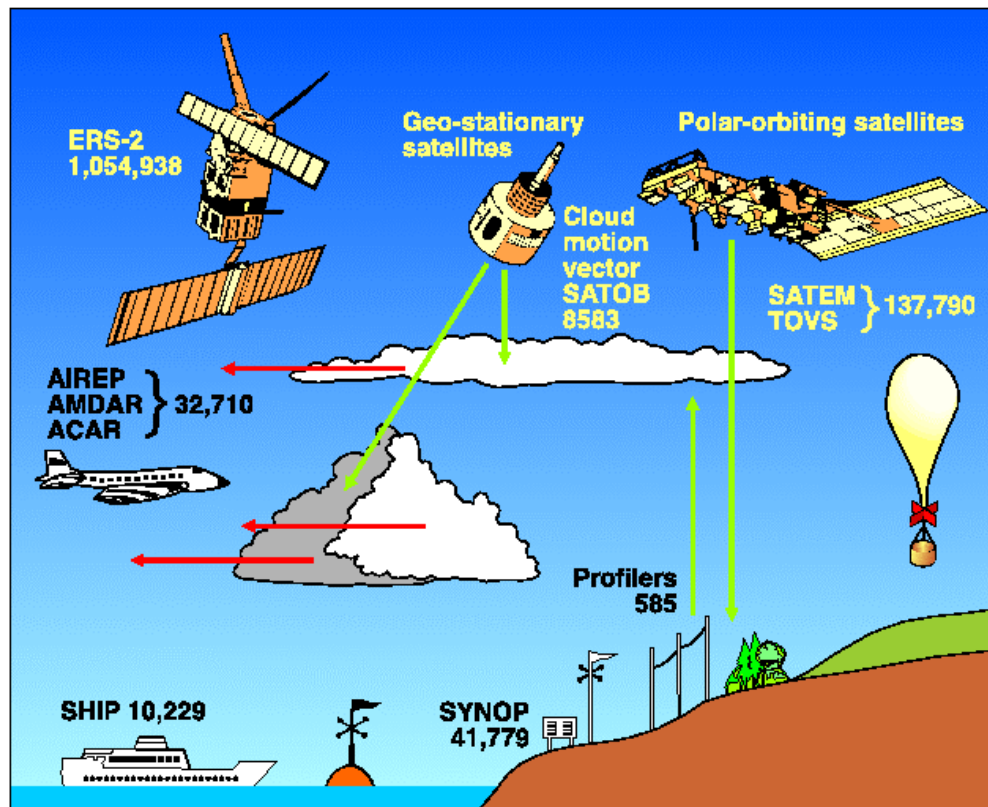


Figure 3.5: Global observing system (courtesy ECMWF).

3.1.2 Near-Surface Wind Requirements

Now that we have discussed the principle need for wind data, the current GOS, and how meteorological data assimilation works we quantify the needs for improved atmospheric flow analysis. The parameters provided in table 1 are discussed in more detail.

3.1.2.1 Horizontal Scale

Global Modelling

The horizontal scales resolved depend on the current GOS and on the data assimilation methodology. Although Global Circulation Models, GCMs, and analysis methodologies show an evolution, it is noted that the spatial extent of the horizontal error structures is mainly determined by the density of the GOS. If a much denser observation network were available then smaller scales would be resolved. In the previous chapter it is argued that 3D wind measurements are required for improving the subsynoptic scale analysis. It is difficult to achieve this with the supplementary observation types that are foreseen, and it is not expected that the spatial extent of these functions will change dramatically in the coming decade. Currently, the transverse wind correlation distance of the structure functions (see Figure 3.2) is roughly 250 km (half-width

half-maximum). One observation provides information on the error of the model state in a spatial context of 250 km, and, consequently, observation information on the model atmospheric state is independent when observations are at least separated by 250 km. On the other hand, observations at much closer distances than 250 km oversample the model state and contribute in an ineffective way to an improved model state (\sqrt{N} law). Currently, scatterometer data are assimilated at 100 km resolution. RFSCAT measurements will be quite uniformly distributed in time and space and thus effectively improve the model state.

Experiments with ERS, tandem ERS and NSCAT scatterometer winds at ECMWF (Le Meur, 1996), KNMI (Stoffelen and Beukering, 1997), and GSFC (Atlas et al., 1998) have shown that an increased density of the near-surface winds network leads effectively to improved atmospheric analyses and forecasts. RFSCAT would thus benefit NWP and climate.

Meteorological model grid distances are typically 50 km and well resolve the spatial error structures as one might expect. Since the spatial error structures are determined in size by the GOS density, one does generally not expect much benefit from a reduced grid distance. This is in particular true over the oceans where the surface forcing is relatively smooth. If smaller scales were allowed in the model, then there would be no (upper air) observations to initialise these. The model thus represents the mean atmospheric state over a 50 km distance typically and it would be best to obtain a measurement with such a footprint in order for it to be spatially representative of the model state. Smaller footprints would result in (observational) noise due to small-scale turbulence not resolved by the model.

Local modelling

The land-sea distribution is a source of small-scale atmospheric forcing, certainly when the coastal land is not flat. This forcing is often deterministic and it may then be worthwhile to observe the coastal circulation with increased sampling. This makes sense in particular, when the coastal land has a high-density meteorological network. Enhanced RFSCAT spatial and temporal coverage in the European coastal regions may be an option for fulfilling this requirement over water areas. From Table 3.1 we note that the high spatial resolution requirement is associated with a fast delivery requirement (about 1 hour).

3.1.2.2 Vertical Scale

In the vertical, NWP model levels are at roughly 500-1000 m and typical error correlation depths around 1500 m.. Direct upper-air impact of surface data is thus limited to a few km, and an increased number of surface observations should ideally be complemented by an increase in upper air measurements in order to obtain a consistent 3D analysis (see e.g., Stoffelen and Cats, 1991). We note that currently 4D variational data assimilation systems are under development, where it is potentially feasible to correct the model state over larger depths, thus increasing the impact of surface data. For example, Isaksen and Stoffelen (2000) report about the beneficial impact of ERS scatterometer winds in a 4D-Var system at ECMWF in case of tropical cyclones.

3.1.2.3 Temporal Domain

A requirement on temporal coverage may be defined by considering the typical time scale of evolution associated with structures of a spatial dimension equal to the structure functions. This time scale is typically one day, and a sensible requirement is to obtain global coverage every 12 hours. However, for the (much-desired) monitoring of fast developing weather systems a higher temporal requirement must be met. This is true in particular for local disturbances related to sea breeze or catabatic flow (e.g. mistral). Since the atmosphere is a moving target, the temporal and spatial coverage requirements are interrelated (see requirement on horizontal scales). For example, after the properties of an air mass are measured, it is required to measure the same air mass again after a time of 12 hours, but then it will be at a different location.

3.1.2.4 Accuracy

In the atmosphere wind variability is caused by 2D or 3D turbulent motion. Lilley and Peterson (1986) provide a range of climatological spectra for the horizontal motions. A typical wind-component variability energy-density spectrum is

$$E(k)dk = 0.25k^{-5/3}dk$$

where $k = 2\pi/\lambda$ is the wave number and λ is wave length in km. Most energy is present in the large-scale atmospheric motion and relatively little energy in the small-scale motion. It is thus most challenging to measure the small-scale atmospheric motion. The structure functions (e.g. Figure 3.2) determine the scales that we would like to analyse and add to the atmospheric state as represented in the model domain, i.e., the energy in these scales represents our signal. From the above spectrum we compute that the signal variance is about

$$\sigma^2 = 2 \int_{2\pi/400}^{2\pi/100} E(k)dk = 3.2 \text{ m}^2\text{s}^{-2}$$

Volume-mean quantities are needed. However, often a true volume-mean quantity can not be achieved and a spatial representativeness error remains. The variation of the horizontal wind in the vertical is not so important, but the horizontal variability dominates. Lorenc et al (1992) investigated this representativeness error in detail by considering climatological spectra for the horizontal motions. For an analysis on scales of 100 km and larger the wind vector spatial representativeness error of a local point measurement would thus typically be

$$\sigma_R^2 = 2 \int_{2\pi/100}^{\infty} E(k)dk = 2.1 \text{ m}^2\text{s}^{-2}$$

and of similar size to σ^2 . It may be clear that an area-mean measurement with small σ_R , such as potentially provided by RFSCAT, is of great benefit for the measurement of the signal of interest. A typical value for wind component accuracy, including spatial representativeness error, would thus be 1.5 m/s (see e.g. Stoffelen, 1996). The measurement of smaller scales is more challenging.

3.1.2.5 Bias

Bias has a context-sensitive interpretation and as such this term may cause confusion. Spatial or temporal error correlation is more specific if one specifies the spatial and temporal scales involved. Below we discuss several relevant spatial scales. Error correlation requirements on the smallest or shortest scales are usually most difficult to meet.

Spatially correlated error is potentially very damaging in data assimilation, in particular when the error structure is a priori not well known. Any systematic error in the analysis will have the multivariate and spatial structure prescribed by the structure functions, i.e., the error is meteorologically balanced and will influence the evolution of the model state in an effective way. Air mass dependent errors are the most damaging, since these potentially change the way air masses interact. Spatial correlation properties often depend on local uncertainties in the geophysical interpretation of the measurements, i.e., on the accuracy of the observation operator and cost function as mentioned at the end of the section on atmospheric analysis. For RFSCAT one could think of wind speed or sea state dependent errors in the interpretation. Fortunately, as for current scatterometers, such effects can be eliminated (Stoffelen, 1998).

Horizontal Error Correlation

Correlation of error between measurements does require investigation, and in some cases potential detrimental effects caused by spatially or temporally correlated error can be removed. Experience with other satellite sensors has shown that fixed systematic errors or systematic errors that depend only on specific instrument characteristics (look angle) or orbit phase can be taken out by comparison to a NWP model (E.g., Stoffelen, 1998). Obviously, in this case the NWP model is calibrated by using conventional observations. For calibration of an observing system against a NWP model it is an absolute requirement that the observing system and its systematic offsets are stable.

In summary, a useful and practical requirement for systematic offset effects may be that the error correlation between any two wind observations is less than 0.1.

3.1.2.6 Reliability

Many operational centres are using or developing variational analysis systems. The variational analysis system is quite flexible in dealing with observations with complex error characteristics as illustrated in Figure 3.3. However, for the measurements to be useful, these observation characteristics have to be a priori known in detail. As such, all signal characteristics have to be used to optimally specify the observation operator and cost function in order to help weight measurements according to the information content on the true atmospheric state.

3.1.2.7 Data Delivery

Meteorological data assimilation systems work in real time in order to provide suitable weather forecasts and a timely data delivery is essential for nowcasting and short range forecasting. In a meteorological data assimilation system those meteorological observations provided timely by the GOS are compared to the first guess. As such, the error characteristics of the first guess are

well monitored and the first guess is a well-defined reference atmospheric state. In turn, this reference atmospheric state is used to routinely monitor and control the observations. If observations are not timely available then this routine monitoring and control is not performed, and special measures have to be taken to collocate the observations with the NWP model and other observations in order to characterise the error properties of such observations. It may be clear that the routine monitoring and control of observations in the main real-time data stream is to be preferred above the off-line processing in most cases.

After that the signal and error characteristics of a new observing system have been determined, experimentation with the assimilation of the data may commence. If the data is delivered in real time then the operational forecast can be used as a control experiment. If it is demonstrated that the new observing system adds to the weather forecast skill of the control experiment, then real-time assimilation of the data will start in the weather or wave prediction application. A timely data delivery is then required since an analysis is started on pre-specified times and a data cut-off time is applied. For weather and wave prediction acceptable data delivery times for short- and medium-range forecasting vary generally between 30 minutes and more than 6 hours, depending on analysis time window and analysis delay. A data delivery requirement of 3 hours is usually specified for space-borne data as a (compromise) constraint. As may be clear from table 1, this makes the data less useful for nowcasting applications in coastal areas.

3.1.3 RFSCAT Application

RFSCAT measurements can provide information on part of the gravity-capillary wave spectrum at the ocean surface. From existing scatterometers it is known that gravity-capillary ocean waves are well correlated to wind speed and direction and that a non-linear relationship exists between these parameters. We show in this section that there is no principle problem in assimilating such data in wind analyses.

3.1.3.1 Geophysical Relationship

Scatterometry is a well established application of radar ocean sensing in atmospheric analysis (Stoffelen, 1998), and can in many respects be used as an example for the development of RFSCAT. Both for C- and Ku-band scatterometry theoretical models have been developed with the aim to aid in the interpretation of scatterometer measurements. The ocean surface, however, turned out to be of complex topography and the interaction of e.m. radiation with this surface too complicated to be described quantitatively with the required accuracy (Stoffelen, 1998; chapter I). If the amplitude spectrum of the different wave components is known, their phase relationship is of greater uncertainty. If anything, the amplitude of gravity-capillary waves is known to be most directly related to the shear stress that the wind exhibits on the water surface. Wind stress observations are very scarce and as such not very suitable to determine the relationship between a backscatter measurement and geophysical state. The relationship between wind stress and wind at reference height depends on the temperature and humidity stratification. However, this dependency is uncertain (about 30%) and accurate temperature and humidity information is usually not available. Since to first order atmospheric stability effects due to temperature and humidity can be incorporated as a wind speed dependency, it suffices to associate backscatter measurements with the wind at a reference height in the so-called surface layer, which extends at

least to about 30 m above the sea. Fortunately, high-accuracy scatterometer instruments were developed, that facilitated the development of empirical algorithms to establish a relationship between wind at 10 m height and radar backscatter. Accuracy thus appears a clear requirement for RFSCAT.

Mutual Measurement Consistency

For example, the ERS scatterometer measures backscatter at each location under three different geometric views. In fact, the relationship between the three backscatter measurements is such that a distribution of these triplets spans a cone-shaped surface in the three-dimensional measurement space (Stoffelen, 1998; Chapter II), as depicted in Figure 3.7. Since the instrument accuracy is 0.2 dB, this relationship may be investigated with the same accuracy. In theoretical modelling of the ocean response a correspondence of 1 dB is an achievement. Theoretical models may thus be improved by investigating space-borne scatterometer measurements. For RFSCAT it is more complex to visualise a large distribution in time and space of collocations of multiple measurements at a fixed set of geometric parameters. From a geophysical point of view the collocation distance should be small compared to the RFSCAT footprint and the collocation time window about 10 minutes. For larger collocation domains wind variability becomes relevant and thus the consistency smaller. It is to be seen how RFSCAT measurements mutual consistency can be used to infer signal or error characteristics. Since, the ERS scatterometer backscatter only depends on two geophysical parameters, the third piece of information from the ERS scatterometer provides information on the internal consistency (noise) and can be used to weigh or reject the retrieved winds in an analysis. Moreover, this overdeterminacy allows to monitor the instrument in time and the product of the geophysical retrieval procedure (Stoffelen, 1998; Chapter II).

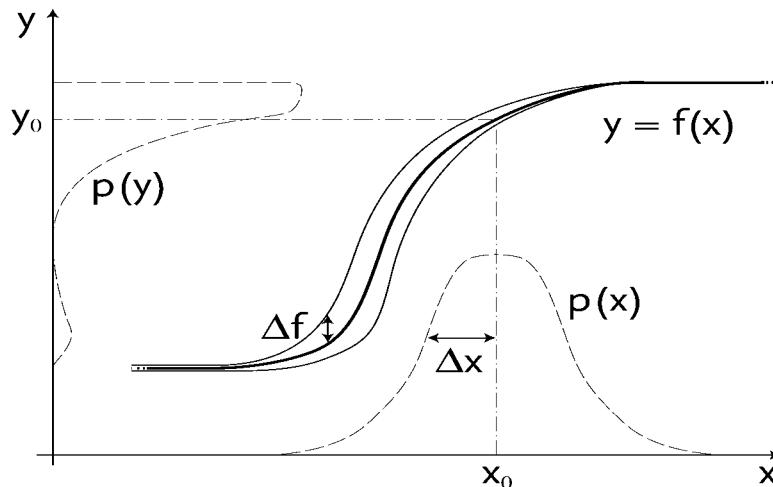


Figure 3.6: Non-linear transformation of a normal distribution $p(x)$ with mean x_0 and of width Δx to the skew and multi-peaked distribution $p(y)$ through an equation f with uncertainty Δf . The projection of the median x_0 of $p(x)$ to the median y_0 of $p(y)$ is shown by the dash-dotted line. For $p(y)$ the median, the mean, the most likely, and minimum variance values of y are all different (Stoffelen, 1998).

Empirical GMF Tuning

The scatterometer Geophysical Model Function (GMF) was determined by direct comparison of backscatter measurements to meteorological model wind data (assuming only wind dependency) (e.g., Stoffelen, 1998). In this case the errors and spatial representativeness of the comparison wind data and the scatterometer measurements have to be known, and care has to be taken of the input distribution of points to avoid biases in the GMF due to the non-linear transformation of noise distributions.

After checking the internal consistency and noise properties of the scatterometer measurements, attempts have been made to fit a GMF to sets of backscatter and wind data. An estimation of the GMF characteristics (non-linearities; harmonic dependencies), and an accurate specification of the noise properties of both the backscatter and wind data turned out to be necessary to find a GMF that obeys the same internal consistency (cone-shaped surface) as the backscatter measurements, for each set of geometrical views (Stoffelen, 1998; Chapter III). The methodology could be easily extended to RFSCAT for allowing precise relationships at slightly different frequencies or polarisation, since the same basic quantities and similar relationships are involved. Noise characterisation can be done in the overdetermined parts of the swath. Inversion and QC may be more complicated in a minor part of the swath where the problem is not overdetermined, due to lack of azimuth or polarisation coverage.

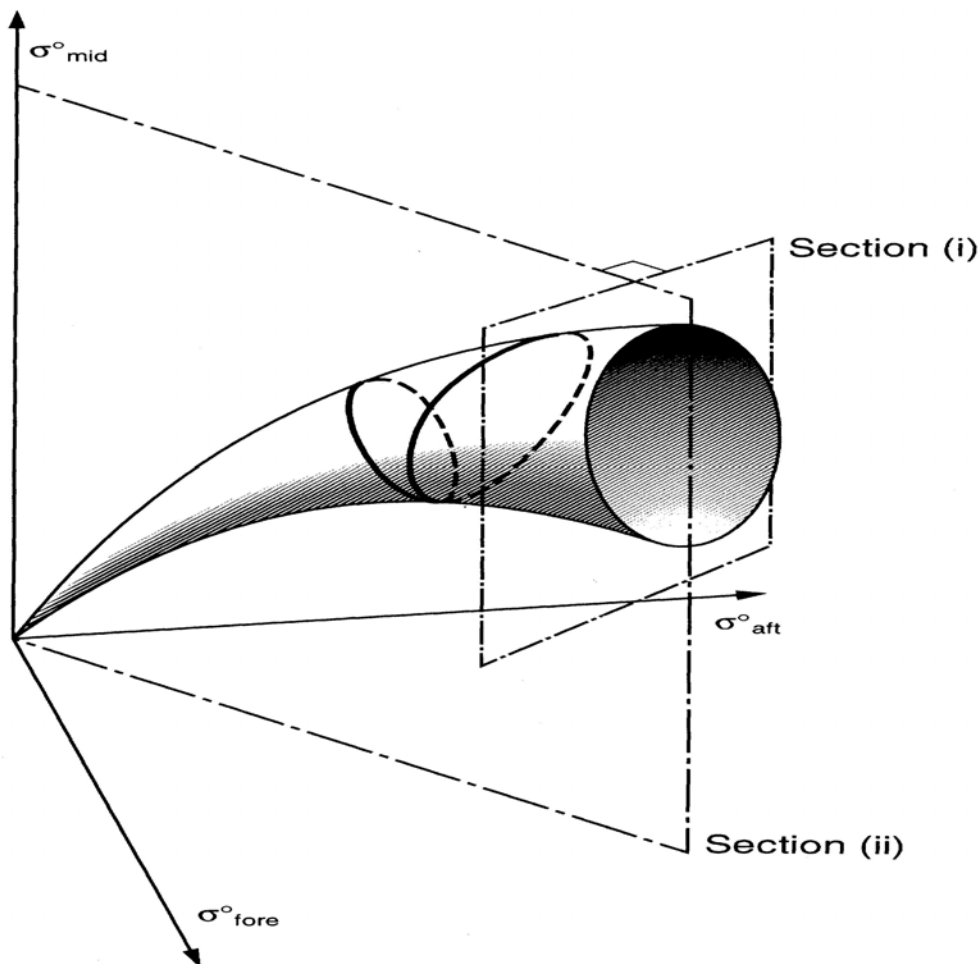


Figure 3.7: Depiction of the surface on which backscatter triplets lie for a given node. The surface actually consists of two sheaths that closely overlap. The Lissajous-type line represents the change of backscatter with wind direction for fixed speed (Stoffelen, 1998).

3.1.3.2 Wind Retrieval and Atmospheric Analysis

After that a GMF has been determined, one can in principle determine the information content of a RFSCAT measurement. RFSCAT depends on two geophysical variables in one grid point and the sensitivity to these variables needs to be specified in all particular cases where we would like to assimilate the data. If the observation operator $H(\mathbf{x})$ determines the functional dependency of the measurement y on the analysis state vector \mathbf{x} , then $y - H(\mathbf{x}_B)$ is the innovation with respect to the first guess state \mathbf{x}_B . The inverse of the derivative of H with respect to \mathbf{x} , $[H'(\mathbf{x})]^{-1}$, then determines the effect of the innovation on the atmospheric variables \mathbf{x} . We already know that a RFSCAT measurement depends on wind speed, wind direction, and probably some atmospheric stability or sea state parameters, but also that RFSCAT is ambiguous in wind direction and additional information is needed to constrain the problem.

Atmospheric and sea state models exist, so it is straightforward to compute a difference between a simulated RFSCAT measurement and a real measurement. This difference can be due to errors in predicted wind speed, wind direction, or other minor parameters, but also due to uncertainties in the area-mean RFSCAT measurement. The former uncertainties are mapped in a non-linear way to the RFSCAT measurement, probably giving rise to systematic off-sets or even ambiguity. Similarly, a RFSCAT measurement with expected normal errors, may result in an ambiguous or biased wind direction distribution, even if all other relevant geophysical parameters are known, as is illustrated in Figure 3.6. This in particular poses a problem to atmospheric data assimilation, i.e., the observation operator and cost function should not necessarily favour the most likely state, nor the minimum variance state, nor the modal state, but better an analysed state that is free of bias. This is not a trivial problem in case of a non-linear function $H(\mathbf{x})$.

The wind retrieval problem has been solved for scatterometry in a pragmatic way by making use of the internal consistency (overdeterminacy) of the data (Stoffelen, 1998); the most likely corresponding point on the cone-shaped surface is sought, given the measured triplet. Due to the low instrument noise of 0.2 dB, this point can be determined with great accuracy. Moreover, an ambiguous cost function is used in the atmospheric analysis. Studies are now ongoing to study the assimilation of NSCAT and SeaWinds scatterometer instrument data that have more ambiguity than the observations from ERS-1 or ERS-2, but of more variable likelihood. Progress with the assimilation of these types of data will further open the way to the use of non-linear and ambiguous observations (Figa and Stoffelen, 1999; Stoffelen, Voorrips, and de Vries, 2000).

3.1.3.3 Accuracy

The value of the measurements y in a geophysical analysis depend on their accuracy and on the sensitivity of the geophysical variables \mathbf{x} on y , as explained before. For a RFSCAT constellation it remains to be seen how much information can be obtained on wind direction in different parts of the swath. In scatterometry an accuracy of 0.2 dB provides good quality near-surface winds

after a careful tuning of the wind retrieval processing and the GMF. However, it should for RFSCAT remain possible to perform adequate QC, prior to data assimilation.. For RFSCAT a similar philosophy may be adopted for the tuning as described above. Since a similar relative modulation due to wind direction is expected, a similar accuracy may be required to retrieve the wind direction, i.e. 0.2 dB, for incidence angles larger than 20°. Wind direction dependency for smaller incidence angles is smaller and hardly useful. Scattering at angles larger than 60°, i.e. grazing incidence, may still result in useful geophysical information, however, theoretical models are extremely limited in usefulness for predicting the behaviour at such angles. Experimental and empirical evidence should be collected to obtain more knowledge in this area.

Sub-Footprint Variability

The wind and wave conditions on scales smaller than the footprint are not negligible as discussed in the wind requirements subsection on accuracy. This variability is convoluted with the radar ocean reflectivity response to obtain the RFSCAT signal. Since the scattering does not depend in a linear way on the geophysical parameters, (systematic) deviations may occur in the retrieval due to the sub-grid variability (as in Figure 3.6). Sub-footprint wind component variability is well described by a normal distribution (Stoffelen, 1998; Chapter 4), such that when an approximate GMF is available, then the effect of sub-footprint wind variability can be simulated. Anomalous wind variability will for instance somewhat reduce the harmonic response.

On the other hand, if the footprint is divided into smaller areas by range or frequency binning, then one may be able to estimate the sub-footprint variability from the resulting subsamples. In that case anomalous subfootprint variability may be identified and tested for quality control. In that way, observations that are difficult to interpret due to anomalous geophysical conditions may be down-weighted or even rejected. Moreover, at low footprint mean wind speed, it is the wind variability in the footprint that determines the mean backscatter, and if this variability is known more accurate wind retrieval at low wind speeds may be possible.

3.2 Expected Future Systems

During the last four decades the radar backscatter from the ocean surface has been studied by many investigators in order to develop techniques for measuring the near surface winds by means of remote sensing. Since the 1970s, the scatterometer activities in the United States focussed on K_u-band systems. An extensive flight program was conducted with the AAFE-RADSCAT (Jones et al. 1977; Jones and Schroeder, 1978; Schroeder et al. 1984) and a first spaceborne K_u-band scatterometer was flown aboard Skylab in 1973 (Moore and Fung, 1979). Finally, the first spaceborne wind scatterometer SASS was employed on the American SEASAT satellite in 1978. In the 1990s this line was continued by the NASA scatterometer NSCAT aboard the Japanese ADEOS satellite (1996-1997) and the present SeaWinds scatterometer on QuikSCAT. It will be further followed by the next employment of SeaWinds on ADEOS-II, which is scheduled for launch in 2001.

The second line of scatterometer development was initiated in Europe with ESA's decision for the C-band (5.3 GHz) Active Microwave Instrument (AMI) aboard the First European Remote

sensing Satellite (ERS-1) in 1981 (Haskell, 1983). At that time only a scant amount of radar backscatter measurements at C-band was available from the Naval Research Laboratory (NRL, Washington, D.C.) flights in the 1960s. The employed 4-frequency radar operated at 0.428 GHz (P-band), 1.228 GHz (L-band), 4.455 GHz (C-band), and 8.910 GHz (X-band) and HH- and VV-polarisation (Guinard et al. 1971). Though these data were excellent during that time, they did not provide a reliable basis for developing an algorithm to extract wind information from C-band backscatter data. As a consequence ESA initiated C-band scatterometer campaigns in order to establish a database for the development of the pre-launch wind scatterometer model for ERS-1 (Attema et al., 1986). Since the launches of ERS-1 in 1991 and ERS-2 in 1995 a vast amount of C-band NRCS data at VV-polarisation became available which was extensively used in order to improve the C-band VV-polarisation GMF.

Today the geophysical model functions (GMF) which relate the normalised radar cross section of the ocean surface to wind speed and direction exist only for K_u -band HH- and VV-polarisation and for C-band VV-polarisation. Very little data have been obtained and published for other frequencies or polarisation combinations, especially for cross-polarisation. As compared to K_u -band for C-band the situation is worse, there is even limited knowledge about the C-band ocean radar backscattering at HH-polarisation and no polarimetric data have been acquired so far. The wind retrieval for both systems suffers from ambiguities, which are caused by the symmetric GMF curves with respect to the azimuth angle. Theoretical work and microwave radiometer measurements indicate that the correlation between co- and the cross-polarised radar backscatter and/or emission are odd functions with respect to the azimuth angle (Nieghem et al., 1992, Yueh et al. 1994). This different azimuthal behaviour may be suited to improve the wind retrieval by solving wind direction ambiguities.

As a consequence future development of spaceborne wind scatterometers will have mainly the following goals:

- Improvement of the spatial resolution in order to better support coastal and land applications.
- Improvement of the temporal sampling by increasing the swath width and/or operating several satellites.
- Improvement of the ambiguity removal by employing multi-frequency, dual-polarisation or polarimetric systems.

While the first two points are more of technical nature and do not require new knowledge in scatterometry the third point will be of scientific interest during the next years. In 1996 ESA already initiated the POLRAD'96 campaign in order to collect polarimetric data over the sea, unfortunately no polarimetric scatterometer data could be collected (ESA, 1997). Recently Tsai et al (2000) published a feasibility study for an enhanced SeaWinds sensor with polarimetric capability. It was demonstrated that polarimetric measurements could improve the wind retrieval significantly. The used polarimetric GMF model is based on a theoretical model, which could not be validated due to lacking experimental polarimetric data.

Presently the airborne polarimetric C-band system (STORM) is being built at the Centre d'Etude des Environnements Terrestres et Planétaires (CETP), Velizy, France, as the successor of the RESSAC C-band system. First test flights are planned for spring 2001 (D. Hauser, pers. Communication). The range of incidence angles for the STORM system is limited to 0-35 degrees for the technical constraint that the antenna has to fit into an available radome for a Merlin IV aeroplane. Yet the rotating antenna will provide azimuthal information on the polarimetric radar backscattering properties. Though the limitation in incidence angle these data will allow for the first time to test the proposed polarimetric GMF for C-band. It might be possible to use first results within this study since Volkmar Wismann has been invited to participate in the data evaluation. This system will also be used in the validation of ASAR products within the ENVISAT AO-project *Participation to a field campaign with an airborne radar for the validation of wind and waves products of the ASAR*. The principle investigator (PI) is Daniele Hauser, from CETP/CNRS, France. The data of this experiment will not be available before end of 2001 and might not be considered in this study. If the first experiments with the STORM system support the polarimetric backscatter theories further tests at larger incidence angles could be made by mounting the antenna at the side of the aeroplane and conducting circle flights.

The ASAR aboard ENVISAT will provide data which will allow to study extensively the polarisation ratio (HH/VV) and the depolarisation ratio (VH/VV) of radar backscattering from the ocean. The system offers the so-called *Alternating Polarisation Mode* that provides two simultaneous images with the same imaging geometry in either HH and VV, HH and HV, or VV and VH polarisation. These scenes have a spatial resolution of 30 m and due to the ScanSAR technique 7 different swathes can be selected offering a range of incidence angles from 14 to 45 degrees while the respective swath widths vary from 108 km to 58 km. This will allow to simulate any scatterometer resolution. An advantage is that costly gathering of in-situ data is not necessary since the C-band VV mode together with existing GMF can be used to provide wind speed and direction information. However, limitations are the small maximum incidence angle of 45 degrees and the noise equivalent σ^0 of -22 dB that might not allow cross polarisation measurements at low wind speeds.

Interest in such kind of investigation has been announced in the research community and 3 respective proposals have been accepted by ESA within the first announcement of opportunity (AO) for ENVISAT:

Investigation of the Polarisation Ratio of Microwave Backscatter from the Ocean Using the ENVISAT ASAR in its Alternating Polarisation Mode, PI D.R. Thompson, Johns Hopkins University/APL, USA.

Use of ENVISAT Advanced Synthetic Aperture Radar Alternating Polarisation Mode Data for Ocean Wind Vector and Wave Field Estimation, PI P.W. Vachon, Canada Centre for Remote Sensing, Canada.

Automatic Classification of Oceanic and Atmospheric Features in ASAR Alternating Polarisation Mode Images of the Ocean, PI W. Alpers, University of Hamburg, Institute of Oceanography, Germany.

Presently, the launch of ENVISAT is scheduled for June 2001 thus it is not very likely that data or results from this mission can be used in this study. For future work, especially for validating the proposed C-band HH-polarisation model function or for developing a new one the ENVISAT data will be of great value.

Although it is not in the focus of this study, other applications of the RFSCAT data than wind retrieval over the oceans should be kept in mind. EUMETSAT initiated a study on possible operational products over land surfaces to be delineated from ASCAT data. Though most of the methods and techniques, which have been developed for retrieving geophysical information over land surfaces from ERS scatterometer data, can be applied to ASCAT data, the improved temporal coverage may lead also to the development of new detection algorithms for short-term processes. Figure 3.8 depicts NRCS time series from the SeaWinds and the ERS-2 scatterometers together with air temperature data for a location in Siberia¹.

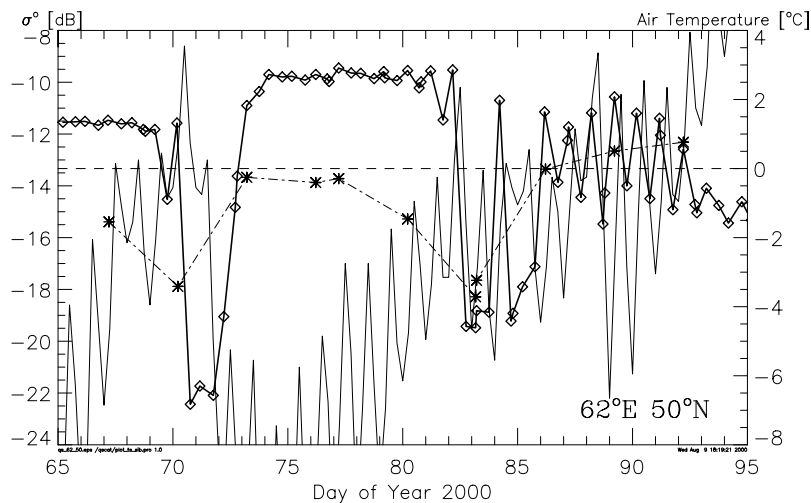


Figure 3.8: Time series of NRCS data from the SeaWinds K_u -band (diamonds) and the ERS-2 C-band (stars) scatterometers as well as of the air temperature (solid line) at $62^\circ\text{E}; 50^\circ\text{N}$ in Siberia.

Based on 3-day mean NRCS data from the ERS scatterometers a technique has been developed to detect and monitor the thawing of soils in Siberia (Wismann, 2000). Due to the higher repetition rate of QuikSCAT measurements the diurnal thaw-freeze cycle can be resolved by this data. The instantaneous reaction of the NRCS on the onset of melting can be seen on day 70 when the temperature exceeded significantly 0°C for the first time. On this day the NRCS decreases by 10 dB. During the following days the NRCS increased due to refreezing of the snow cover. Between day 87 and 92 temperatures above and below 0°C were encountered during day and night, respectively. The NRCS followed this thawing and freezing with a decrease and

¹ SeaWinds data at level 2A were provided by the Physical Oceanography Distributed Active Archive Center (PO.DAAC) at JPL, Pasadena, the ERS data by the French-PAF CERSAT at IFREMER, Brest, and the temperature data originate from the NCAR/NCEP reanalysis and were provided by the NOAA Climate Diagnostics Center.

increase. These diurnal fluctuations may be better suited to detect the thawing as the presently used 3-day mean change detection technique or at least may complement it in certain regions. The ERS-2 data in Figure 3.8 do not represent the 3-day mean values but all available data-takes during this period.

Since RFSCAT can be seen as a possible predecessor of ASCAT any improvement in spatial or temporal sampling by this instrument will have considerable impact on other fields of application.

4. Review of RFSCAT Concept

4.1 Review of the Proposed Instrument Concept

4.1.1 Instrument Concept

The measurement principle for RFSCAT is shown in Figure 4.1. The proposed RFSCAT is a spaceborne system on a polar orbiting platform at a height of 725 km. The antenna rotates at a rate of 0.35 rad/s, while the satellite travels with a velocity of 7.49 km/s, resulting in an epicycloidal footprint on the earth's surface with a total swath width of 1500 km. The incidence angle from a fanbeam varies from 28° to 51° . The radar operates at C-band, 5.3 GHz, and transmits and receives vertically polarized signals (VV). The radar operates in a pulsed mode, so that each point of the echo profile can be attributed to a unique pixel position within the antenna footprint along the radial direction (range-gated). The instrument parameters listed in Attachment I of SOW are listed in Table 4.1 here which are reviewed in the following subsections.

Table 4.1: Scatterometer concept for high resolution mode

Parameter	Option 1	Option 2
Orbit / repeat cycle	725 km / 2 day	1075 km/2 days
Antenna scan rate	0.35 rad/s (3.3 rpm)	0.25 rad/s (2.4 rpm)
Total swath	1500 km	1600 km
Min. wind speed	≤ 4 m/s cross-wind	≤ 4 m/s cross-wind
Incidence angle	$28^{\circ} - 51^{\circ}$	$21^{\circ} - 42.5^{\circ}$
Footprint length	408.6 km	450.5 km
Frequency	5.3 GHz	5.3 GHz
Polarization	VV	VV
Pulse bandwidth	1.06 MHz	1.39 MHz
Pulse compr. Ratio	200	200
Pulse rep. Frequency	239 Hz	179
Nrange	50 (HR)	50 (HR)
Nazimuth	13.7 (HR)	13.4 (HR)
Spatial resolution	15 km \times 15 km (HR) 50 km \times 50 km (wind)	15km \times 15 km (HR) 50 km \times 50 km (wind)
Radiometric resolution	≤ 0.3 dB (HR) ≤ 0.09 dB (wind)	≤ 0.3 dB ≤ 0.11 dB (wind)
Average RF power	145 W	83 W
Antenna size	3.6 m \times 0.4 m	4.6 m \times 0.4 m

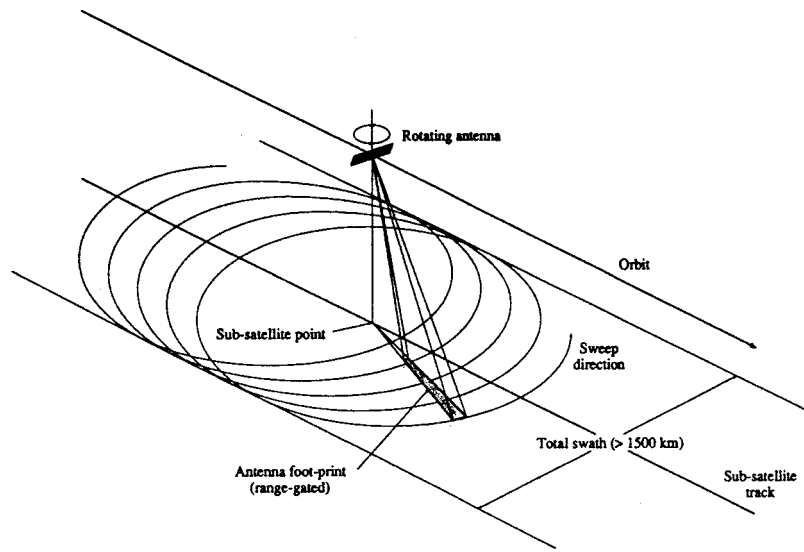


Figure 4.1: Rotating fanbeam scatterometer concept

4.1.1.1 Measurement Geometry

Scan Geometry

The RFSCAT scan geometry depends on:

- the spacecraft (orbit) altitude;
- the antenna footprint size and position (with respect to the sub-satellite point);
- the antenna rotation speed.

The width of the total swath is determined by the farthest point of the antenna footprint. Generally, a largest possible swath is desirable for minimising the time necessary for a global coverage of the Earth. This can be achieved by two means: (1) increase the orbit altitude for a given incidence angle or; (2) increase the incidence angle (range) for a given orbit altitude. Unfortunately, an increase in orbit altitude results in decrease in the radar link-budget which must be compensated by higher transmit power or higher antenna gain. The increase in the incidence angle, on the other hand, is not desirable beyond a certain limit for which the wind extraction algorithms become unreliable due to the rapidly decreasing normalised radar cross-section of the ocean surface. In conclusion, the achievable swath width is constrained by the on-board power resource and the maximum allowable antenna size.

The swath defined by the RFSCAT is illustrated in Figure 4.2a while Figure 4.2b defines the geometry. The incidence angle is θ_i , the satellite height is h and the earth radius is R . The incidence angle for the RFSCAT varies from 28° to 51° . The antenna pointing angle α and the slant range r can be calculated using the Law of Sines:

$$\frac{\sin \alpha}{R} = \frac{\sin \theta_i}{R + h}$$

Also, $\eta = \theta_i - \alpha$, $S = R \cdot \eta$, and $l = R \cdot \sin \eta$. The height different Δh between the nadir point and the point at which the radar beam intersects the surface is given by $\Delta h = R - R \cdot \cos \eta$.

These equations permit the calculation of all geometrical quantities in the Figure 4.2. The Table 4.2 gives values for required range of incidence angle.

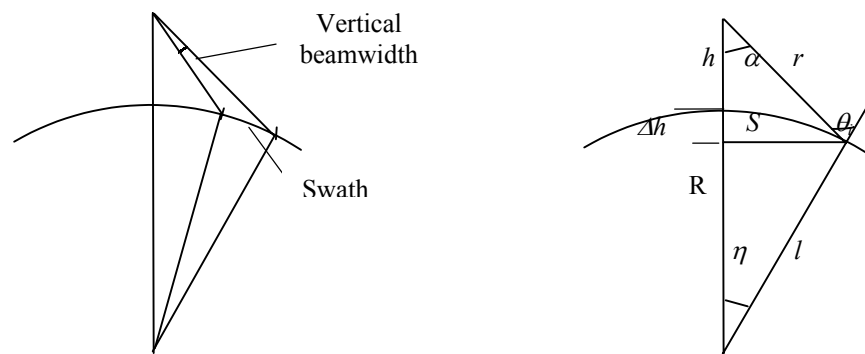


Figure 4.2: Satellite geometry. a) Swath illustration, b) definition of quantities.

The antenna azimuth rotates at an angular rate of 0.35 rad/s. The sweep speed of the beam on the ground (neglecting satellite motion and earth rotation) is $0.35 \cdot l$. This is also shown in the Table 4.2.

Table 4.2: Satellite Geometry

θ_i ($^\circ$)	α ($^\circ$)	η ($^\circ$)	S (km)	r (km)	l (km)	Sweep Speed (km/s)
28	24.924	3.076	341.3	809.6	341.2	119.4
40	35.239	4.7613	528.2	914.5	527.7	184.7
51	44.234	6.766	750.7	1073.7	749.0	262.1

The satellite ground speed is 6.7 km/s, which is almost negligible compared to the sweep speed, except that it produces a slight asymmetry in total sweep speeds on opposite side of the satellite path. The rotation speed of a point on the earth's equator is approximately 0.46 km/s. These have little effect on the performance analysis but, of course, cannot be neglected in the system simulation.

The antenna rotates in azimuth at a rate of 0.35 rad/s while the satellite moves forward at a speed of 6.7 km/s. Thus, in one revolution (17.95 second), it moves forward by a distance of $6.7 \times$

$17.95 = 120.3$ km. The width of a swath corresponding to the arc length S between incidence angles of 28° to 51° is $749.0 - 341.2 = 407.8$ km. Therefore, the overlap between adjacent sweeps is $407.8 - 120.3 = 287.5$ km or 70.5%.

Number of Acquisitions

The inversion of the data to extract wind information requires at least 4 acquisitions at different azimuth view-angles during an over-flight. It is furthermore desirable that the observation angles are spaced not too close to each others in order to limit the number of ambiguous solutions. Provision of a higher number of acquisitions (> 4) per over-flight could reduce the ambiguity problem and also opens possibilities for other applications such as sea-ice, snow and land observations [Cavanié 98; Wismann 98]. Thus, a larger number of acquisitions has been aimed for by taking advantage of the new scanning geometry.

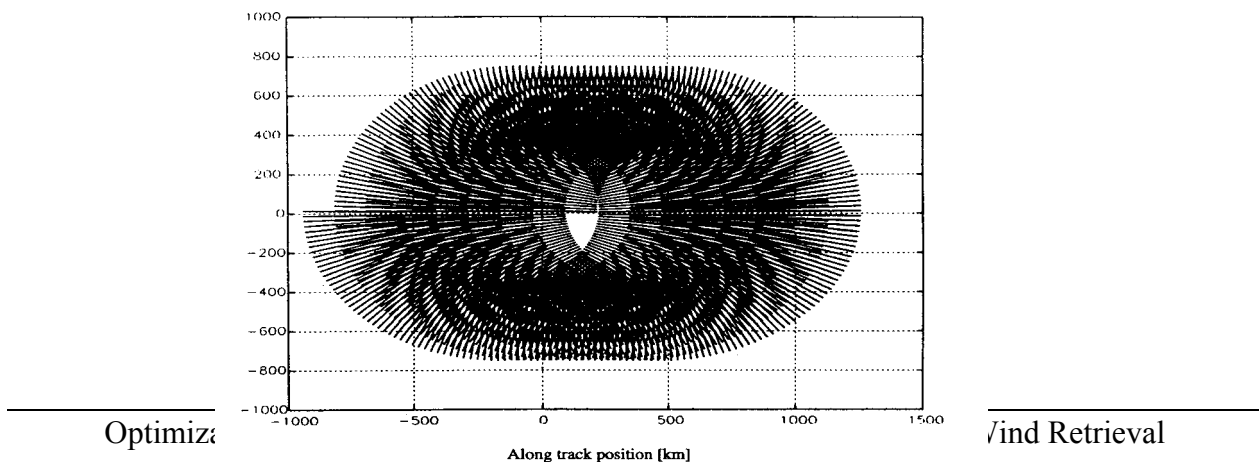
In order to achieve a good coverage within the total swath and a large number of acquisitions, the rotation speed of the antenna must be sufficiently high such as to produce large overlaps of the antenna footprint between successive scans. If ω_a (rad/s) is the rotation rate of the antenna, the satellite displacement Δx (km) between two successive scans (one complete rotation) is given

$$\Delta x = v_g \frac{2\pi}{\omega_a}$$

by:

where v_g is the spacecraft ground-speed (≈ 6.7 km/s). This distance must be a fraction of the radial size of the antenna footprint. If e.g. Δx is one third of the latter, a point on the sub-satellite track is viewed 3 times in the forward direction and 3 more times in the backward direction during an over-flight. Figure 4.3 shows an example of such a case (70 % overlap between the successive scans) with a total swath width of 1500 km. The positions of the antenna footprints during 6 complete scanning cycles are marked by bars in order to illustrate their overlap during an over-flight. This figure demonstrates the complex overlap which occurs during successive scans.

Figure 4.3 FRSCAT scan coverage



Optimiz

Wind Retrieval

The pixel acquisition geometry has been investigated [lin 00]. Figure 4.4 shows the number of acquisitions as a function of across track position for one over-flight. Figure 4.5 shows the average number of acquisitions as a function of across track position. The graphs indicate that in the inner swath, the number of acquisitions is fairly low, while for the outer swath, the number of acquisitions are also very low.

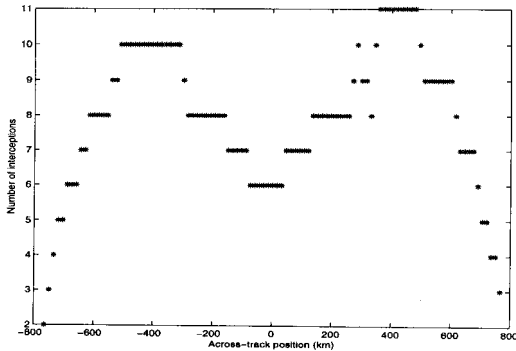


Figure 4.4 Number of interceptions as a function of the across-track position

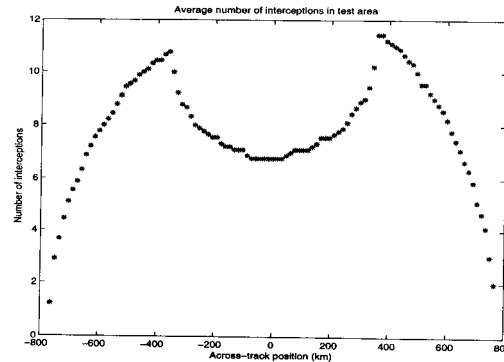


Figure 4.5 Average of number of interception as a function of the across-track position

Incidence and azimuth view-angles

The analysis of the incidence and azimuth view-angles as a function of the across-track position was performed by simulating an over-flight [lin, 00]. The following set of system parameters was assumed:

Orbit height:	725 km ($v_g = 6.7$ km/s)
Total swath:	1500 km
Footprint length:	408.6 km (in radial direction)
Incidence angle:	$28^{\circ} - 51^{\circ}$
Antenna scan rate:	0.35 rad/s (3.3 rpm)

Note that the dwell-time of the antenna beam over a given measurement pixel differs between the left and right sides of the swath. This is because the satellite ground velocity and the projected scan velocity add up on the right-hand side, whereas they are subtracted on the left-hand side. The ground-sweep velocity due to the antenna rotation alone (without satellite motion) is 120 km/s and 263 km/s for the inner and outer limits of the antenna footprint, respectively. When superposed onto the satellite motion, the sweep asymmetry on the left and right-hand sides due to the satellite motion (6.7 km/s) is less than 12 %, therefore negligible.

The simulation was carried out over a ground-track distance of 10000 km during which 83 rotations were completed by the antenna. Due to the negligible asymmetry on the left and right-hand sides of the swath, the analysis was restricted to the left-hand side only. The measurement swath was divided into resolution cells of $15 \text{ km} \times 15 \text{ km}$, and the incidence and azimuth view-angles were recorded at each passage of the antenna footprint over those cells. As the number of

acquisitions varies not only as a function of the across-track position but also slightly with the position along track, the result was summed over narrow strips of 10000 km in order to observe an averaged statistical behaviour of those angle distributions. The result for the incidence angles is presented for a strip width of 100 km whereas the azimuth view-angles are presented for a 50 km strip width.

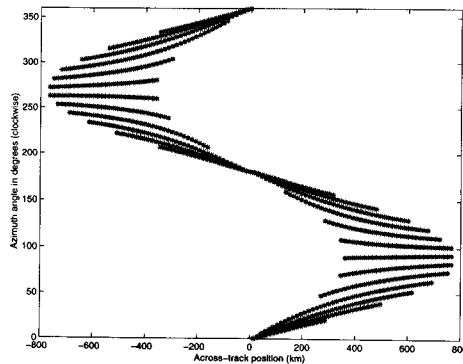


Figure 4.6 Azimuth view-angle as a function of the across-track position

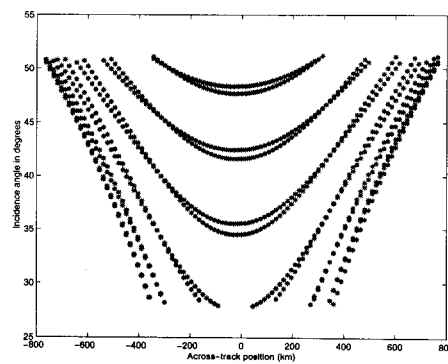


Figure 4.7 Incidence angle as a function of the across-track position

Figures 4.6 and 4.7 illustrate the distribution of azimuth and incidence angles for the acquisition respectively as a function of across track position. The system allows multiple azimuth views (up to 11 acquisitions per overpass). The graphs indicate that in the inner swath, the range of azimuth angles is also very low while the range of incidence angles is good. For the outer swath, the number of azimuth angle range and incidence angle range are also very low. From the study, the conclusion can be made:

- the distribution of the azimuth view-angles around the sub-satellite track as well as around the swath edges is less than optimum for inversion algorithms to obtain wind speed and direction, hence an ambiguity removal scheme is needed for those areas;
- at intermediate swath positions (300 – 650 km from the sub-satellite track), an optimum measurement condition is achieved with well-distributed azimuth view-angles and a large number of acquisitions per pixel.

4.1.1.2 Instrument parameters

Frequency

Initially, both C and Ku-bands were considered in the trade-off. Despite the prospect of smaller antenna to be required at Ku-band, the C-band concept presented a more favourable radar link-budget. Furthermore, the effects of the moisture in the atmosphere as well as that of sea-surface roughness changes due to precipitation are much weaker at C-band. And lastly, the radar signature at C-band has a higher saturation level than at Ku-band for extreme winds. Those considerations led us to favour a C-band system. A total swath width of larger or equal to 1500 km was specified for ensuring global coverage in two days. Two orbit options were then

identified at 725 km (Option 1) and 1075 km (Option 2) heights which also met the other requirements.

Bandwidth and pulse compression

A system bandwidth of 1.06 MHz or 1.39 MHz was necessary for Option 1 and Option 2, respectively, in order to provide a minimum of 50 range-looks within 15 km. For avoiding very high peak RF-power, a pulse compression technique (linear chirp) was introduced with a compression ratio of 200.

Number of samples and Radiometric Resolution

Two spatial resolution requirements were put: a High-Resolution (HR) mode and a Wind mode. For HR mode, a multi-look spatial resolution starting from 12 x 12 km to 18 x 18 km was considered whereas the Wind mode requirement was 50 x 50 km. The required spatial resolution is achieved with a shorter antenna (3.6 m) in Option 1 (725 km orbit height). As the antenna length is a critical design driver for such a mechanically rotated system, this lower orbit option has been selected for the further design activity. The radiometric resolution Γ (dB) which expresses the standard deviation of the signal is given by:

$$\Gamma = 10 \times \log \left\{ 1 + \sqrt{\frac{1}{N_{sig}} \left(1 + \frac{1}{SNR} \right)^2 + \frac{1}{N_{noise} SNR^2}} \right\}$$

where

N_{sig} : Number of signal samples (looks) within the multi-look resolution cell

N_{noise} : Number of noise samples within the multi-look resolution cell

SNR : Single-look signal-to-noise ratio

The total number of looks N_{sig} within a resolution cell is given by:

$$N_{sig} = N_{range} \times N_{azimuth}$$

where N_{range} is the number of independent looks in the radial (range) direction and $N_{azimuth}$ is the number of independent looks in the azimuth direction (number of summed echos).

The single-look signal to noise ratio for maximum range and 2 m/s and 4 m/s wind speed at cross wind look direction has been calculated as 4.5 and 11.5 dB respectively, without considering system losses and other non-ideal effects. The SNR and the number of looks determine the radiometric resolution of the system. The number of noise looks N_{noise} refers to the number of samples of received signals when only the receiver is operating. This mode measures noise power only. The scatterometer description in Attachment I of the SOW states that the number of looks N_{sig} in a resolution cell is 685 for the high resolution mode. However, the number of noise samples N_{noise} is not defined. It is not known how these samples are measured. It is likely that some of the time devoted to signal looks will have to be used for noise samples. This will reduce the number of signal looks N_{sig} .

For the high resolution mode, there are 13.7 azimuth steps per resolution cell and 50 range steps to give a total $N_{sig} = 685$. If one azimuth step per resolution cell is devoted to noise measurement, this leaves $N_{sig} = 635$. One azimuth step takes $1/239 = 4.184$ ms.

The system time resolution is $0.94 \mu\text{s}$. Therefore, one azimuth step time could give more than 4000 noise samples. It should be noted that noise measurements cannot be resolved to the resolution cell, only to the footprint area. Radiated noise from the surface would be averaged over this area.

It is assumed that $N_{sig} = 635$ and $N_{noise} = 4000$. For a SNR of 4.5 dB (i.e. 2.82), $\Gamma = 0.23$ dB. For a SNR ratio of 11.5 dB (i.e. 14.12), $\Gamma = 0.18$ dB. If some losses are assumed for non-ideal performance and the SNR values are taken to be 3 dB and 10 dB, the Γ values are 0.25 dB and 0.19 dB respectively.

The radiometric resolution Γ is a measure of the accuracy of the σ^0 estimate and is a function of the SNR, the number of signal looks N_{sig} and the number of noise looks N_{noise} . These variables are, in turn, dependent on the scatterometer parameters, scatterometer resolution, the size of the resolution cell, the measurement geometry (slant range and incidence angle) and the σ^0 value (dependent on wind speed and direction).

For a given transmit power, there is a trade-off between the SNR and the number of the looks for integration to improve the radiometric resolution. High SNR can be achieved by reducing antenna beam size and faster rotation rate. On the other hand, the number of looks can be improved by increasing the antenna beam width with slower rotation rate (or increase dwell time). For example, if the SNR goes from 1 to 10, the radiometric resolution improved by 3 dB. For higher SNR beyond 10, the maximum improvement of the radiometric resolution is about 10%. Thus, it is not necessary advantageous for a scatterometer to have a very high SNR. The effort should be better spent on having larger values of number of looks with a moderate SNR.

The number of looks depends on the resolution parameters. However, these parameters also affect the SNR. The radiometric resolution is therefore a complex function of the radar parameters and the measurement values. Furthermore, if the system has several channels (i.g. system enhancements) and the channels are processed sequentially, there is a trade-off between Γ , the number of channels and the spatial resolution. The study will determine the optimum trade-off between the system parameters for best system performance.

The ultimate system performance measure is the wind retrieval accuracy. This depends not only on the radiometric resolution but also on the shape of the GMF and the measurement geometry. The study will characterize wind retrieval accuracy as a function of system parameters by means of simulation and determine an optimum set of system parameters.

4.1.2 Instrument Design

4.1.2.1 Baseline Design

The hardware block diagram of the baseline system is given in Figure 5 of Attachment I of the Statement of Work (SOW), and is illustrated here in Figure 4.8. A vertically polarized signal is transmitted and a vertically polarized signal is received. The system operates in C-band.

The system consists mainly of an antenna, Data Conditioning Equipment (DCE), Radio Frequency Electronics (RFE), and Front - End Electronics (FEE). The DCE provides transmit signal generation and receive data processing. The RFE up-converts and down-converts signals. It sends Tx signals to the High Power Amplifier (HPA) and receives Rx signals from the Low Noise Amplifier (LNA). Isolation between transmit and receive paths is provided by a circulator.

The system also contains the Power Control Unit (PCU), the Interface Control Electronics (ICE), the Antenna Control Electronics (ACE) and a Calibration Unit.

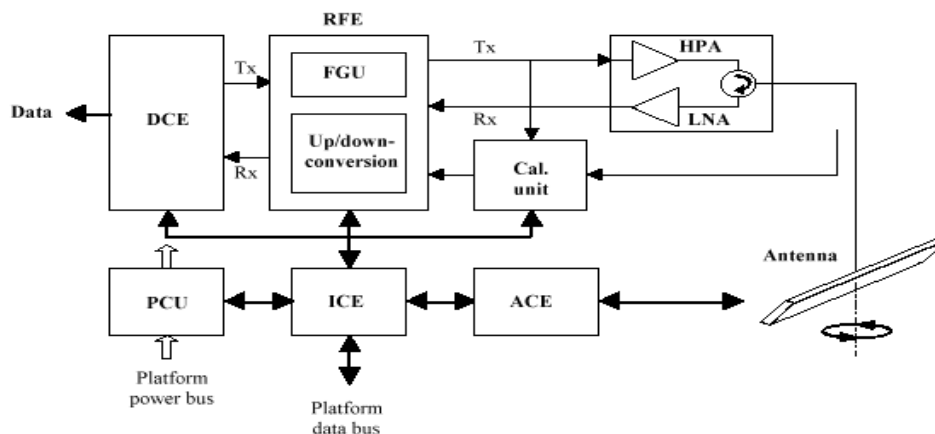


Figure 4.8: Instrument general block diagram

4.1.2.2 Doppler Compensation

A preliminary analysis has shown in Figure 4.9 that in the worst case, the Doppler shift of the received signal as a function of slant range could vary from 100 kHz to 160 kHz (see Figure 4.5, [MPBT 00]). If this Doppler shift is not compensated, the compressed pulse from a given location will be shifted in time and its amplitude will be reduced. The time shift must correspond to a distance of much less than a resolution cell size (15 km). The amplitude reduction must be kept well below the radiometric resolution (< 0.3 dB). The Doppler compensation accuracy needed for this purpose will be investigated using the simulation program and also by analytical methods.

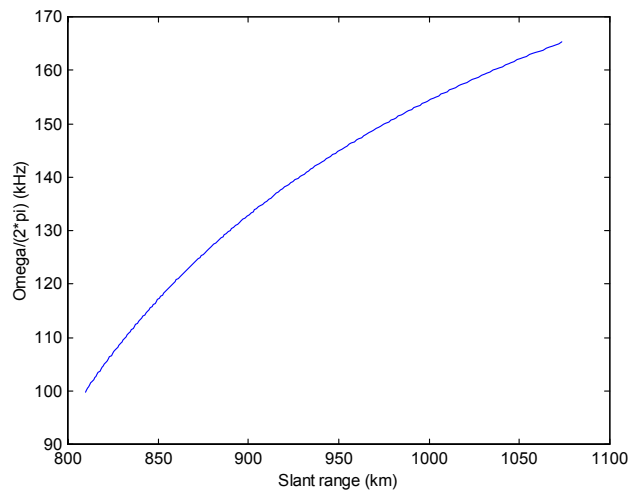


Figure 4.9: Doppler shift vs slant range.

4.1.3 Preliminary Analysis of RFSCAT Performance Issues

The RFSCAT is a relatively simple system with good coverage, and ranges of azimuth and incidence angles. The number of acquisitions is quite high in large areas of the swath. However, in parts of the swath, i.e. within 300 km of the sub-satellite track and more than 650 km away from the track, the number of acquisitions and ranges of azimuth and incidence angles will be low (see Figures 4.4 to 4.7).

The trade off for the good coverage is that the antenna gain is lower than for pencil beam systems and the resulting signal to noise ratio at maximum range is low for low wind speeds (4.5 dB for 2 m/s, [MPBT 00]). This value is acceptable after multi look averaging over a 15 km resolution cell. However, the signal to noise ratio should not be degraded much further and all equipment inaccuracies must be minimized.

The preliminary analysis [MPBT 00] has given the minimum single look signal to noise ratio at maximum range of 4.5 dB and a corresponding radiometric resolution of 0.23 dB. This is satisfactory, but these values will be verified using the simulation program.

One critical area is the Doppler compensation. The worst case Doppler shift ranges from 100 to 160 kHz over the slant range variation. If the shift is not compensated, the return signal values will be shifted in time and reduced in amplitude after pulse compression. If the Doppler shift is f_d , the pulse width is τ (200 μ s) and Δ is the chirp range ($\Delta \approx 1$ MHz), the time shift is

$$T_0 = \tau \times f_d / \Delta$$

And the amplitude reduction is $1 - (f_d / \Delta)$ [Hovanessian 84].

For a 100 kHz error, the time shift is 20 μ s, which corresponds to a range error of 3 km. The amplitude reduction is 0.9 (i.e. -0.9 dB). It is clear that the Doppler shift must be compensated.

The Doppler shift, not including earth rotation shift, is given by [MPBT 00]:

$$\omega_d = \frac{4\pi v}{\lambda} \sqrt{1 - \frac{h^2}{r^2}} \cos \varphi; \quad v = \frac{dx}{dt}$$

where v is the satellite speed, λ is the wavelength, $h + \Delta h$ is the effective satellite altitude, r is the slant range, and φ is the azimuth angle relative to sub-satellite track.

The graph of Doppler shift versus slant range is given in Figure 4.9 for $\varphi = 0$.

For other values of φ , the Doppler varies as $\cos \varphi$. At $\varphi = \pm \pi/2$, the Doppler shift is zero, not including earth rotation effects. At $\varphi = \pm \pi/4$ and $\pm 3\pi/4$, the range of Doppler shifts is about 70 to 110 kHz.

The earth's rotation also contributes a Doppler shift. At the equator, the rotation speed is about 0.46 km/s. At higher latitudes, the rotation speed varies as the cosine of the latitude.

The Doppler shift due to the earth rotation is largest at the equator. Since satellite is on a sun-synchronous orbit, the earth motion is almost perpendicular to the satellite track at the equator. At this point, the maximum Doppler shift is approximately 7.5 kHz. This value is calculated from the formula for ω_d above with v being the rotation speed of the earth in this case and $\cos \varphi \approx 1$. This shift occurs when φ is around $\pm \pi/2$. The effects of this shift are much smaller than due to satellite velocity and are almost negligible.

Other critical areas are the performance at the swath edges and inner areas and the resolution of ambiguities. The system enhancements are intended to address the ambiguity performance but will involve a loss of signal to noise ratio for the main VV channel. This issue must be carefully studied to ensure the best system performance.

If a polarimetric system is considered, the low signal to noise ratio (15 dB) below the main channel becomes a critical issue.

4.1.4 Preliminary Analysis of System Risk

4.1.4.1 Baseline system

The RFSCAT baseline system risk must be considered in two areas: implementation and performance. The technology to be used is mature and not too complex. It is expected that implementation within the size and weight constraints of the satellite.

The signal processing involved for the received signals is also clearly established and is feasible. The most critical aspect is the Doppler compensation and the pulse compression. The Doppler compensation is especially important. The accuracy with which this is performed will affect system performance. There is a trade-off between the processing power required for an accurate approximation and the performance loss of a simple approximation. Optimizing the trade-off will require the use of the simulation program.

4.1.4.2 Enhancements

The proposed enhancements and recommendations are given in Section 4.1.5. The recommended system enhancement is the addition of a horizontal polarization (HH) capability, and possible consideration of a polarimetric (HV) capability. These systems are judged to be feasible. However, they could cause significant performance losses (e.g. not meeting the 0.3 dB radiometric resolution requirement) of the basic VV channel. The losses could be compensated by increasing the HPA output, but this would affect the satellite power budget. A careful trade-off must be made to optimize such systems.

The polarimetric system also has the risk that the signal to noise ratio of the HV channel may be too low but the recommended enhancement is the HH capability in any case.

4.1.5 System Equipment Enhancements

4.1.5.1 General

The baseline system for this study is a C-band VV polarization system. Several potential system enhancements have been identified and are listed below:

- a) Addition of horizontal polarization (HH)
- b) Addition of polarimetric capability
- c) Addition of another frequency
- d) Addition of a second symmetric beam

The motivation for adding these features is mainly to remove ambiguous solutions for the wind velocities. In particular, the upwind / downwind ambiguity must be resolved as much as possible.

The system design modification involves RF design, antennas, system calibrations and data acquisition and processing. These issues are also discussed in this section.

4.1.5.2 Equipment Design and Performance

4.1.5.2.1 RF Design Issues

An enhanced system with more than one channel can operate either simultaneously or sequentially. The two channels system is assumed for the following discussions.

The characteristics of the simultaneous system are that the transmitter will require double power per pulse for same performance as baseline system, the receiver equipment will be increased and data processing circuitry will be either increased or speeded-up, and a good isolation will be required between channels (e.g. V / H).

The characteristics of the sequential system are that the transmitter power will be the same as baseline but no. of looks will be reduced, therefore, there is a trade-off between the radiometer

resolution and the spatial resolution. The receiver equipment and data processing will be similar to the baseline system, and the isolation between channels is not a problem.

The system RF performance is measured by the transmit power loss and the receiver RF noise figure. Number of RF components determines extra losses and receiver noise figure increase. Extra RF components, such as circulators, isolators, switches, OMT's, etc. in the RF path will increase RF transmit losses and receiver noise figure increase of the system.

The system power consumption is also an important issue. The power consumption increases with number of channels. However, the number of transmit channels is the main factor for power consumption

4.1.5.2.2 Antennas

The antenna configuration is also an important area for the system design, which involves

- Number of antennas;
- Antenna type;
- Design & construction technologies; and
- Size and weight.

These features are summarized in the Tables 4.3 and 4.4 below.

Table 4.3 Antenna Configuration

Antenna Configuration	Potential Concepts
Dual Frequencies	<ul style="list-style-type: none"> - Reflector (long length, narrow width) - Two feeds with different frequencies (transmit simultaneous) - Existing pencil beam scatterometers use this type - Planar array (passive) - Slotted array – two separate arrays - Microstrip - Active phased array (RadarSat II) - Preferred: Reflector with dual frequency feeds
Polarization / Polarimetric	<ul style="list-style-type: none"> - Reflector - Cassegrain feed - Dual polarised feed - Planar array (passive) - Slotted array (existing fanbeam scatterometers use this type) - Microstrip – Simultaneous transmit H & V - Preferred: Microstrip Planar array
Dual Beam	<ul style="list-style-type: none"> - Two antennas – simultaneous transmit - Two reflectors or planar arrays

Table 4.4 Antenna Size and Weight

The example of the antenna size and weight of the existing scatterometer antenna, ERS-1, is given in the Table 4.4.

	Size	Total Weight	
		Aluminum	CFRP
Fore/Aft	4 x 6 slotted waveguides for each antenna 0.25 m x 3.6 m	4 x 25.6 kg	4 x 7.7 kg
Mid	4 x 8 slotted waveguides 0.36 m x 2.3 m	2 x 15.6 kg	2 x 7.1 kg
Panels total		133.6 kg	45.0 kg

For RFSCAT, there is only one antenna in the baseline system and the antenna weight would be approximately 25.6 kg for an aluminum antenna and 7.7 kg for the CFRP antenna.

4.1.5.2.3 System Calibration

The system calibration is another important aspect of the system design. Two types of the calibrations are needed for a scatterometer, absolute calibration and relative calibration in which gains of all channels must be balanced.

There are two types of the calibration methods which are the external calibration and the internal calibration. The external calibration provides absolute calibration, it can be achieved using a transponder or an earth target. The external calibration can be performed periodically. On the other hand, the internal calibration provides relative calibration. A coupler can be used to sample the transmit signals and then send them to the receiver channels. The internal calibration can balance channels but does not include the calibration of the antenna. It can be performed continuously.

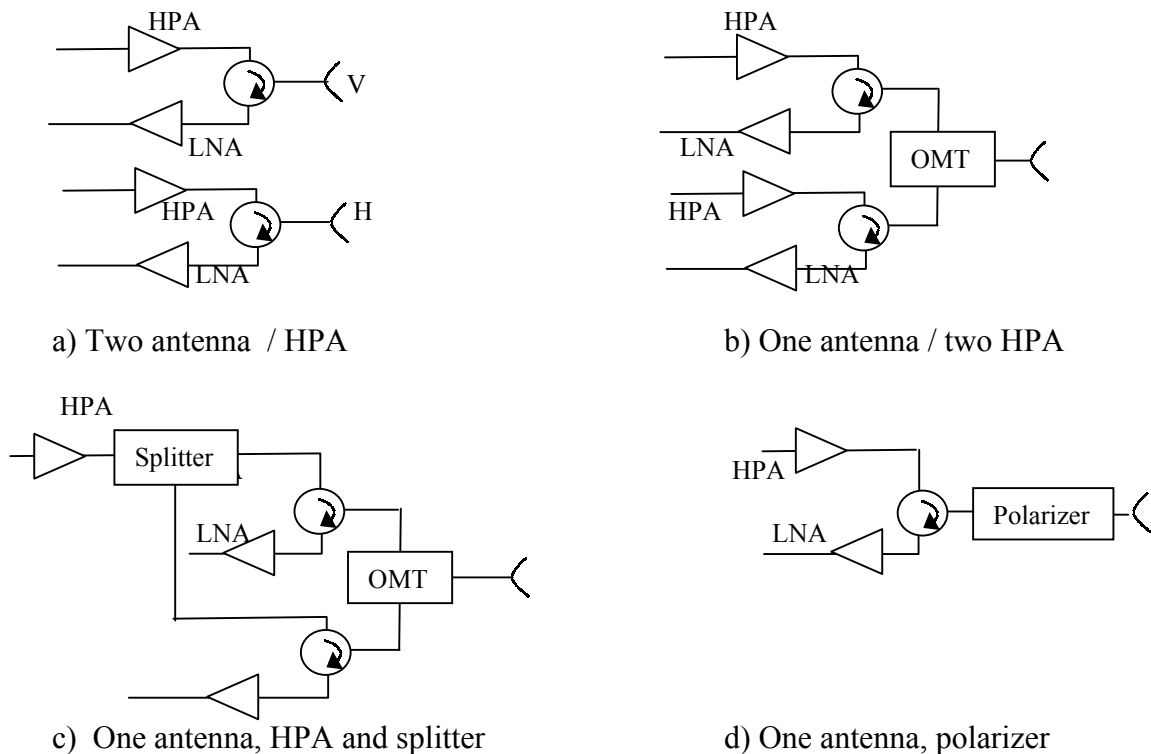
4.1.5.2.4 Data Acquisition and Processing

The data acquisition and processing complexity depends directly on the number of channels. However, the complexity can be traded-off for the processor speed. The baseline system sampling rate is of the order of 5 MHz per channel for digital signal processing.

4.1.5.3 Potential Enhancements

4.1.5.3.1 HH Polarization Channel

There are several potential techniques to implement a second HH polarization channel. The FEE / Antenna portions of these different approaches are illustrated in Figure 4.10.



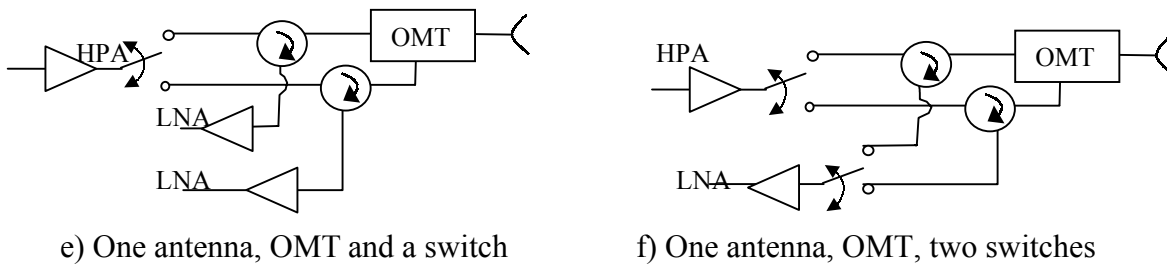


Figure 4.10 HH Channel – potential approach.

The approach of Figure 4.10a) uses two antennas and two identical parallel RF paths. Figure 4.10b) uses two identical RF paths but only one antenna. An orthomode transducer (OMT) provides the separation of H and V polarizations. 4.10c) uses one HPA and a power splitter to feed both RF channels. Figure 4.10d) uses only one RF path together with a polarizer to switch between V and H polarizations. 4.10e) uses one antenna, and HPA is switched to either V or H input of an OMT and then to the antenna with two identical receiver RF path. 4.10f) uses one antenna, and the transmitter path is the same as 4.10e), but uses a switch to switch either V or H receiver path. For all of these approaches, the DCE, PCU, ICE, ACE and Calibration Unit are all still required, although their capabilities may have to be expanded.

Approach a) is the most straightforward and has the best isolation between V and H channels. It also has no additional RF insertion losses. However, it requires two sets of RF components and two antennas. Also, the transmit power is doubled if the same transmit power per pulse is used. This would need more overall power consumption.

Approach b) requires only one antenna but the OMT has less isolation than two antennas and has additional insertion loss. This reduces the HPA output and increases the receiver noise figure.

Approach c) has one HPA, but an additional splitter which adds insertion loss in the transmit path only. The transmit power is reduced by the splitter and the OMT while the receiver noise figure is increased by the OMT loss.

Approach d) has only an additional polarizer over the baseline system, which adds insertion loss. This reduces the transmit power and increases the receiver noise figure. However, the transmit pulses must be shared between V and H polarization. This means that the number of looks must be reduced or the resolution must degrade.

Approach e) has one HPA which is switched to a V or H polarization path. The receiver selects the V or H signal as appropriate. In this approach, the number of samples per polarization is divided by two.

Approach f) has one HPA which is switched to a V or H polarization path. The receiver V or H polarization is selected by using a switch alternatively.

Approach a), b), c) and d) are simultaneous, while e) and f) are sequential. All approaches require calibration for 2 channels and all except f) need data processing for 2 channels.

In approach a) the total HPA power is doubled for the same performance. Alternatively, the performance is degraded by 3 dB for the same total power. In approach b) the OMT loss affects both the transmit power and receiver noise figure. If the OMT loss is 1 dB, then the performance loss relative to the baseline system is 2 dB for the same total HPA power. For approach c), there is an additional splitter loss in the transmit path only. If the splitter loss is 1 dB (on top of the 3 dB for the splitter function) the performance loss will be 3 dB. In approach d), the polarizer degrades the transmit power and the receiver noise figure. If the polarizer loss is 1 dB, the performance loss is 2 dB. However, the number of looks is lower than for the baseline system. In approach e), if the switch loss is 1 dB, the transmit power loss is 2 dB while the receiver noise figure increases 1 dB relative to the baseline system. In approach f), the transmit power loss is the same as approach e), but the receiver noise figure increases an additional 1 dB for a total degradation of 4 dB relative to the baseline.

Overall, it is judged that approach c) offers the best combination of performance and system simplicity. However, to achieve a 0.3 dB radiometric resolution, the HPA power should be increased. It should also be verified that V to H crosstalk in the return signal is low enough that accuracy is not affected by transmitting V and H and receiving V and H at the same time.

The DCE must process two channels of information and must therefore operate twice as fast as for the baseline system. The PCU must supply the increased power for the HPA's. The ICE must interface with more modules and the complexity of the Calibration Unit must be increased.

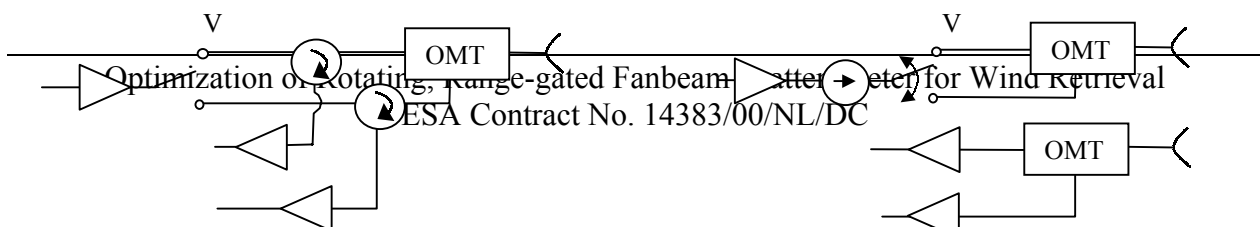
4.1.5.3.2 Polarimetric Capability (HV/VV)

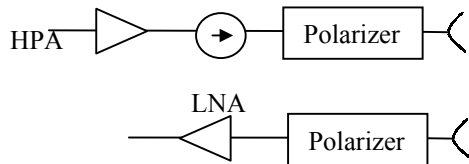
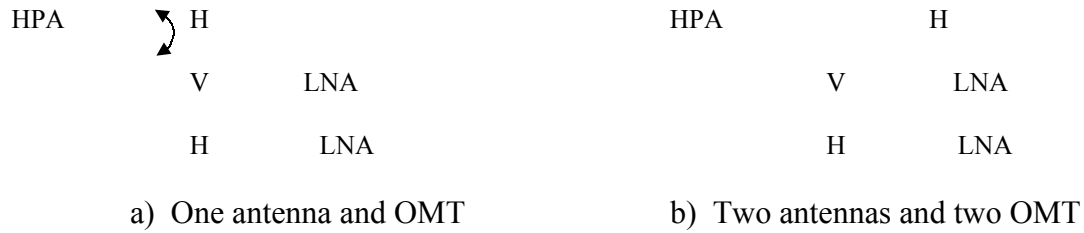
A full polarimetric capability requires the measurement of 4 quantities: VV, HH, HV and VH components. The HV and VH component have a phase as well as a magnitude. There are also several methods to implement a polarimetric capability. Figure 4.11 shows the FEE / Antenna portions of these different approaches for a full polarimetric capability.

Figure 4.11a) shows an approach using one antenna. An HPA is switched to either the V or H path and goes to a circulator, an OMT and then to the antenna. Two receive channels are taken from the other circulator ports. LNA's are used to amplify the signals prior to down conversion and processing.

Figure 4.11b) shows a two – antenna approach. An HPA drives an isolator which is switched to either the V or H input of an OMT. The output of the OMT goes to the first antenna. The receive antenna goes to OMT, whose two outputs are the V and H channels. The receive signals are amplified by LNA's.

Figure 4.11c) shows another configuration of two-antenna approach using polarizers. The signal from HPA goes to an isolator and then the transmit antenna. The polarizer is switched to alternately produce V and H polarizations. The receive antenna goes to a polarizer and then to an LNA. The polarizer is alternately switched to produce V and H polarizations.





c) Two antennas and two polarizers

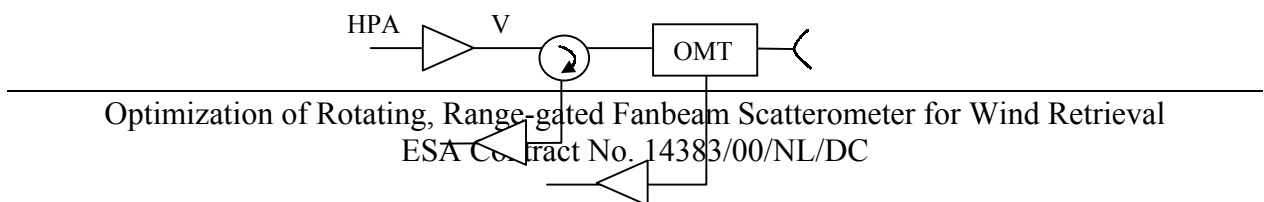
Figure 4.11 Design approaches for full polarimetric capability.

In the approach of 4.11a) the Tx power is reduced by the insertion losses of the switch, circulator and OMT. The receiver noise figure is degraded by the insertion losses of the OMT and circulator. The total degradation is 3 dB relative total baseline system. For 4.11b), the Tx power is reduced by the insertion losses of the isolator, switch and OMT while the receiver noise figure is degraded by the insertion loss of the OMT. The total degradation is 2 dB. In 4.11c), the Tx power is reduced by the insertion losses of the isolator and polarizer while the receiver noise figure is reduced by the polarizer insertion loss. The total degradation is 1 dB.

All of the approaches have two receiver channels which process the V and H signals. The DCE must operate at double the rate of the baseline system. Calibration is needed for 4 channels. It should be noted that the polarization of the transmit signal must be switched alternately to V and H to be able to cross-polarization components from the like-polarization components. This means that either the number of azimuth looks is divided in half or the resolution cell size is doubled. This is a serious disadvantage since the cross-polarization levels are already small and will therefore have a very low signal to noise ratio.

The approaches which use two antennas generally have slightly better performance than the single antenna approach. Nevertheless, the single antenna approach has a lower weight and is selected as the preferred system. The system also requires the RFE, DCE, PCU, ICE, ACE and Calibration Unit.

The requirement to transmit V and H pulses alternately is a serious drawback. However, in order to remove ambiguous solutions for the wind direction, it may only be necessary to measure the VV and HV components. In this case, the simpler system of Figure 4.12 could be used.



V LNA
H LNA

Figure 4.12 Partial polarimetric system (HV, VV).

This system contains no switching as only V pulses are transmitted while V and H signals are detected. The system has lower losses than a full polarimetric system (2 dB relative to the baseline for VV) and does not have a reduction in the number of looks. It needs calibration for 2 channels and the data processing must operate at a double rate.

4.1.5.3.3 Operation at Two Frequencies

Approaches for a two frequency system are illustrated in Figure 4.13. Only the FEE / Antenna portions are shown.

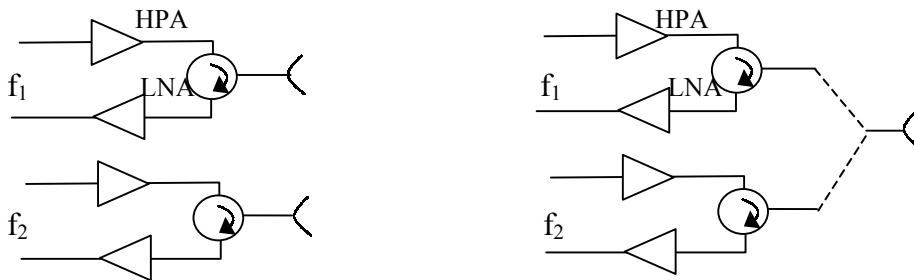


Figure 4.13: Two frequency system.

Figure 4.13a) shows a two antenna system, while Figure 4.13b) uses one antenna with a dual feed. The systems both use double sets of FEE and RFE equipment and there is no performance degradation relative to the baseline. The DCE operates at double the rate of the baseline system and calibration is needed for 2 channels. The PCU, ICE, ACE and Calibration Unit are needed for both systems.

The single antenna unit is preferred because of its lower complexity and lower weight. The performance of both approaches is very similar.

4.1.5.3.4 Two Beam System

Two approaches to a two antenna system are shown in Figure 4.14. The two antennas are placed on opposite sides of the satellite to increase the number of acquisition.

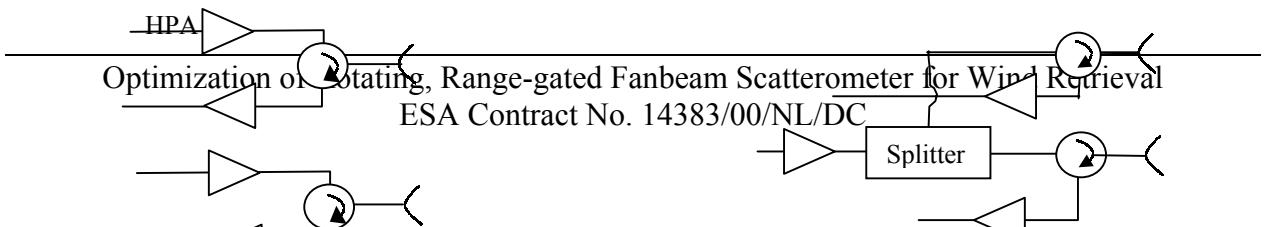




Figure 4.14 Two antenna system.

In some of the other system approaches, two antennas were used for transmitting and receiving. Here both antenna transmit and receive. In Figure 4.14a) two HPA's are used. In figure 4.14b) one HPA providing about twice the power is used together with a power splitter. The power splitter causes a 1 dB performance degradation. The choice is between two smaller HPA's and a larger HPA plus splitter. Both systems need calibration for 2 channels and the data processing must be at a double rate. The best system in this case can be decided only during the detailed design of the equipment.

4.1.5.3.5 Implementation of Recommended Enhancement – Dual Polarization (VV, HH)

Figure 4.15 shows a block diagram of the implementation of the recommended dual polarization system. The RFE must have two receive channels. The DCE could have either two receive channels or sample both channels and operate at double speed. The PCU will have to supply more power and more interfaces need to be controlled.

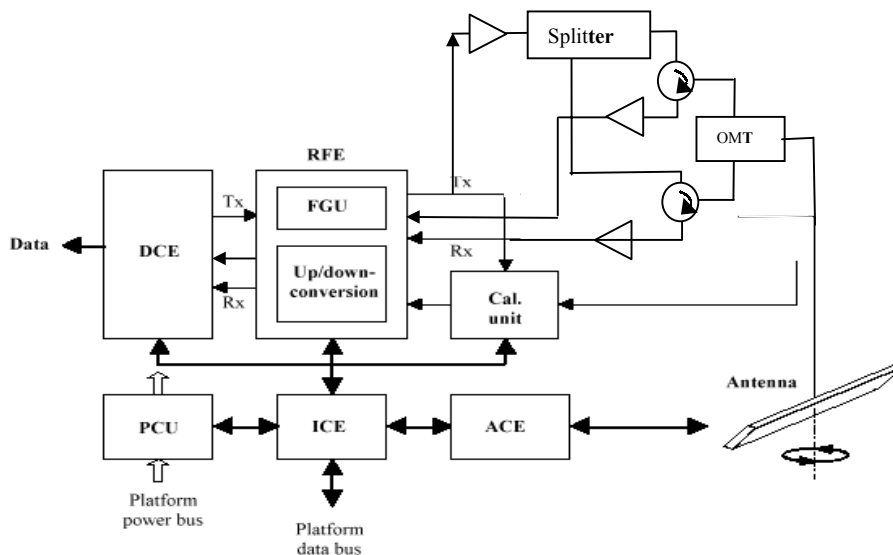


Figure 4.15 Implementation of recommended dual polarization system (VV, HH).

4.1.5.3.6 Implementation of Partial Polarimetric System

Figure 4.16 shows a block diagram for the implementation of the partial polarimetric system which was proposed as a potential alternative enhancement if the SNR is acceptable for cross-polarization signals. It has one transmit channel and two receive channels. The DCE in this system must also process two channels but the system does not require a large increase in transmit power and the PCU requirements will not change greatly.

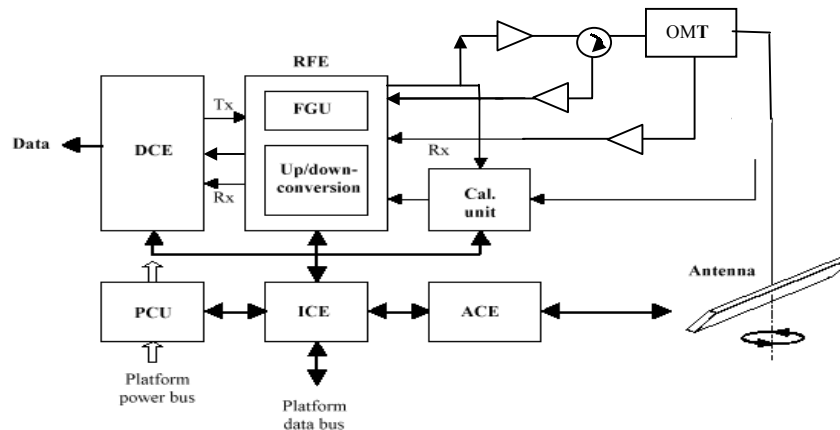


Figure 4.16 Implementation of recommended partial polarimetric system.

4.2 Review of scatterometer performance

Radar backscattering from the ocean surface is anisotropic, therefore the measurement geometry is important to precisely determine its directional behaviour. The swath of the proposed RFSCAT is nearly symmetric to the ground track of the satellite, thus in the following the term swath is used only for the area covered by the instrument on one side of the ground track. The measurement geometry varies considerably across this swath as can be seen from Figure 4 of Attachment I of the Statement of Work. For convenience this swath is divided into three domains according to the measurement geometry:

- the inner-swath close to the ground track is covered by a wide range of incidence angles but only at 2 azimuth directions;
- the mid-swath has a AMI type of coverage with a considerable spread of azimuth and incidence angles;
- the outer-swath is covered only by look directions across track and large incidence angles.

As a consequence the wind retrieval performance is expected to be different for these domains. Though there are techniques available to extrapolate wind field information from the mid-swath to the inner and outer swath during the wind retrieval this will not be considered here. The goal is to achieve the best possible and independent wind retrieval for each resolution cell. The best wind retrieval performance can be expected in the mid-swath. The AMI aboard ERS-1/2

uses three optimally chosen azimuth looks in order to retrieve the wind direction. However, due to the nearly symmetric radar response for upwind and downwind look directions the retrieved wind directions are ambiguous. The RFSCAT provides even more azimuth looks than the AMI, which will reduce the number of rank 3 and rank 4 solutions, but this will not solve the upwind/downwind ambiguity. The dual pencil-beam scatterometer SeaWinds employs both VV- and HH-polarisation. Due to different azimuthal response at the different polarisations the upwind/downwind ambiguity can be resolved in many cases, leading to 80% rank 1 solutions (Stoffelen and Voorrips, 1999; Figa and Stoffelen, 2000).

At the inner swath measurements are performed at two opposite look directions but several incidence angles. At a single radar frequency this incidence angle diversity will not provide sufficient independent information in order to solve the ambiguities. Here it is necessary to study the impact of another polarisation and/or frequency in detail. At the outer swath the wind retrieval will be problematic. Additional information to the NRCS measurements at a single azimuth and incidence angle is necessary. How this can be achieved by employing different polarisations and frequencies is being studied. Baseline of the proposed RFSCAT is a C-band VV-polarisation system for the following reasons:

- The GMF for wind retrieval is well known.
- Lower frequencies are not suited for this application since the sensitivity of the NRCS to wind speed decreases significantly with radar frequency.
- Higher frequencies (X- and Ku-band) are more affected by rain and water vapour in the atmosphere.
- This will ensure the continuation of a homogenous climatological data set, which started with ERS-1 in 1991, followed by ERS-2 and the METOP series.
- This continuation is also important for other climatological applications of the scatterometer data dealing with snow, ice and land surfaces. Although this not of interest in this study other emerging applications of scatterometer data should be kept in mind in the instrument design.

Adding an HH-polarisation channel is technically the most effective way to gather additional information. Presently there is no GMF for C-band and HH-polarisation available, however a first model is being proposed in this report. The next logical step after having added HH-polarisation is to extend the capability of the instrument to polarimetric measurements. Polarimetric airborne radiometer data have indicated that the Stokes parameters have a different azimuthal behaviour allowing an ambiguity free retrieval of the wind direction. No polarimetric scatterometer data over the ocean have been published so far. However based on the proposed polarimetric GMF for SeaWinds (Tsai et al. 2000) both, the Ku-band GMF NSCAT2 and the C-band GMF CMOD4 were extended to describe polarimetric radar backscatter as well.

4.2.1 Literature survey to extend the GMF

The first model to be used in this study is CMOD4, a GMF for C-band VV-polarisation, which is presently being used for operational wind retrieval from ERS-2 scatterometer data (Stoffelen and Anderson, 1997). Though there might be a need for further improvements especially for high wind speeds (Donnelly et al. 1999) this is out of the scope of this project. Therefore, literature considering only C-band radar backscatter at VV-polarisation were not be taken into account.

The second model that is being used is NSCAT2, a GMF for K_u -band VV- and HH-polarisation, which has been used for the final reprocessing of all NSCAT data (Wentz and Smith, 1999). For the same reasons as for C-band publications concerned only about K_u -band like-polarised radar backscatter were not considered.

There are several theoretical models available which claim to describe the radar backscatter from the ocean surface on basic physical principles. However, all of them have certain empirical tuning parameters, which are used to describe the ocean wave spectrum and/or its relation to the wind. Furthermore the ocean surface is divided into different artificial scales in order to separate different scattering mechanisms and to describe the contributions from tilt- and hydrodynamic modulation of Bragg waves for explaining e.g. the up-wind down-wind ratio. The mostly used models are from Plant (1986), Donelan and Pierson (1987), and Romeiser et al. (1997). Common to all these models is that they still have significant problems in describing the azimuthal behaviour of the radar backscatter and the polarisation ratios. None of these models are suited as a GMF for this study.

Therefore, the literature survey was reduced to publications, which could help to develop an empirical C-band HH-polarisation GMF either in providing sufficient data or to allow a scaling of the NSCAT2 model to C-band. Furthermore, any information that could be obtained on polarimetric backscatter was of interest.

4.2.2 NRL Airborne Data

In the 1960s the Naval Research Laboratory (NRL, Washington, D.C.) conducted flights with a 4-frequency radar operating at 0.428 GHz (P-band), 1.228 GHz (L-band), 4.455 GHz (C-band), and 8.910 GHz (X-band) (Guinard et al. 1971). Though limited in azimuth angles and wind speeds the data are still valuable since measurements were performed at VV- and HH-polarisation.

4.2.2.1 Airborne X-Band Data of the Radio Research Laboratory, Tokyo

Masuko et al. (1986) report NRCS measurements at X- (10.00 GHz) and K_a -band (34.43 GHz) and both VV and HH polarisation. Circle flights were performed at wind speeds of 3.2, 7.9, 9.3, and 14.5 m/s and the incidence angle was varied between 0 and 70 degrees in steps of 10 degrees. Although it is not planned to develop a GMF for X-band these data are useful when scaling the polarisation ratio of the K_u -band NSCAT2 model down to C-band.

4.2.2.2 DUTSCAT

A multi-frequency dual-polarisation set of airborne scatterometer data were obtained by the Delft University of Technology with the DUTSCAT during the TOSCANE-2 campaign of ESA in 1987 (Unal et al. 1991; Snoeij et al. 1992a). The system operated at 1.2 GHz (L-band), 3.2 GHz (S-band), 5.3 GHz (C-band), 9.65 GHz (X-band), 13.7 GHz (K_u -band) and 17.25 GHz (K_u -band). Unfortunately, due to an amplifier failure the X-band system was not well calibrated. NRCS measurements over the ocean were made during circle flights for a range of incidence angles and for VV- and HH-polarisation. During 10 flights the wind speed ranged between 3 and 13 m/s whereby 5 flights were done at 10 m/s and the other 5 flights at 3, 5, 8, 9, and 13 m/s. This distribution of wind speeds has to be considered when discussing the wind speed dependence of the polarisation ratio derived from this data.

4.2.2.3 SAXON-FPN

This data set was obtained by the University of Massachusetts during the SAXON-FPN experiment on the Forschungsplattform NORDSEE (FPN) in November 1991 (Plant and Alpers, 1994a, 1994b). Polarimetric backscatter measurements were made at X- and C-band. Keller et al. (1989) have investigated the problem of measuring the ocean radar backscatter as function of azimuth angle on this research tower due to disturbances of the airflow by its structure. Therefore, only data within a $\pm 90^\circ$ sector from the upwind look direction were used but, on the other hand, a wide range of incidence angles (20° to 70°) and of wind speeds (5 m/s - 20 m/s) were covered. Both scatterometers employed on the FPN used two separate antennae for H and V polarisation in order to achieve maximum isolation between the polarisations. Due to the relative large physical distance between the antennae feeds for V- and H-polarisation the phase signal was extremely noisy and the phase between VV, HH, and VH radar backscatter could not be retrieved. Nevertheless, the magnitude of the radar cross section at different polarisations could be measured very accurately, especially at cross-polarisation. This allows to determine the depolarisation ratio which is defined as the ratio of the cross-polarised cross section to the like-polarised cross section and is denoted χ_v when the like-polarised cross section is VV and χ_h when it is HH.

4.2.2.4 SIR-C/X-SAR

The Spaceborne Imaging Radar-C, X-Band Synthetic Aperture Radar (SIR-C/X-SAR) was flown on Space Shuttle Endeavour for two ten-day missions in April and October 1994. The system acquired radar imagery simultaneously at L-, C-, and X-band. The L- and C-band SAR were fully polarimetric, while the X-band SAR operated at VV polarisation only. For details about the system and mission see the special issue on SIR-C/X-SAR of IEEE Transactions on Geoscience and Remote Sensing (IEEE, 1995). Within the ESA POLRAD'96 campaign also SIR-C images have been analysed (Wisnmann, 1997) and the results were used herein.

4.2.2.5 HELISCAT

The HELISCAT scatterometer of the Institute of Oceanography of the University of Hamburg measures simultaneously at the five microwave frequencies 1.0 GHz (L-band), 2.4 GHz (S-band), 5.3 GHz (C-band), 10.0 GHz (X-band), 15.0 GHz (K_u -band) and the four polarisation

combinations VV, VH, HH, and HV. The antenna is aft-looking and can be tilted mechanically during the flight such that the incidence angle varies between 23 and 65 degrees (Wismann, 1994a). The system is not fully polarimetric, thus the phase between the different polarisations can not be measured.

Within this study radar backscatter measurements of the SAMPLEX oil spill experiment conducted in June 1992 (Wismann et al., 1993, 1998) and of underflights of the SIR-C/X-SAR in April and October 1994 (Wismann, 1994b; Gade et al., 1998) have been re-analysed. The aim of these experiments was to exploit the radar contrast of the different surfactants (difference of radar backscatter between clean ocean surface and oil/slick covered surface) as a function of radar frequency, incidence angle, and look direction relative to the wind. In this new analysis only the data collected over the clean ocean surface were considered. The polarisation ratio, ($\sigma_{HH}^{\circ}/\sigma_{VV}^{\circ}$) and the depolarisation ratios χ_v and χ_h were obtained as a function of incidence angle for different radar frequencies. The experiments were conducted only at moderate wind speeds between 6 m/s and 10 m/s which are the favourable conditions for oil spill and slick observations by radar. Therefore, it is not possible to derive any dependencies on wind speed from these data.

4.2.3 Extending CMOD4 to HH-polarisation

The polarisation ratio $\sigma_{HH}^{\circ}/\sigma_{VV}^{\circ}$ was used to scale the polarisation dependence within the NSCAT2 model to CMOD4. In order to justify this approach the dependence of the polarisation ratio on radar frequency, incidence angle, wind speed and wind direction was studied on the basis of available data and models. The extended C-band GMF is called CMOD4H.

Figure 4.17 depicts the polarisation ratio as a function of incidence angle for different radar bands. Most of the data were measured with the HELISCAT system, triangles, squares and crosses denote the up-, down- and crosswind directions, respectively. Magnified symbols indicate data obtained during the POLRAD'96 campaign of ESA by the RENE X-band radar at 40° of incidence angle (Hauser et al. 1997). The diamonds for L-, S-, C-, and Ku-band are data from Snoeij et al. (1992a) and for X-band from Snoeij et al. (1992b). The short thick line between 26 and 30 degrees incidence angle for L- and C-band are data from an analysis of SIR-C/X-SAR imagery (Wismann, 1997). The nearly straight lines for C- and X-band are results from the composite-surface radar backscatter model of Romeiser et al. (1997) for up- and down-wind. The thick solid line in all plots is a cubic polynomial fit to all data indicating a relation between the polarisation ratio and incidence angle, which is not a strong function of radar frequency. For C- and Ku-band model curves of CMOD4H and NSCAT2 are included as solid, dotted, and dashed lines for up-, down-, and crosswind, respectively.

The scatter in the HELISCAT data seems to increase with radar frequency, but this is very likely due to different measurement statistics. The footprint size is a function of antenna beamwidth, which decreases with radar frequency thus the illuminated and averaged area per data point decreases accordingly with frequency.

Figure 4.18 depicts the polarisation ratio as a function of wind speed for incidence angles of 20, 30, and 45 degrees. The thin solid, dashed, and dotted lines are for CMOD4H for up-, down-,

and crosswind, respectively. The according thicker lines were computed from parameters given by Masuko et al. (1986) for X-band while data reported by Snoeij et al. (1992a) are marked by symbols for different radar bands. There is an obvious dependence on radar frequency in the DUTSCAT data. The polarisation ratio seems to increase with radar frequency and furthermore with wind speed. The C-band data reported by Snoeij et al. do not follow the overall trend for the other frequencies. This was mentioned in the conclusions of Unal et al. (1991) and of Snoeij et al. (1992a) but was not further investigated. We have no explanation for this behaviour of the C-band data. However, the curves for CMOD4H do not significantly deviate from the experimental data.

Furthermore, the azimuthal polarisation response of CMOD4H was compared to the azimuthal polarisation behaviour of experimental data. Figure 4.19 shows plots of the polarisation difference for the upwind/downwind ratio and for the upwind/crosswind ratio for incidence angles of 20, 30, and 45 degrees. The solid lines originate from CMOD4H, the dashed line from Masuko et al. (1986) for X-band and the data points are from circle flight measurements Snoeij et al. (1992a) for different radar bands. The DUTSCAT data do not indicate a significant dependence on frequency. The polarisation difference for the upwind/downwind ratio increases with incidence angle. The curves for CMOD4H do not deviate very much from the experimental data, however at 30° incidence angle the dependence on wind speed differs slightly from the DUTSCAT data but agrees with the curve from Masuko et al. (1986) for X-band. There is no clear trend in the polarisation difference of the upwind/crosswind ratio, neither with radar frequency nor with wind speed. At 45° incidence angle the curve for DUTSCAT K_u-band has the opposite trend as all the other curves. We have no explanation for this behaviour.

In summary, the model function CMOD4H fits the available experimental data reasonably well, at least there is no major deviation from these data, which could question the suitability of this model for the envisaged task in this project.

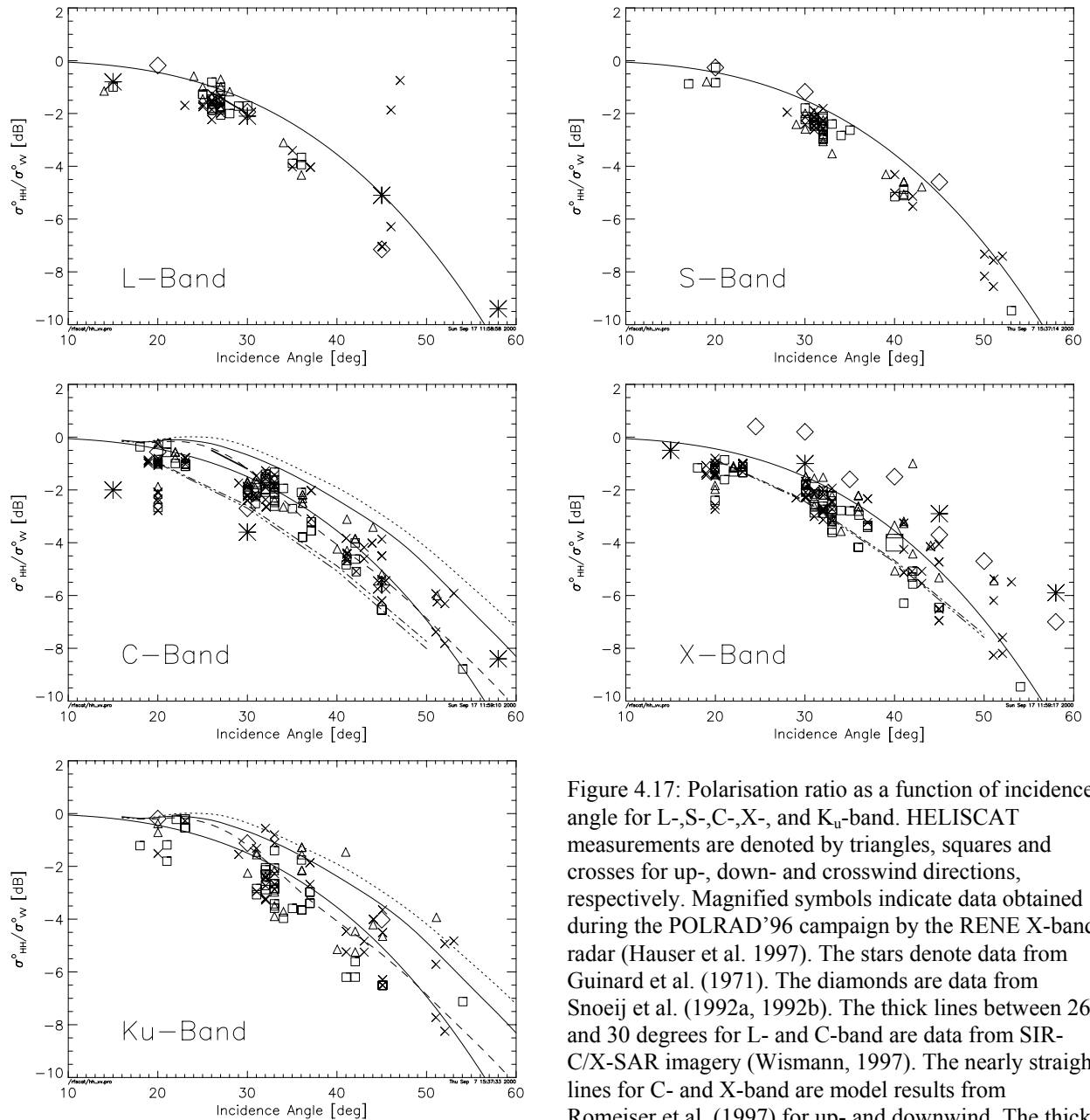


Figure 4.17: Polarisation ratio as a function of incidence angle for L-,S-,C-,X-, and Ku-band. HELISCAT measurements are denoted by triangles, squares and crosses for up-, down- and crosswind directions, respectively. Magnified symbols indicate data obtained during the POLRAD'96 campaign by the RENE X-band radar (Hauser et al. 1997). The stars denote data from Guinard et al. (1971). The diamonds are data from Snoeij et al. (1992a, 1992b). The thick lines between 26 and 30 degrees for L- and C-band are data from SIR-C/X-SAR imagery (Wismann, 1997). The nearly straight lines for C- and X-band are model results from Romeiser et al. (1997) for up- and downwind. The thick solid line is a cubic polynomial fit to all data. For C- and Ku-band model curves of CMOD4H and NSCAT2 are included as solid, dotted, and dashed lines for up-, down-, and crosswind, respectively.

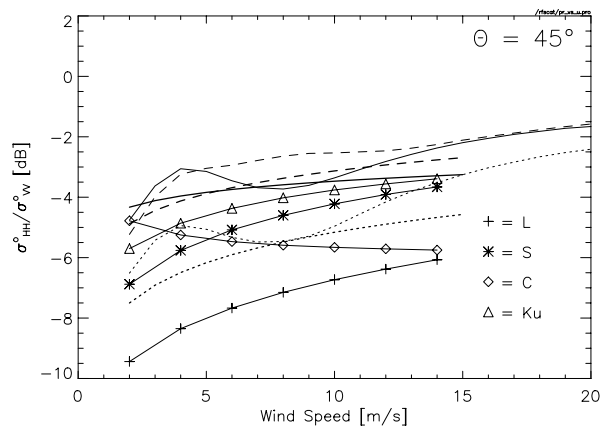
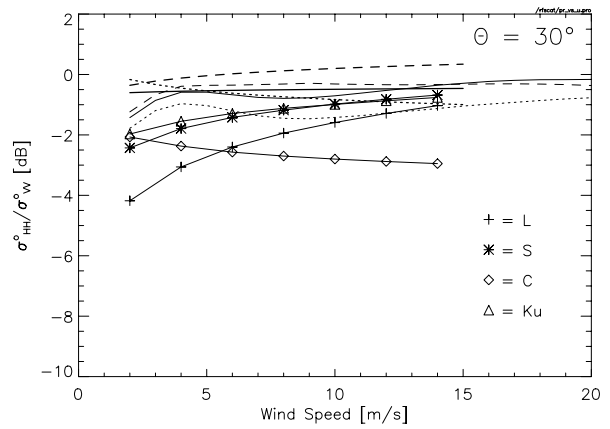
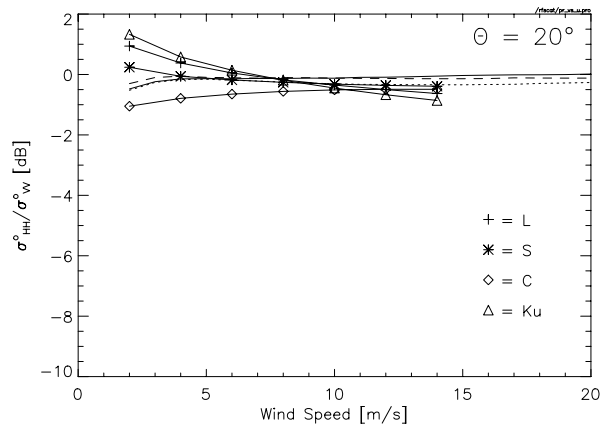


Figure 4.18: Polarisation ratio as a function of wind speed for incidence angles of 20, 30, and 45 degrees. The thin solid, dashed, and dotted lines are for CMOD4H for up-, down-, and crosswind, respectively. The according thicker lines were computed from parameters given by Masuko et al. (1986) for X-band. Circle flight data reported by Snoeij et al. (1992a) are marked by symbols for different radar bands.

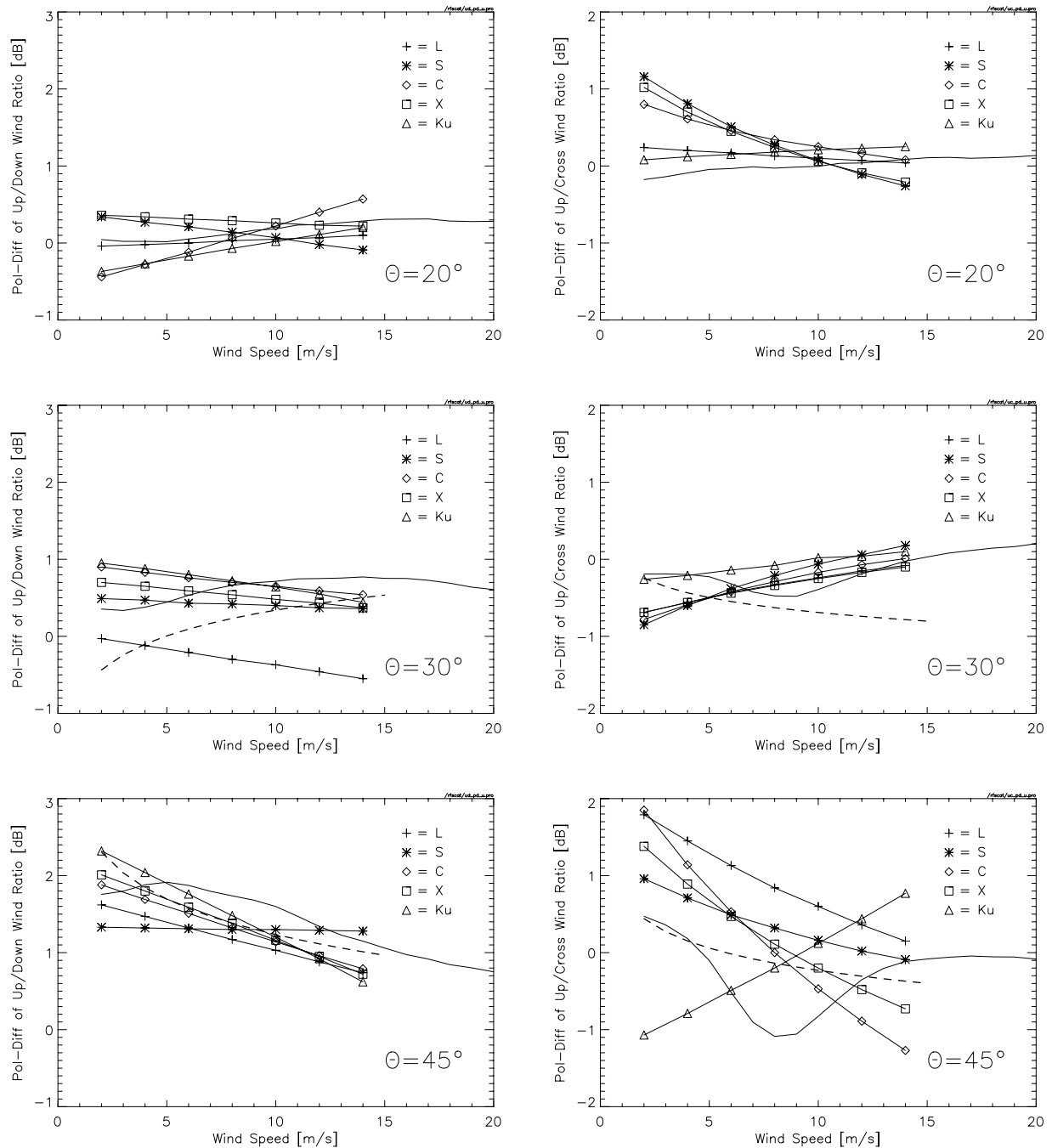


Figure 4.19: Plots of the polarisation difference of the upwind/downwind ratio (left) and of the upwind/crosswind ratio (right) for incidence angles of 20, 30, and 45 degrees. The solid lines are from CMOD4H, the dashed lines from Masuko et al. (1986) for X-band and the circle flight data of Snoeij et al. (1992a) are marked by symbols for different radar bands.

4.2.4 Extending NSCAT2 and CMOD4H to Polarimetry

To our knowledge, no polarimetric NRCS data over the ocean are published that can be used to develop an empirical polarimetric GMF or to validate theoretical models. Recently Tsai et al. (2000) published a study on a polarimetric enhancement of the SeaWinds K_u -band pencil-beam scatterometer. Their approach is based on a theoretical model of Yueh et al. (1994) which was scaled to the SeaWinds measurement geometry using the NSCAT2 model.

In order to extend NSCAT2 to the polarimetric model NSCAT2P the polarimetric correlation coefficient σ_{hvvv} was computed based on the equations given by Tsai et al. (2000) and the radar backscatter σ_{VV}^0 given by NSCAT2. Furthermore a depolarisation ratio of -15dB , a symmetry factor of 0.5 and a signal attenuation of 1.0 were chosen. The latter two tuning parameters can be used to modify the polarimetric signature until experimental scatterometer data will be available. Tsai et al. used polarimetric radiometer data to validate their model and these values were found to be appropriate to fit the radiometer measurements. The important parameter for the practical application in scatterometry is the depolarisation ratio, which is defined as the ratio of the cross-polarised to the like-polarised radar cross section and is denoted χ_v when the like-polarised cross section is VV and χ_h when it is HH. Tsai et al. used a constant value of -15 dB for χ_v which was obtained from K_u -band scatterometer data acquired with the airborne NUSCAT system of JPL. Data from other experiments and for other frequencies indicate that a value of -15 dB is reasonable, however they also indicate that χ_v might depend on incidence angle.

Figure 4.20 shows measurements of the depolarisation ratio during the SAXON-FPN experiment on the North Sea Research Tower. The depolarisation ratio does not depend on wind speed up to 20 m/s for both X- and C-band but increases significantly with incidence angle.

Depolarisation ratios were also obtained from re-analysed HELISCAT data. This data is shown in Figure 4.21 and different symbols distinguish up-, down-, and crosswind directions. Furthermore different symbol sizes are used for the SAMPLEX (small) and the SIR-C (large) experiments in 1992 and 1994, respectively. A dependence on incidence angle is not so obvious as for the SAXON-FPN data but for C-band a different incidence angle dependence was found for the two experiments. The data of each experiment allow to delineate a distinct relation between χ_v and the incidence angle. However this dependence is much stronger for the SIR-C than for the SAMPLEX experiment. The short lines in the L- and C-band plots are from an analysis of SIR-C/X-SAR imagery (Wismann, 1997). For C-band these SIR-C data agree well with the HELISCAT data for the SIR-C experiment, though the data are not collocated. The SIR-C images were acquired over the Gulf of Mexico while the HELISCAT data were collected over the North Sea. We cannot explain this difference in C-band, especially since no similarity was observed for the other radar bands. It has to be noted that measuring χ_v with a system like HELISCAT is technically challenging since a very good isolation between the antennas for V- and H-polarisation has to be achieved. According to the specification of the HELISCAT antenna, this isolation is about 20 dB but it might be less at higher frequencies. This could be the reason why for the SIR-C experiment the χ_v values for X- and K_u -band do not show the same low values as for C-band.

As a first attempt χ_v was also set constantly to -15 dB in order to be compatible with the model of Tsai et al. This value might be too optimistic in view of the RFSCAT design when considering the necessary signal to noise ratio, but any other value can be chosen and the sensitivity of the retrieval results on χ_v might thus be studied as well.

With the same method CMOD4H was extended to its polarimetric equivalent CMOD4HP, the same values for the symmetry factor, signal attenuation, and polarisation ratio were used, but σ_{VV}^0 was taken from CMOD4. Figure 4.22 depicts example plots of NSCAT2P and CMOD4HP, which were used in a first impact study for the RFSCAT design. The incidence angle is 35 degrees and the wind speed range from 4 to 18 m/s with increments of 2 m/s.

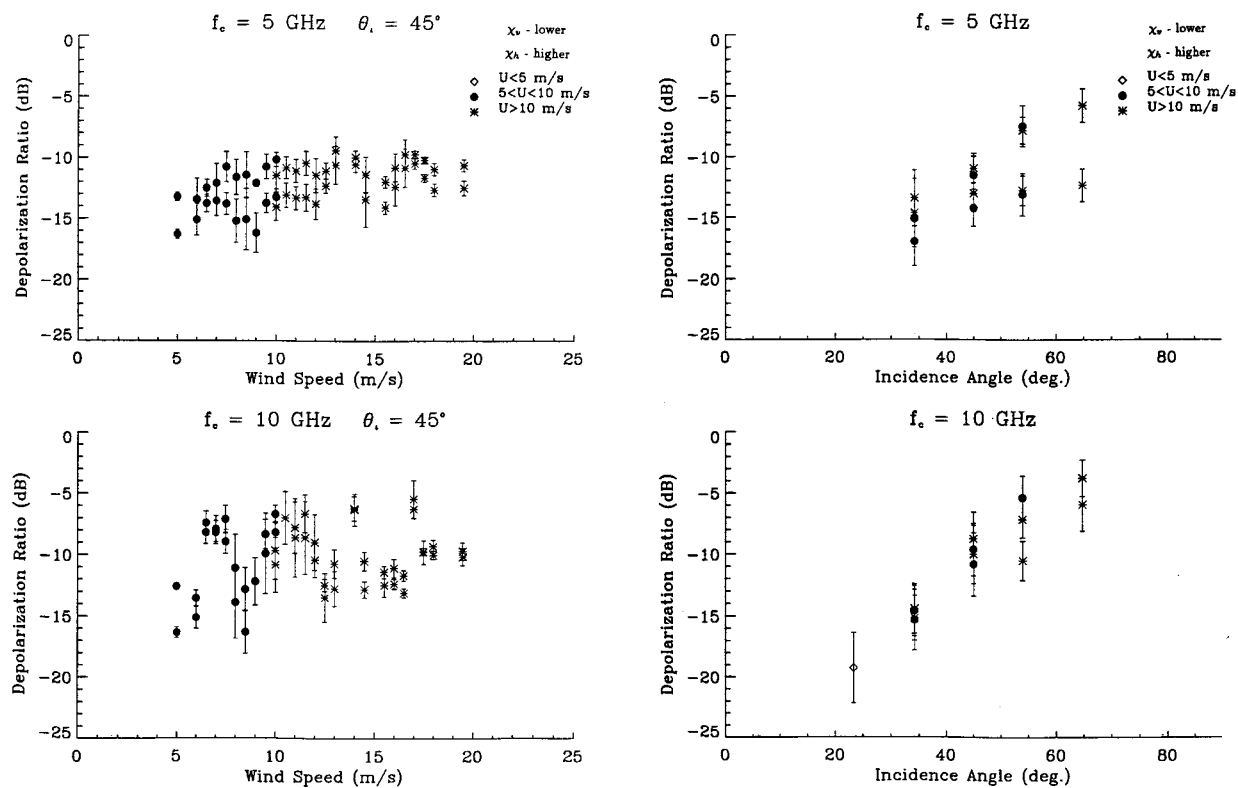


Figure 4.20: Depolarisation ratios χ_v and χ_h as a function wind speed at an incidence angle of 45° for C-band (top left) and X-band (bottom left) and as a function in incidence angle for C-band (top right) and X-band (bottom right). Measurements by the polarimetric scatterometer of the University of Massachusetts during the SAXON-FPN experiment. Plots are taken from Figures 59 and 60 of Plant and Alpers (1994b).

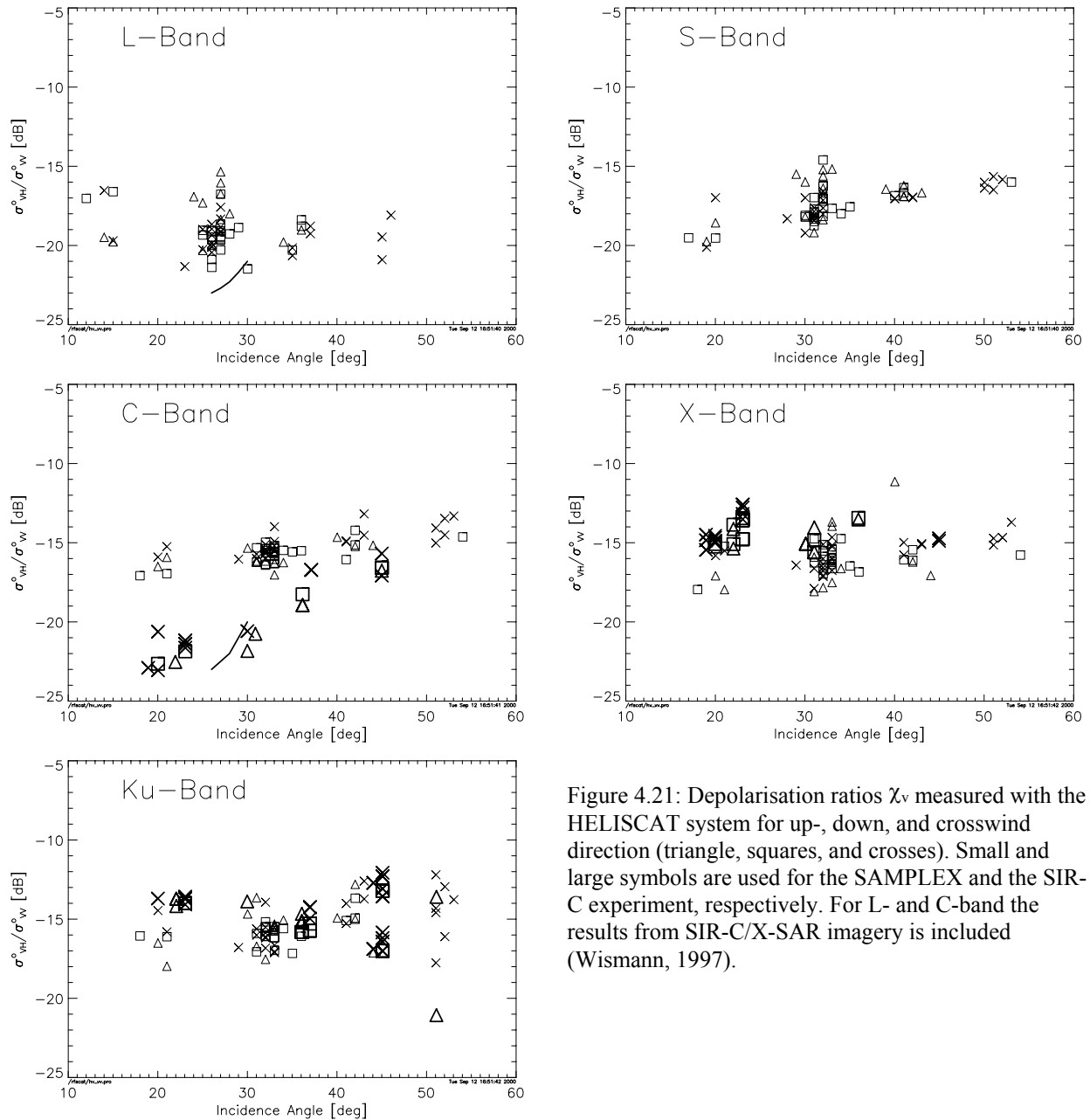


Figure 4.21: Depolarisation ratios χ_v measured with the HELISCAT system for up-, down, and crosswind direction (triangle, squares, and crosses). Small and large symbols are used for the SAMPLEX and the SIR-C experiment, respectively. For L- and C-band the results from SIR-C/X-SAR imagery is included (Wismann, 1997).

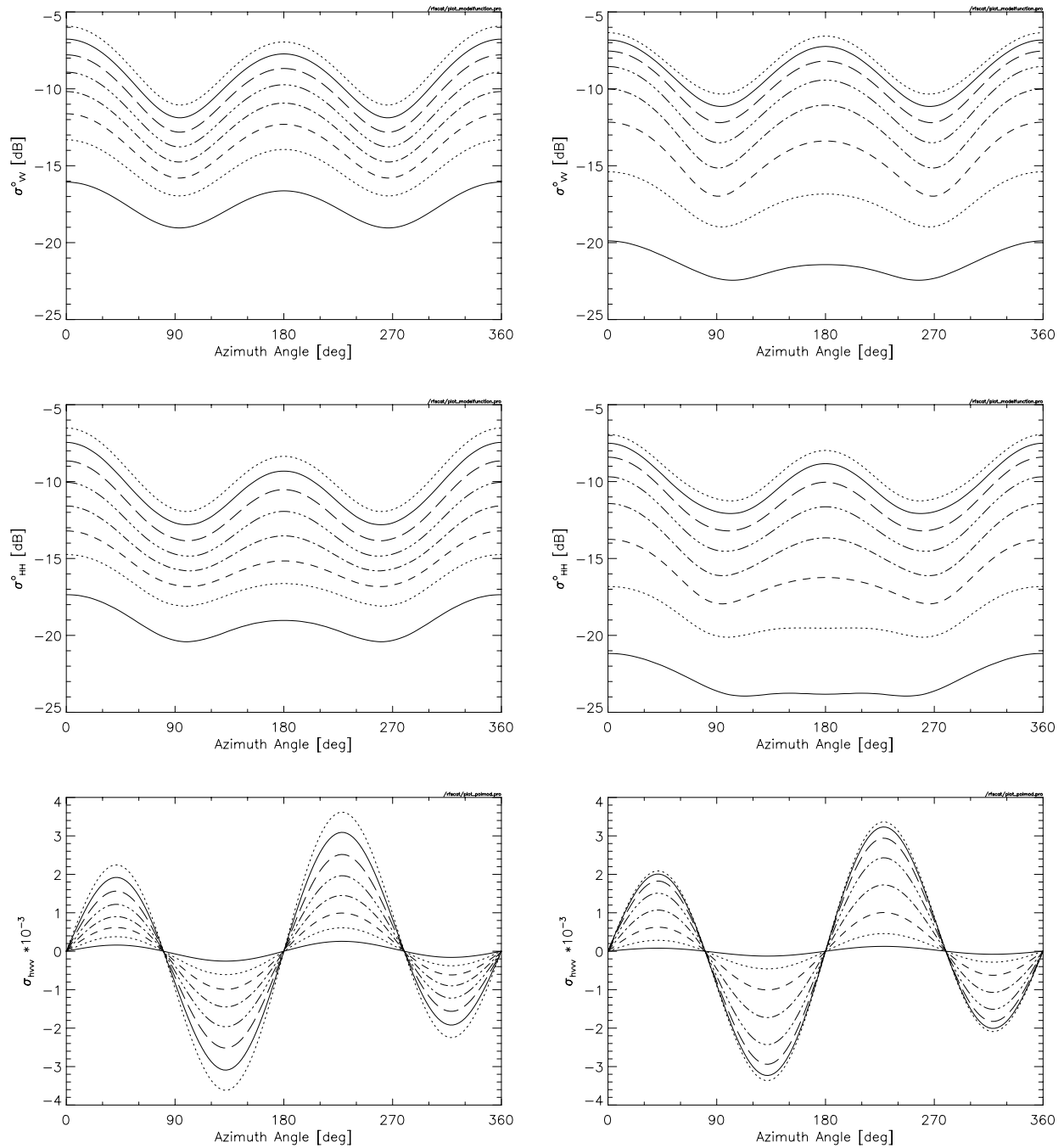


Figure 4.22: Plots of the GMF CMOD4HP (left) and NSCAT2P (right) for σ_{VV}^0 (top), σ_{HH}^0 (middle), and the polarimetric correlation coefficient σ_{hvv} (bottom) for 35 degrees of incidence angle and the wind speeds between 4m/s and 18 m/s, the ΔU is 2 m/s.

4.2.5 A first impact study

The effect of different enhancements of the RFSCAT on wind retrieval was studied, especially the impact for the inner and outer swath regions were investigated. It is assumed that the two models CMOD4HP and NSCAT2P describe reasonably well the radar backscatter behaviour with respect to measurement geometry and surface wind vector. Possible errors or shortcomings of these models will not be discussed herein. Seven different designs of RFSCAT were considered:

- (a) C-band with VV-polarisation
- (b) C-band and K_u -band both with VV-polarisation
- (c) C-band with VV-and HH-polarisation
- (d) C-band and K_u -band both with VV-and HH-polarisation
- (e) C-band polarimetric
- (f) C-band and K_u -band both polarimetric
- (g) C-band two beam, semi-polarimetric system. The inner beam transmits H and receives V and H. The outer beam transmits V and receives V and H.

The same numbering is used for the respective plots in the following figures. Furthermore, four scatterometer resolution cells with the worst expected performance in wind retrieval were selected, two in the inner and two in the outer swath, their locations are:

- 1 On the sub-satellite track, NRCS measurements were simulated at 0 and 180 degrees of radar look direction with respect to the satellite track and at incidence angles of 25 and 55 degrees.
- 2 50 km beside the sub-satellite track, the radar look directions were 10° and 170° at an incidence angle of 55 degrees and 15° and 165° at an incidence angle of 25 degrees.
- 3 50 km inside of the outer border of the swath, the radar look directions were 80° and 100° and the incidence angle was 55 degrees.
- 4 At the edge of the swath, the radar look direction was 90° and the incidence angle was 55 degrees.

The mid-swath region is not discussed here, based on the experience with NSCAT and ERS-AMI it is expected that the performance of the RFSCAT will be sufficiently good.

A wind speed of 7 m/s was used because this is the global mean wind speed and the instrument performance will be best at moderate wind speeds. Wind directions of 140 degrees and 90 degrees with respect to the sub-satellite track were considered. A wind direction of 140 degrees with respect to the sub-satellite track was selected because here the σ^0 versus azimuth curves of the GMF for VV- and HH-polarisation have the largest slope and the polarimetric GMF a relative maximum. Consequently, it can be expected that for this geometry the wind retrieval will perform best. In other words, for any other geometrical constellation the performance will

be lower, thus if an instrument enhancement does not show a significant improvement here the overall gain in wind retrieval performance will be small. A wind direction of 90 degrees gives a worst case performance.

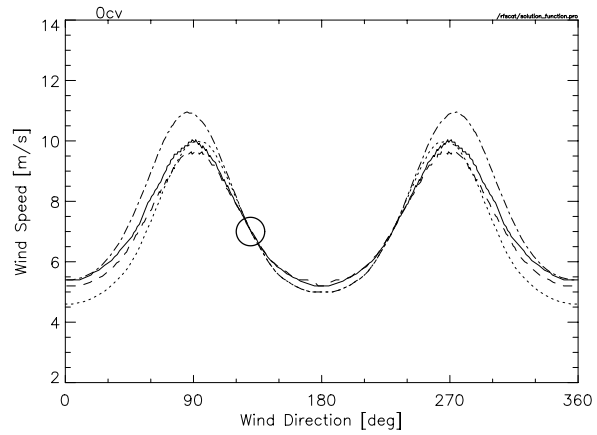
Furthermore, in this analysis a perfect system was assumed no system errors or noise were considered. This requires the end-to-end RFSCAT simulator and will be done at a later stage of this study. The GMF were inverted in order to provide the solution functions for each radar beam which are shown in Figure 4.23 to Figure 4.26 for the four cell locations across the RFSCAT swath and the six different RFSCAT designs (from (a) to (f)). Wherever the solution functions intersect a solution is found. In all plots the true solution of 7 m/s wind speed and 140 degrees of wind direction is marked with a circle. In reality the measurements will have errors, which will shift the solutions curves up and down, thus two solution curves which are still separated in these plots may not be distinguishable when considering a real system.

It is not necessary to discuss all the plots in Figure 4.23 to Figure 4.26 in detail because these figures indicate a general behaviour. Already from Figure 4.22 is it obvious that the GMF for C- and K_u -band differ only significantly for low speeds. For moderate to high winds they are very similar, C- and K_u -band scatterometers provide nearly redundant information. Thus, it can be expected that their solution curve look very similar, as shown in Figure 4.23 to Figure 4.26. As a consequence, adding a K_u -band VV-polarisation channel does not improve the wind retrieval significantly for all scatterometer cells. The gain in information is much higher when adding a C-band HH-polarisation channel, here the solution curves are much more separated for all four cells across the swath. Further adding of a dual-polarised K_u -band again will add mostly redundant information that does not contribute significantly to resolve the ambiguity problem. From Figure 4.24 and Figure 4.25 it can be seen that even a slight difference in azimuth angle already helps to separate the solution function by a respective phase shift. This is the advantage of the different look direction within the mid-swath of RFSCAT.

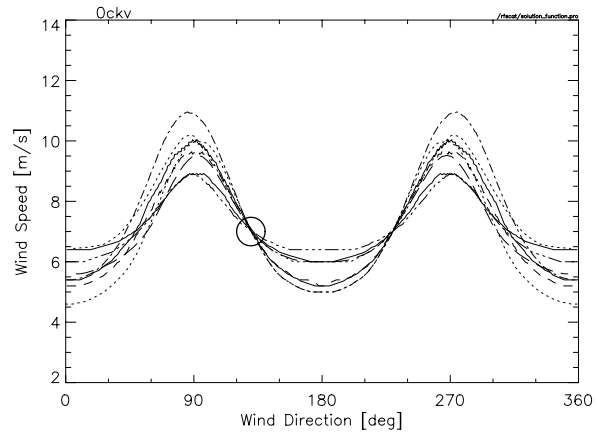
More orthogonal information is provided by the polarimetric correlation coefficient. The solution functions have a completely different shape and cover only small sectors of wind direction. Consequently, a lot of the remaining ambiguities in plots (c) and (d) can be resolved. As for the non-polarimetric systems, adding a polarimetric K_u -band provides redundant information that only increases impressively the number of solution functions (e.g. in Fig. 4.24(f)).

Figure 4.27 to Figure 4.30 show the solution functions for a wind direction of 90 degrees, which represents a worst case.

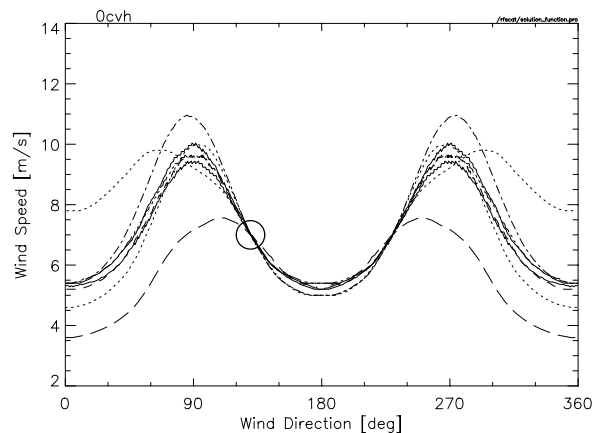
Figure 4.31 and Figure 4.32 show the solution curves for the two beam system for 90 degree and 140 degree wind directions. Both co-polarized and polarimetric cases are shown. The polarimetric operation improves the retrieval significantly without any additional costs in terms of transmitted power or reduced number of looks. Even in the worst case scenario (90 degree wind direction) only two solutions are found at the swath edge which are 180 degree apart.



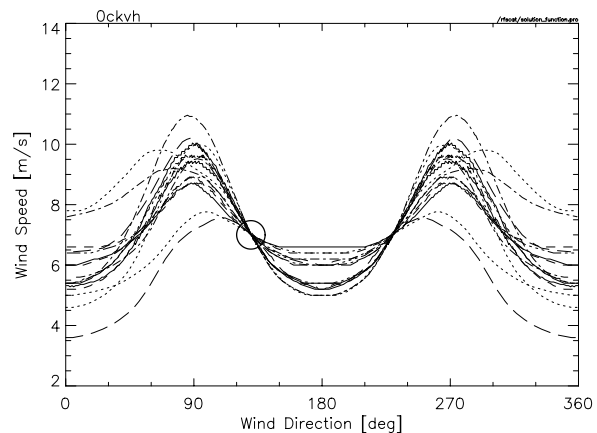
(a)



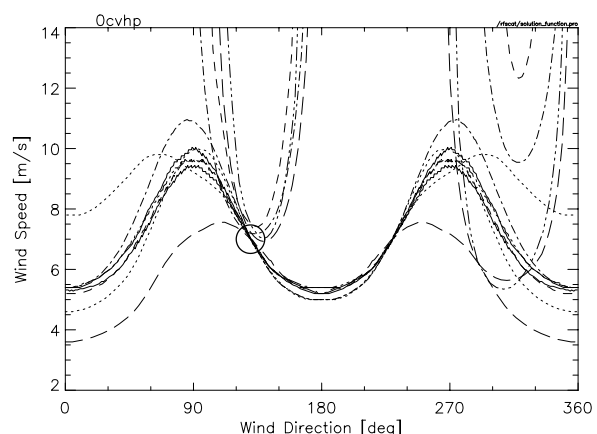
(b)



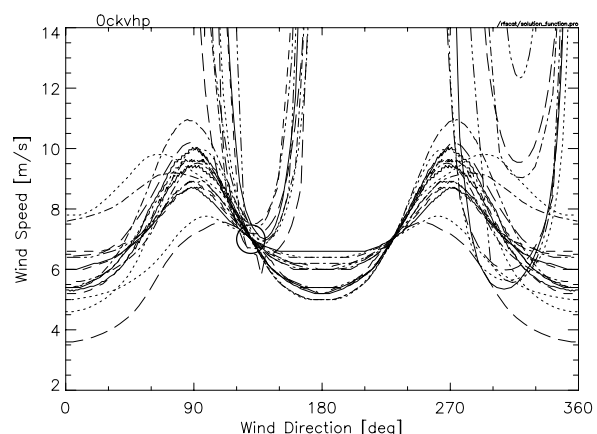
(c)



(d)



(e)



(f)

Figure 4.23: Solution functions for sub-satellite track cells. Only C-band in the left column and a combination of C- and Ku-band in the right column. From top to bottom: only VV-polarisation, VV and HH-polarisation, and a polarimetric systems. The true solution of 7 m/s wind speed and 140 degrees wind direction is marked by the circle.

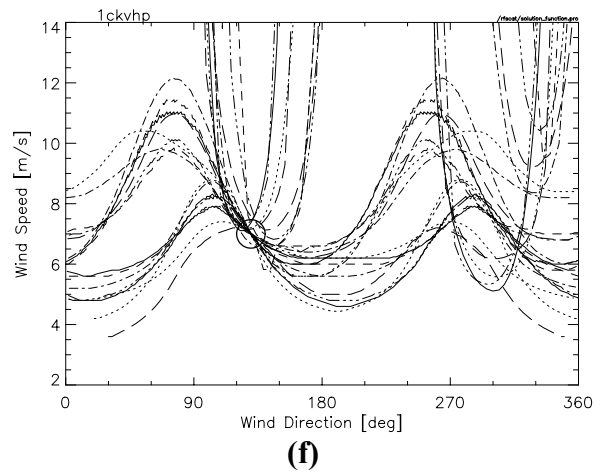
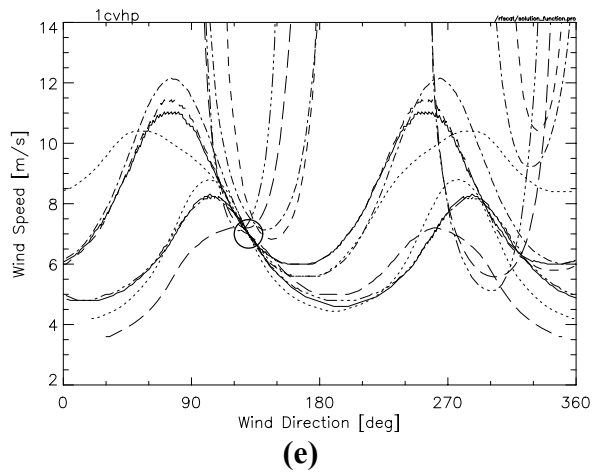
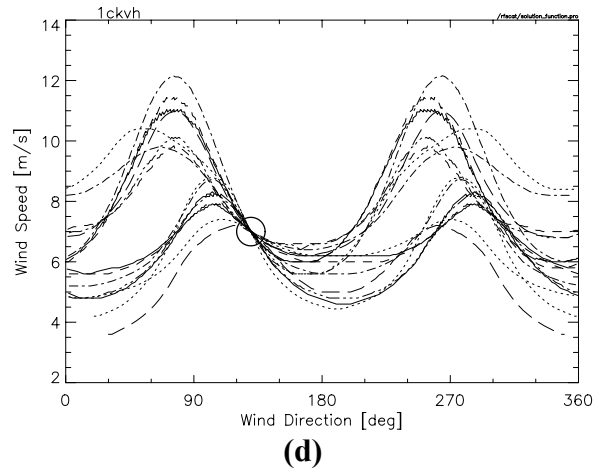
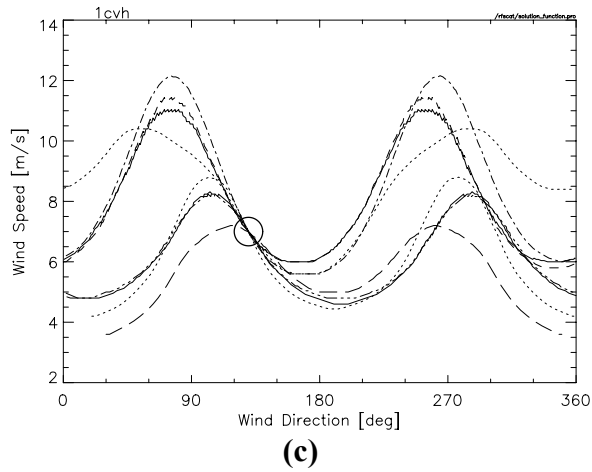
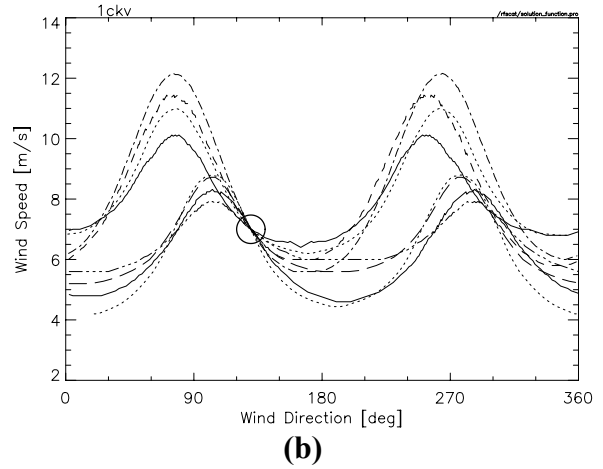
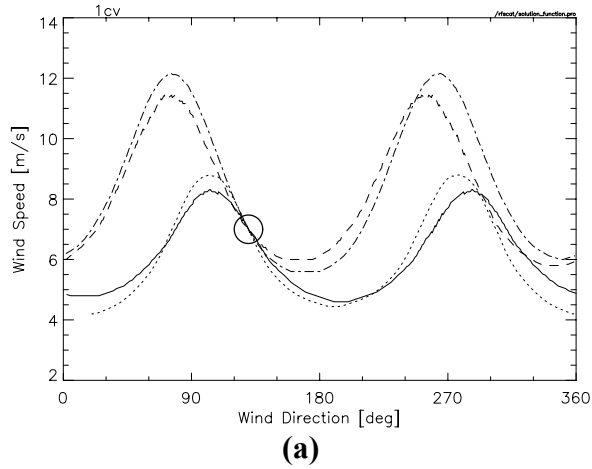


Figure 4.24: Same as Figure 4.23 but for cells being 50 km of the sub-satellite track.

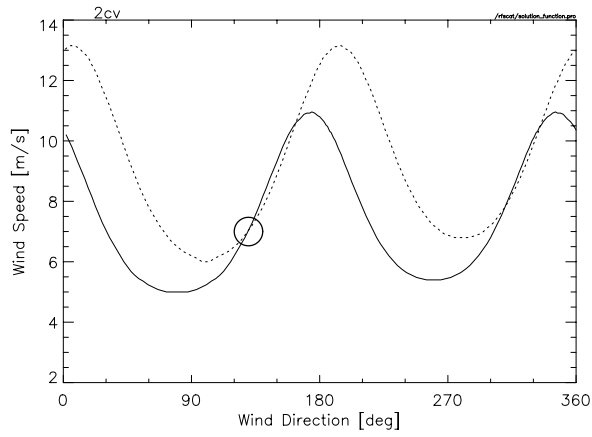
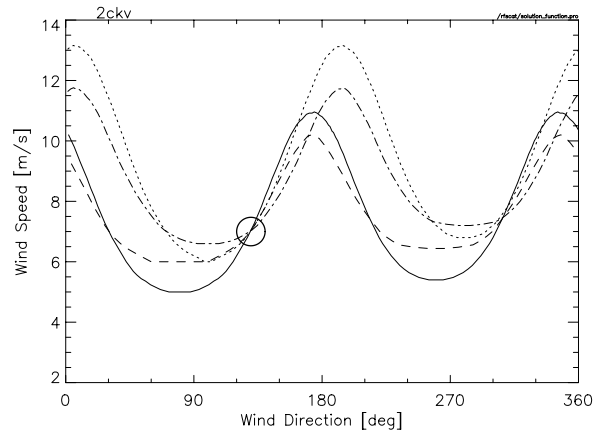
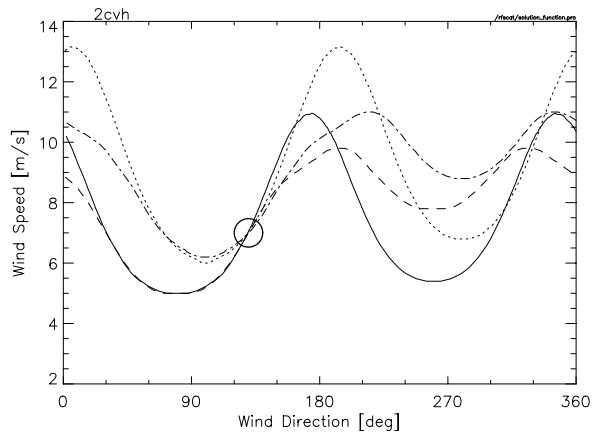
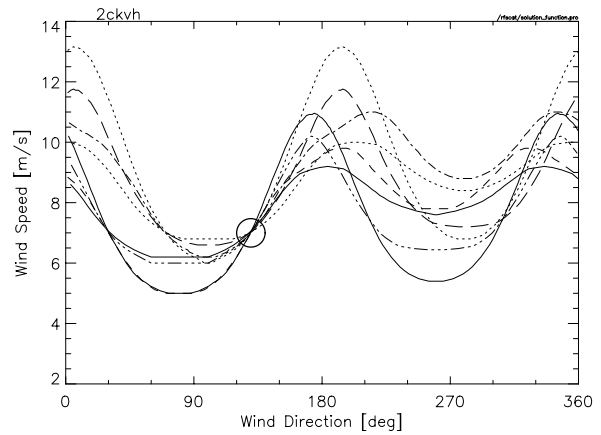
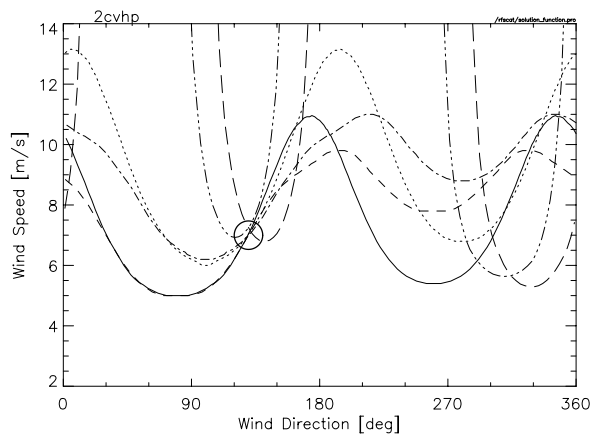
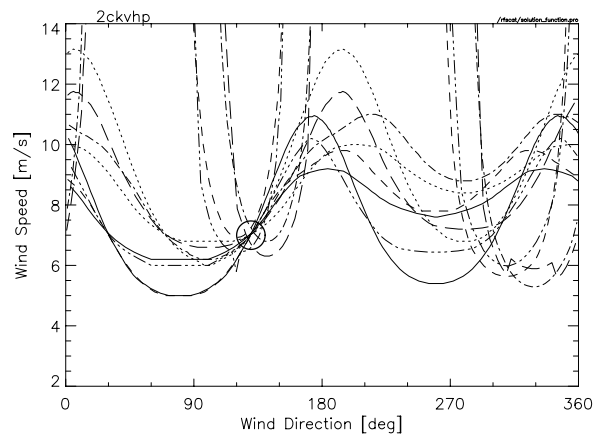

(a)

(b)

(c)

(d)

(e)

(f)

Figure 4.25: Same as Figure 4.23 but for cells being 50 inside of the edge of the swath.

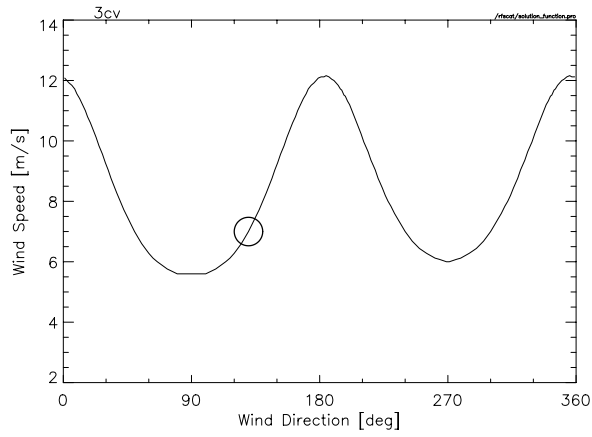
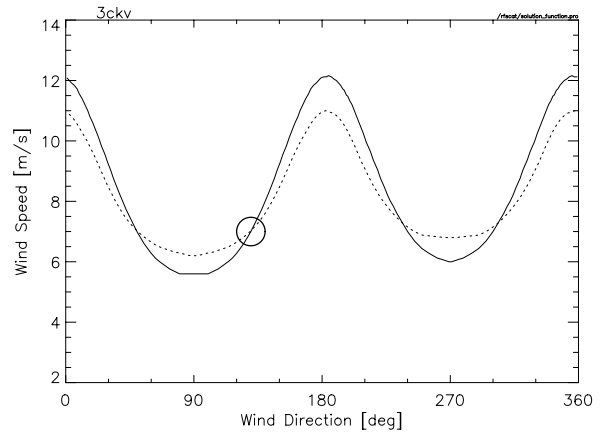
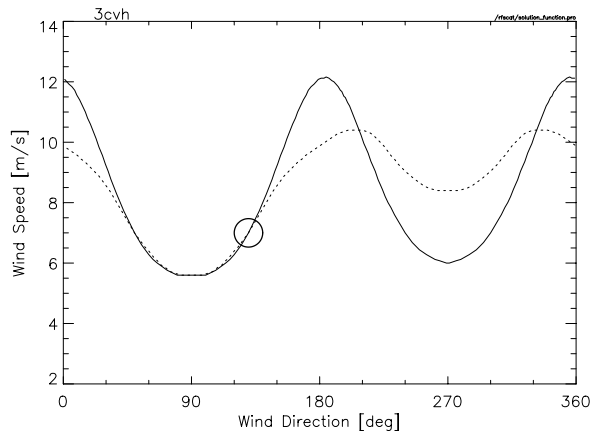
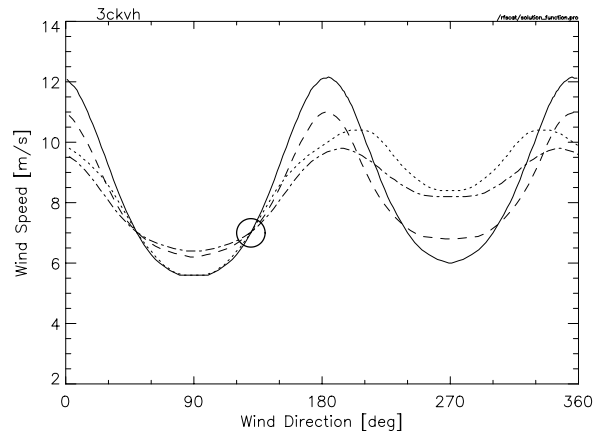
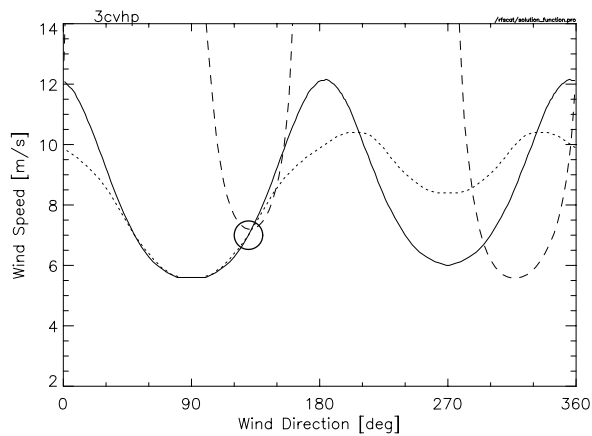
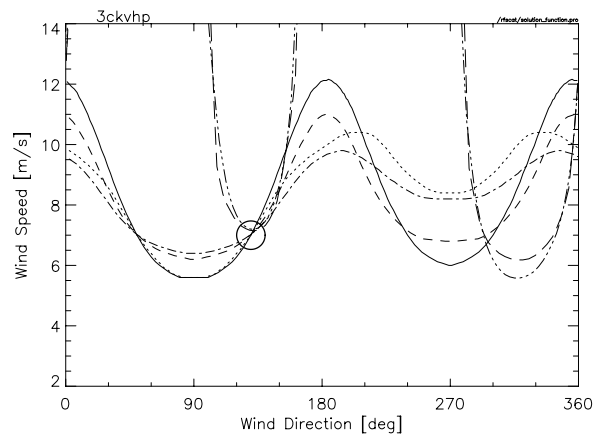

(a)

(b)

(c)

(d)

(e)

(f)

Figure 4.26: Same as Figure 4.23 but for cells at the edge of the swath.

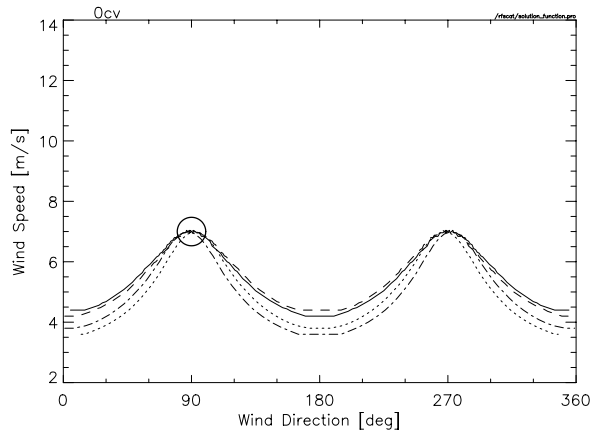
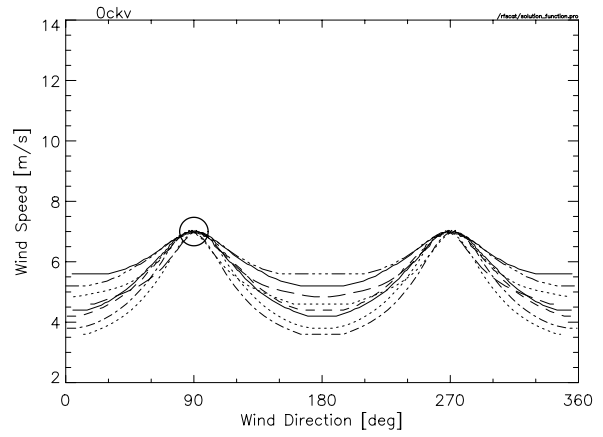
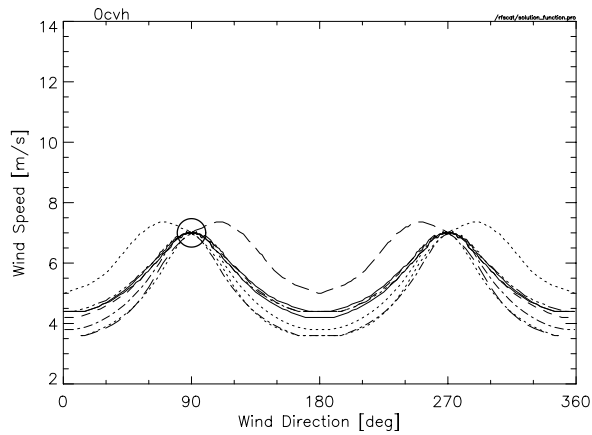
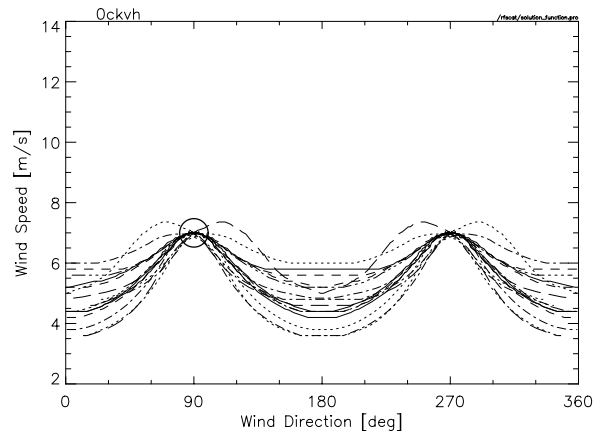
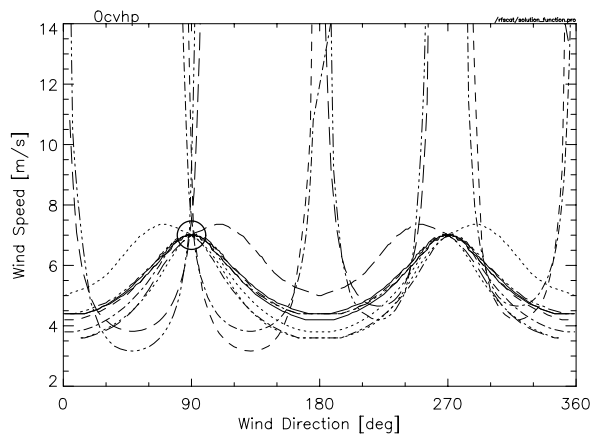
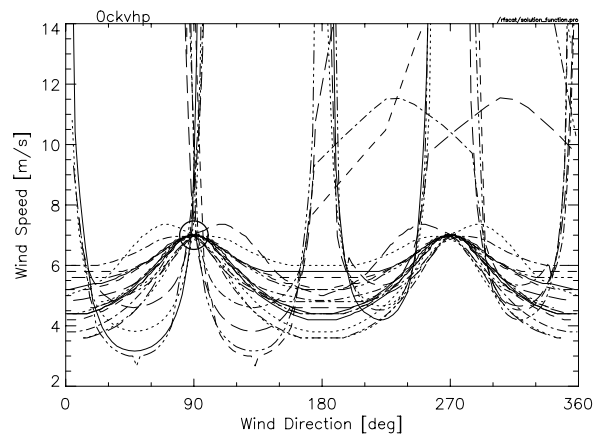

(a)

(b)

(c)

(d)

(e)

(f)

Figure 4.27: Solution functions for sub-satellite track cells. Only C-band in the left column and a combination of C- and K_u -band in the right column. From top to bottom: only VV-polarisation, VV and HH-polarisation, and a polarimetric systems. The true solution of 7 m/s wind speed and 90 degrees wind direction is marked by the circle.

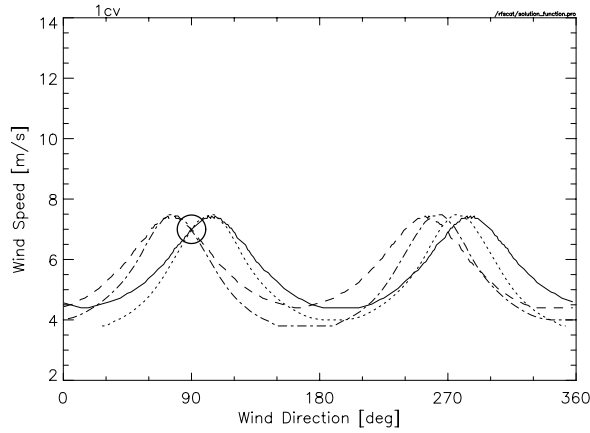
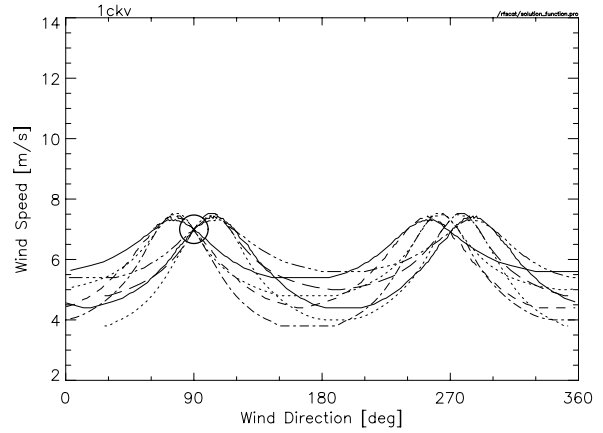
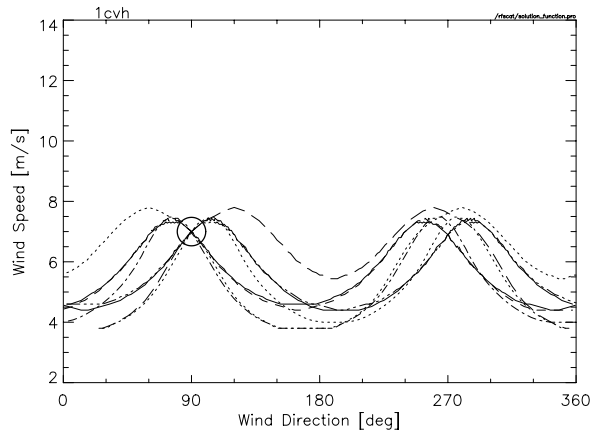
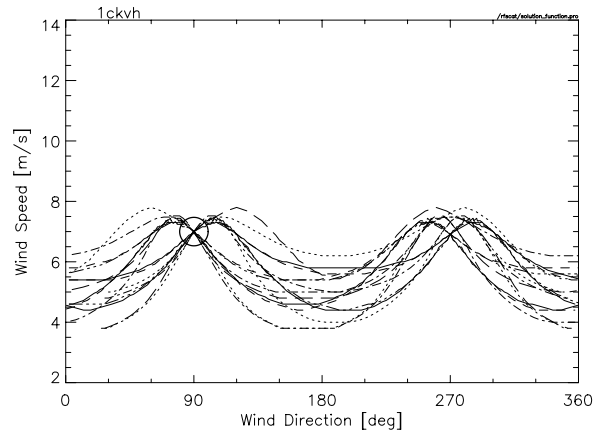
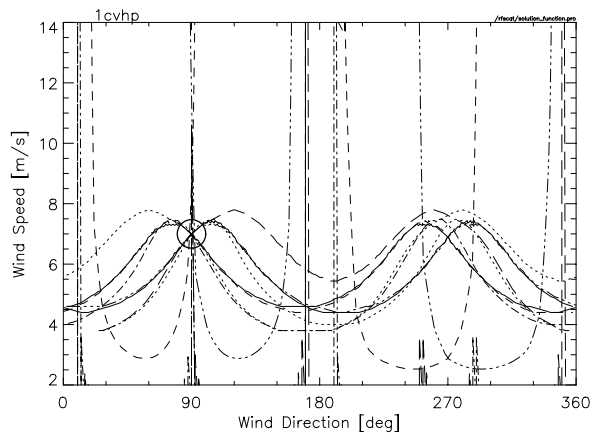
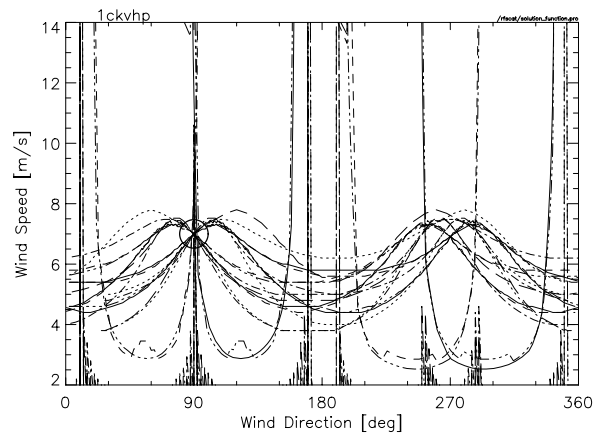
**(a)****(b)****(c)****(d)****(e)****(f)**

Figure 4.28: Same as Figure 4.27 but for cells being 50 km of the sub-satellite track.

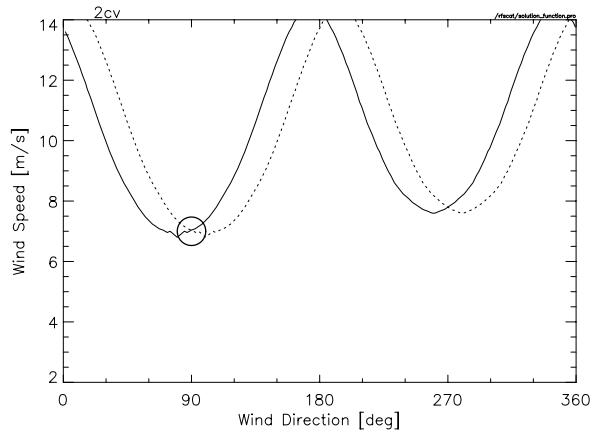
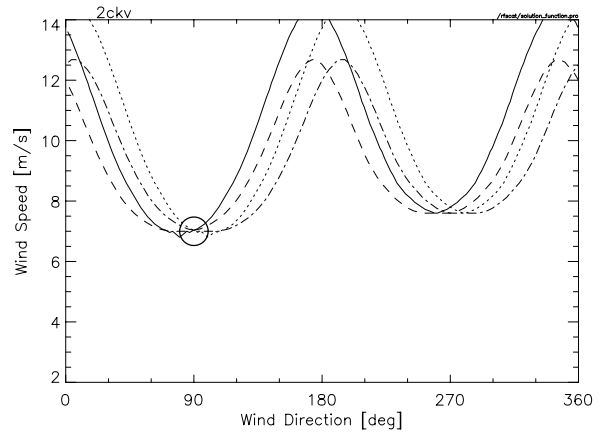
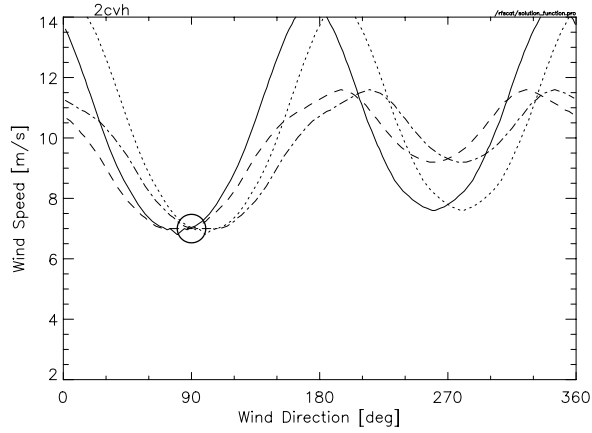
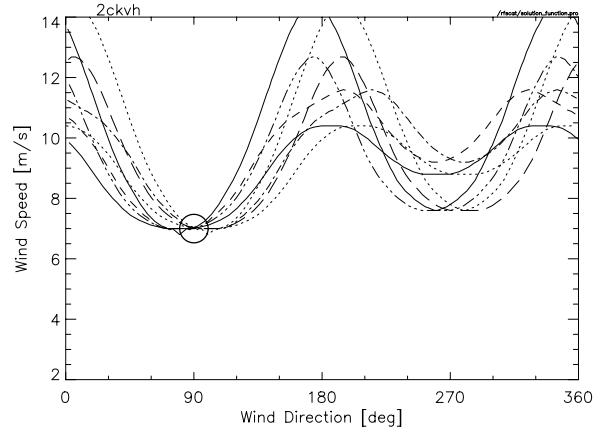
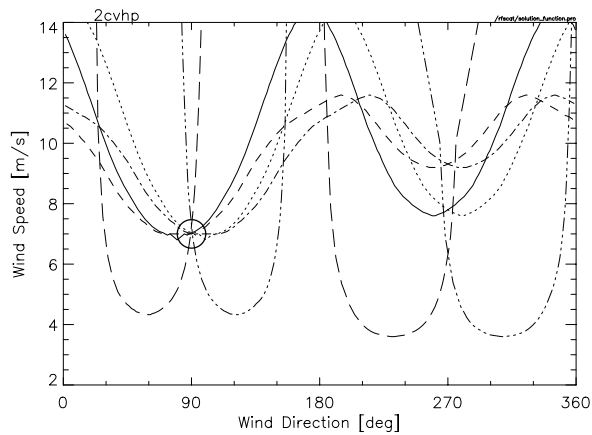
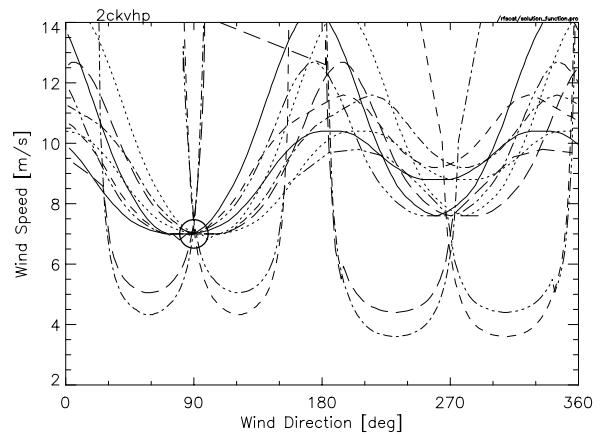

(a)

(b)

(c)

(d)

(e)

(f)

Figure 4.29: Same as Figure 4.27 but for cells being 50 inside of the edge of the swath.

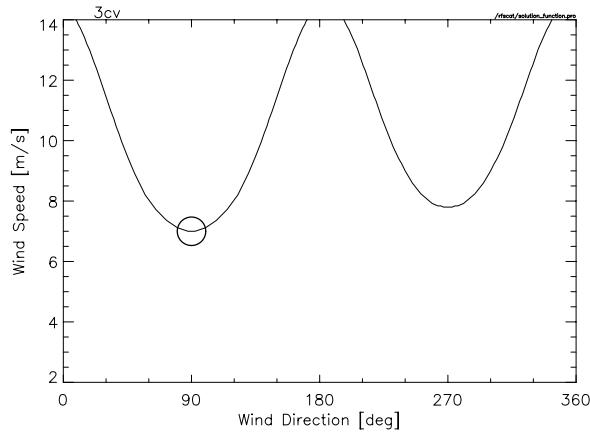
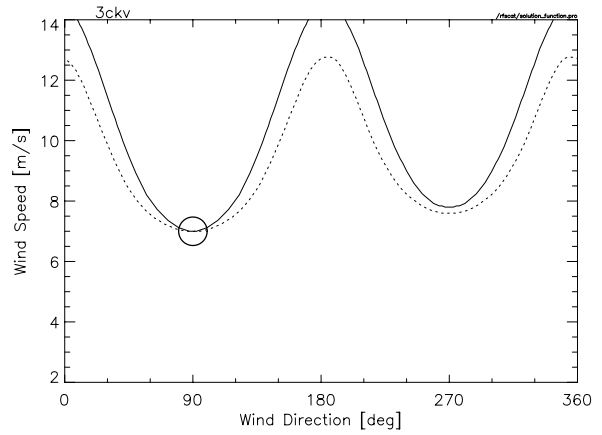
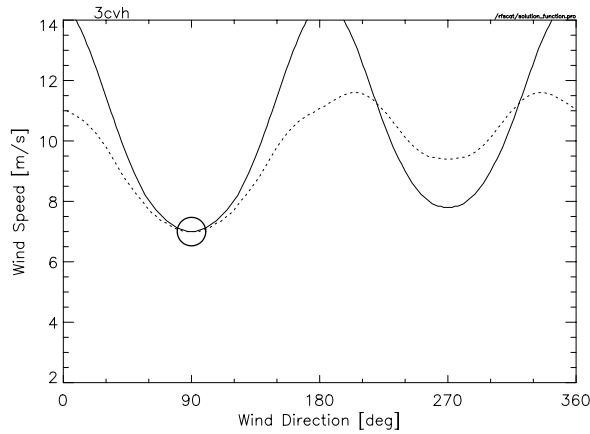
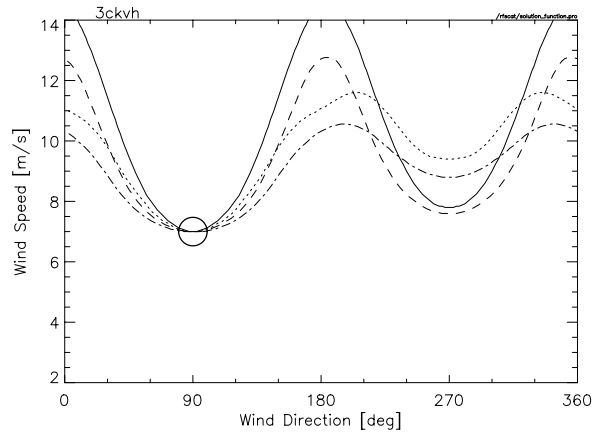
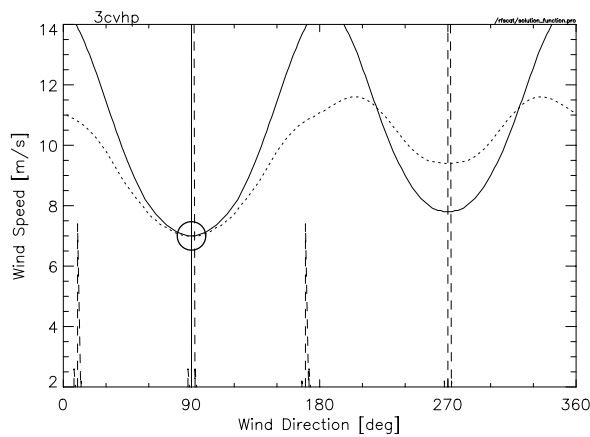
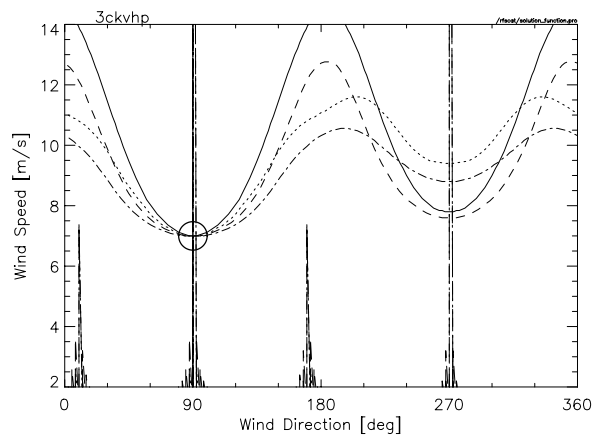
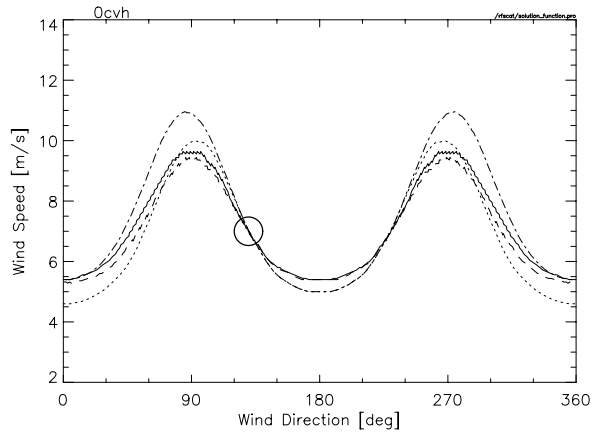
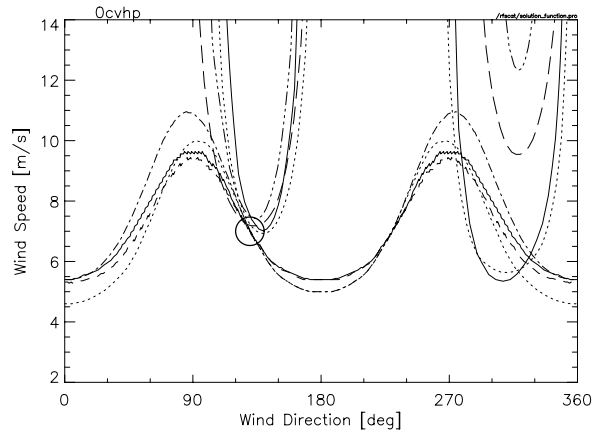

(a)

(b)

(c)

(d)

(e)

(f)

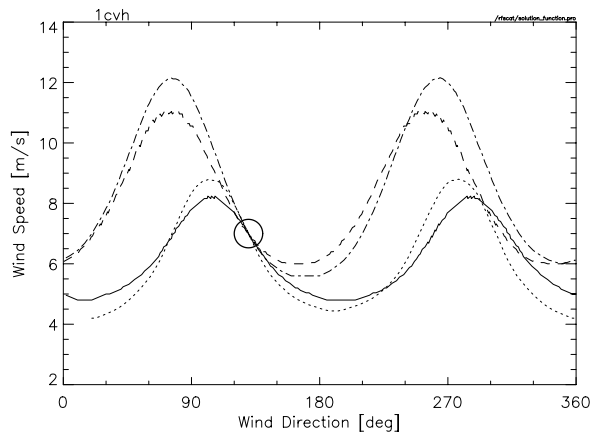
Figure 4.30: Same as Figure 4.27 but for cells at the edge of the swath.



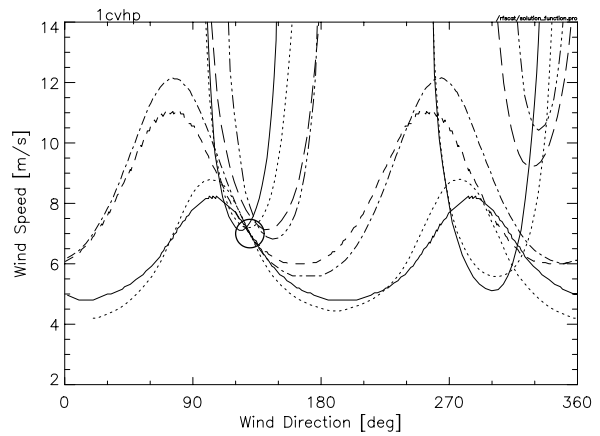
(a)



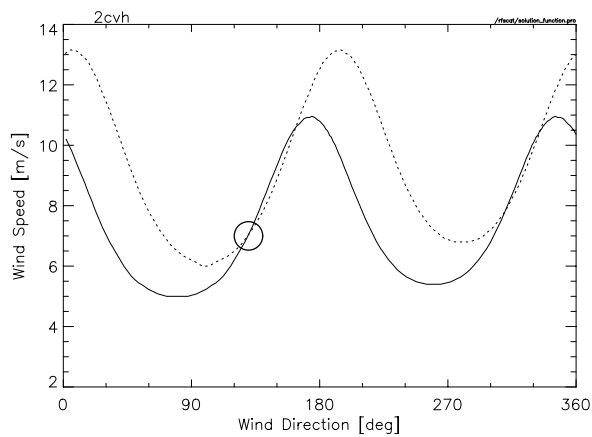
(b)



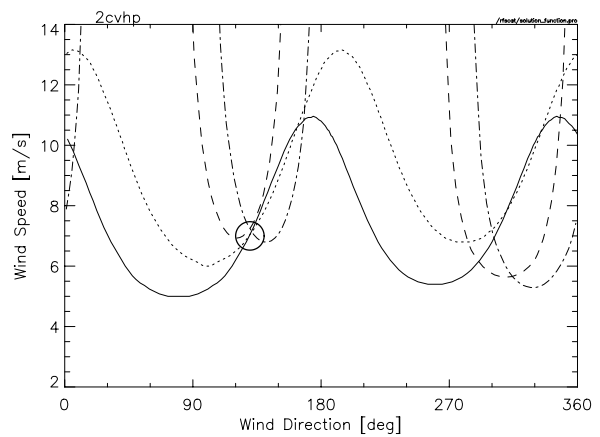
(c)



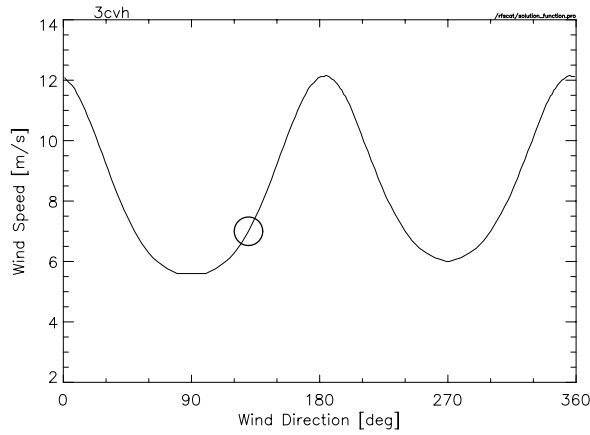
(d)



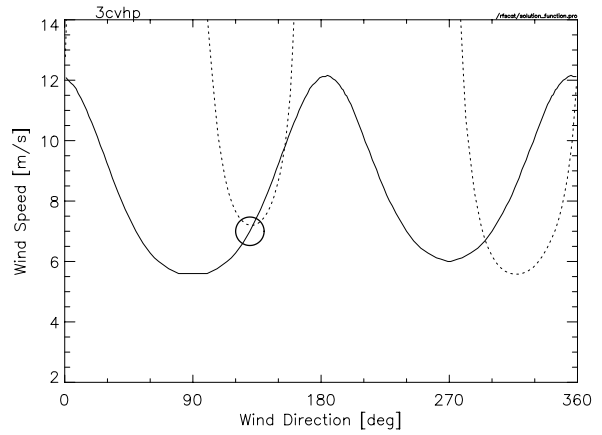
(e)



(f)

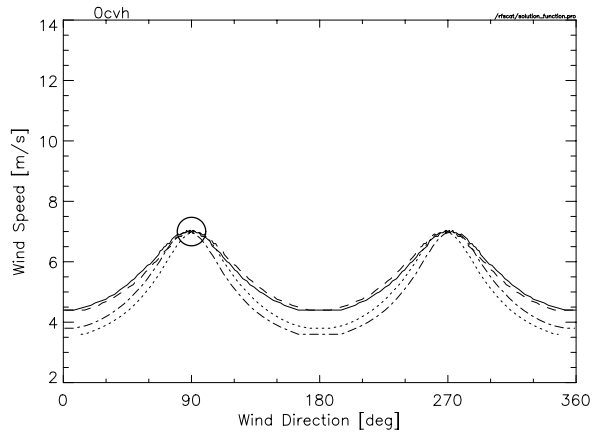


(g)

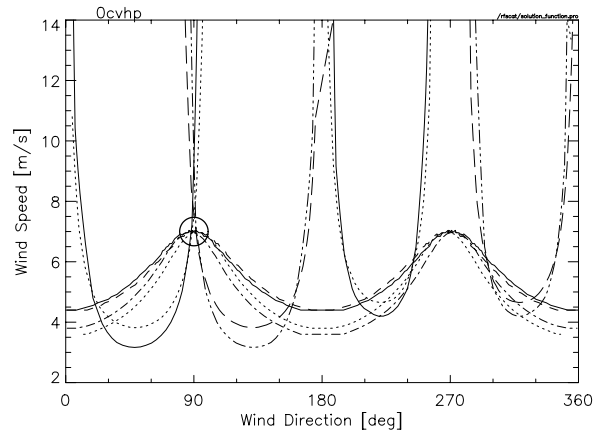


(h)

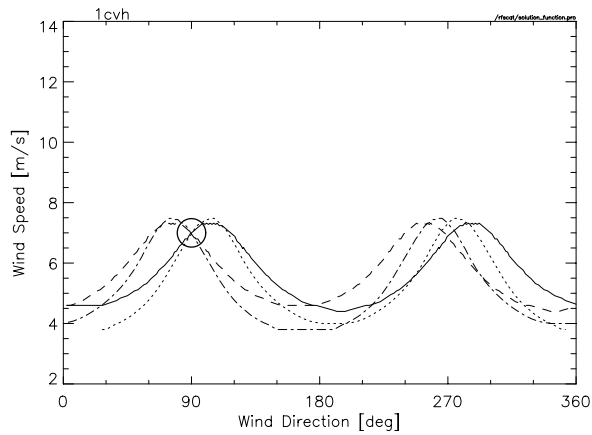
Figure 4.31: Dual beam RFSCAT. Solution functions for ground track, 50 besides ground track, 50 km inside swath edge, and at the swath edge (from top to bottom). In the left column the inner beam has HH-polarisation and 25 degrees incidence angle and the outer VV- polarisation and 55 degrees incidence angle. In the right column both beams are enhanced to semi-polarimetric measurements either HH & HV or VV & VH. The wind speed is 7 m/s and the direction w.r.t ground track is 140 degrees.



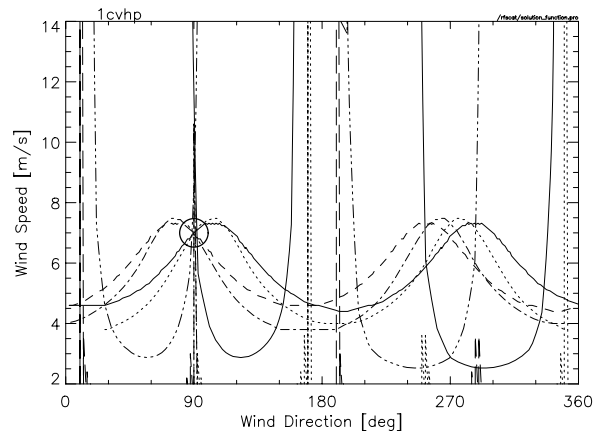
(a)



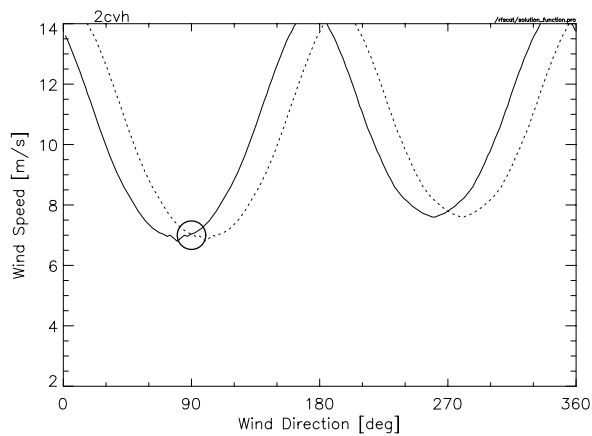
(b)



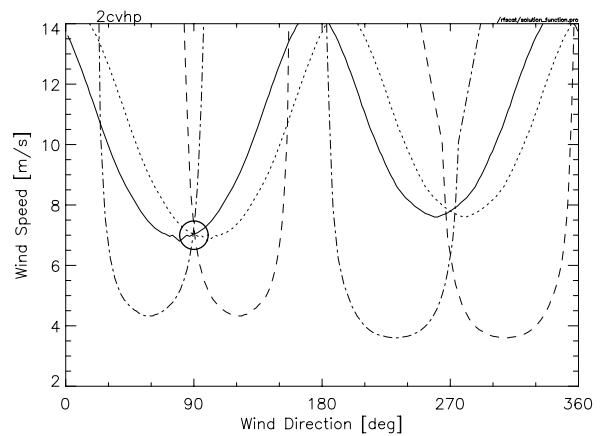
(c)



(d)



(e)



(f)

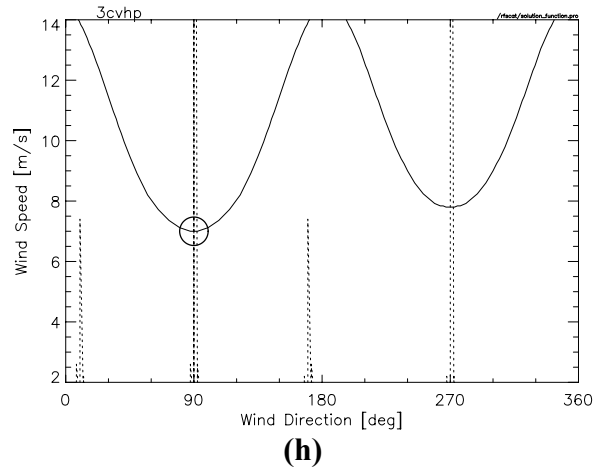
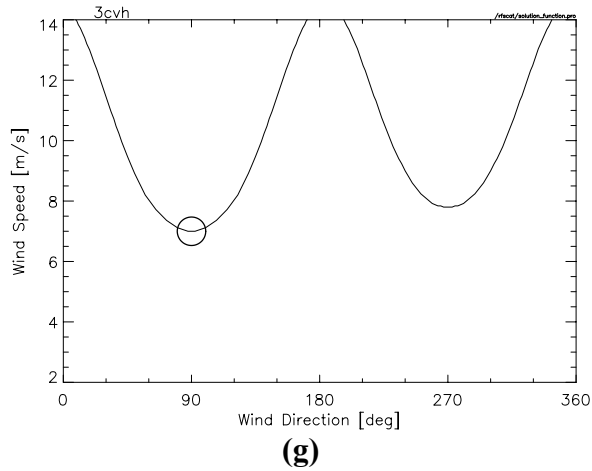


Figure 4.32: Same as Figure 4.31 but for a wind direction of 90 degrees w.r.t ground track.

5. Discussion on Critical Issues in Simulation Tool Development

This section is included as an introduction to Task 2, i.e., to define the scope and overall scope of the simulation tool. The objectives of the simulation tool are

To carry out parametric analysis of the scatterometer

Optimization of system/instrument parameters

The optimization is done with respect to

Scatterometer system performance:

- System sensitivity
- Calibration and accuracy
- Power consumption, mass and cost

Wind retrieval performance:

- Wind speed accuracy
- Wind direction and ambiguity removal
- Spatial resolution and coverage

Overall simulation tool block diagram is shown in Figure 5.1. Critical issues associated with each simulation modules are discussed below.

Simulation scenario definition and simulation input data set

Wind Field Scenario Model:

- Function: defines the wind scenario to be studied
- Input: - wind velocity vectors for each element of surface area used in simulation run
- Output: - wind vector

Discussion:

Measurement geometry: Satellite orbit, subsatellite track position in relation to input data set area.

Type of data set to be used: measured or synthetic data (model based) and list of parameters defined in the data set; position coordinate, wind vector, temperature, sea state (?), NRCS (?) etc.,

Extent of area covered and pixel resolution; local area or global

Number, size and format of the data sets.

GMF:

- Function: generate surface NRCS σ^0
- Input: - wind speed and direction with respect to antenna orientation
- incidence angle
- polarisation
- Output: - NRCS
- Discussion:

NRCS generated is under ideal condition (i.e., no noise) and it is regarded as the “true NRCS”.

GMF for dual frequency and polarimetric cases;

Geophysical Noise:

- Function: generate random variables to represent additional noise due to geophysical effects for specified elements of surface area used in simulation run
- Parameters: - sub-resolution wind variability
- sea state
- surface slicks
- water vapour (rain)

Discussion : How is it modelled ?

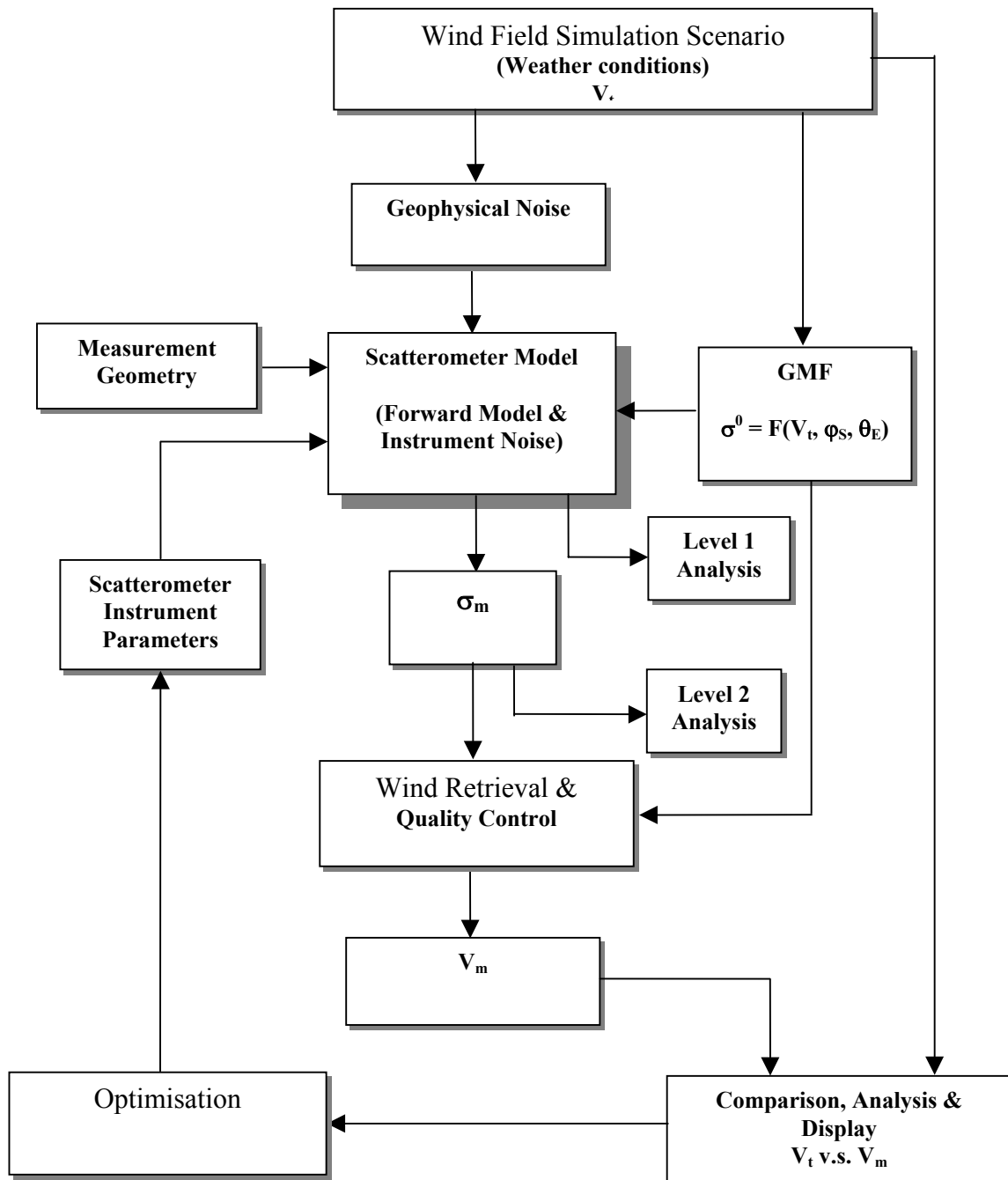


Figure 5.1: Overall approach for simulation Methodology.

Measurement Geometry Model:

- Function: define satellite orbital parameters and relevant earth geometry
- Input:
- satellite position
 - antenna rotation
 - satellite altitude
 - orbit / repeat cycle
 - inclination
 - satellite speed
 - antenna azimuth angle
- Output:
- ground target position
 - incidence angle
 - slant range
 - swath width
 - footprint length
 - return signal time delay
 - Doppler shift / spread of the radar echo

Instrument Parameter Model:

- Function: contains all instrument parameters
- Parameter:
- transmit RF power
 - transmit pulse width
 - transmit modulation
 - carrier frequency
 - antenna scan rate
 - antenna beam width, gain
 - antenna polarisation
 - pulse bandwidth
 - pulse compression ratio
 - pulse repetition frequency (PRF)
 - N_{range}
 - N_{azimuth}
 - receive noise figure
 - receive filtering
 - external noise power
 - resolution
 - Calibration: instrument drift & bias
 - signal detection
 - look averaging

Scatterometer Model:

Function: simulate the determination of earth surface σ_m as function of surface position and satellite position

Input:

- σ^0
- Geophysical noise
- measurement geometry
- instrument parameters
- system noise

Output:

- σ_m for each resolution cell on the surface
- spatial resolution
- radiometric resolution

Discussion:

The most critical aspect is realistic modelling of sources of errors whose effects are reflected in the realistic measured σ_m . It includes geophysical noise, instrument noises (or sensitivity), Doppler compensation error (and other radar signal processing errors) and calibration accuracy, and spacecraft attitude/antenna pointing errors.

Level of simulation: no video signal level signal processing will be included. It will be based on radar equation in conjunction with analytical modelling of noise and errors. Geophysical noise and spacecraft attitude/antenna pointing errors will be modelled as gamma distributed noise with bias on σ^0 (true NRCS). Doppler compensation error will be included in range determination, and SNR and calibration error reflected in measured power variance and bias respectively.

Level 1 Analysis:

Function: analysis of the signal to noise ratio (SNR) and radiometric resolution distribution as a function of geometry

Description: analysis of SNR in each resolution cell for one look while varying azimuth angle and incidence angle (slant range), and resulting radiometric resolution.

Level 2 Analysis:

Function: analysis of σ_m distribution

Description: analysis of σ_m in each resolution cell while varying azimuth angle, incidence angle (slant range) and system parameters

Wind Retrieval and QC:

- Function: Using measured NRCS perform wind velocity retrieval and ambiguity removal
- Input: Measured NRCS data
- Description: - analysis of σ_m and incidence angle data etc. for multiple samples at each element of surface area and ambiguity removal
- determination of wind vector for each element of surface area

Comparison, Analysis & Display:

- Function: - comparison of input and output wind field
- statistical analysis of the scalar and vector comparisons
- visualisation of the results
- Parameters: - wind field scenario
- wind speed
- wind direction w.r.t ground track
- cell location across swath
- Outputs: - on-screen display and PostScript files of:
- wind field (difference) maps
- x-y plots
- histograms
- statistical parameters, figure of merit

Optimisation Model:

- Functions: sensitivity analysis for measurement geometry and instrument parameters
iterative and interactive fine tuning
- Input: - results from analysis model
- Parameters: - measurement geometry model
- instrument parameter model
- Final output: - optimised scatterometer design

6. Conclusion

As a preparatory activity towards development of a simulation tool of an advanced instrument based rotating fanbeam scatterometer (RFSCAT) concept, a critical review of the scatterometer wind product requirements, preliminary analysis of the scatterometer concept and potential areas of system enhancement has been carried out. Also included is preliminary discussion on critical areas of simulation tool development for the purpose of providing inputs to the further discussions to be done at the Task 1 Review meeting.

The meteorological analysis problem provides clear guidelines on the near-surface wind user requirements that are consistent with those of the WMO (see table 1). Improved coverage of near-surface wind vector data at the quality of a scatterometer is useful. Two avenues of development can be identified.

Obtain global coverage in space and time with a typical coverage of 250 km every 12 hours.

Provide locally in the coastal region high-density observations with a typical coverage of 50 km every 3 hours with a 1-hour delivery.

Physical modelling of the RFSCAT measurements is complicated, as found in the physical modelling of existing scatterometer measurements. Physical models seem useful for a qualitative assessment of the variables that may be important in the interpretation of RFSCAT and in defining a strategy of detecting RFSCAT signals by using alternate polarisations or frequencies. Due to the uncertainty in the physical models, additional statistical modelling of these uncertainties is needed to achieve an accurate quantitative interpretation. In scatterometry statistical analyses provided a useful GMF estimation and wind retrieval (Stoffelen, 1998; Stoffelen, Voorrips, and de Vries, 2000), but only after launch. If alternate polarisation or frequencies are considered, empirical GMF modelling for RFSCAT analogous to existing scatterometers and taking account of non-linear relationships appears as a problem of the same nature and complexity.

Both maximum likelihood estimation and neural network methodologies have been used to retrieve scatterometer GMF, where the former proved more successful. Although there are substantial differences in the fitting procedure, the most critical elements of empirical fitting are the learning cost function, and the data selection procedure (see e.g. Stoffelen, 1998, chapter III). The non-linear aspects of the GMF relationship and the noise properties of the input observations need to be known before a satisfactory result can be obtained.

Also for the inversion of RFSCAT data, the non-linear aspects of the GMF relationship and the noise properties of the RFSCAT observations need to be taken into account carefully, as is being done for existing scatterometer data. For scatterometer data inversion is only solved for the situation where multiple (three or four) measurements are available with varying azimuth and/or polarisation. Azimuth coverage needs to be sufficient to determine the $\cos^2\phi$ dependency, whereas horizontal polarisation on NSCAT and SeaWinds eases the wind direction ambiguity problem. For RFSCAT, the outer and nadir swath parts need careful consideration for sampling improvement, whereas in the parts in between the sampling can be degraded (oversampling).

QC, monitoring, and biases require special attention, since anomalous or biased data can potentially counteract the beneficial effect of many good observations. Overdeterminacy, i.e., the availability of more than two backscatter values for the determination of one wind vector, is crucial for the interpretation and assimilation of data from existing scatterometers.

Inverted RFSCAT data could be compared to and assimilated in weather models. The assimilation of data that depend in a non-linear way on the NWP model state is methodologically not well established. On the other hand, the assimilation of SeaWinds scatterometer measurements is posing very similar challenges and is currently being tackled by KNMI (Stoffelen, Voorrips, and de Vries, 2000).

Regarding the second option mentioned above (coastal mission) and the physical and empirical modelling effort needed, it is noted that coastal regions show much more complex ocean surface characteristics than areas in the open ocean, due to ocean wave interaction with bottom topography and breaking and reflection of waves near the coast line, thereby complicating the modelling. This makes the implementation of the global application of RFSCAT more straightforward than the local application.

Near-surface wind requirements for medium-range global weather prediction seem the easiest to meet with space-borne RFSCAT. Improved analyses in this application have spin-off for many other studies, in particular those related to the earth climate. For example, 15- or 40-year meteorological re-analysis fields are being used intensively by the atmospheric science community. Ocean circulation and wave forecasts would also be improved with RFSCAT, for which very similar spatial and temporal coverage requirements hold. As noted above, for nowcasting of weather or waves more stringent spatial and temporal requirements exist.

The state-of-the-art of wind scatterometry from space is reflected by American K_u -band and European C-band systems. Both systems employ co-polarised measurements of the ocean radar backscatter, and the wind retrieval of both systems suffer significantly from inherent ambiguity problems which is caused by the symmetry in the spectrum of the ocean surface roughness. Thus even a perfect GMF cannot solve the ambiguity problem. The wind retrieval can be improved when combining VV- and HH-polarisation measurements. In order to make maximum use of the differences between the solution curves for VV- and HH-polarisation a very precise estimate of σ°_{VV} and σ°_{HH} is required. This is the point where instrument design becomes important. The requirement for better spatial resolution contradicts the wish of a better σ° estimate. On the other hand a smaller resolution cell will reduce the sub-cell variability and therefore the geophysical noise of the σ° estimate. The trade-off between the precision of the σ° estimate and the instrument resolution can only be specified with the end-to-end simulator at a later stage of this study. The option of a second symmetric beam in order to reduce k_p will be part of this analysis.

The technique of polarimetric measurements is not yet state-of-the-art, but the impact for solving the ambiguity problem is significant when relying on existing polarimetric models. But still the exact azimuthal behaviour of the polarimetric correlation coefficient is not well known. Measured depolarisation ratios exhibit considerable scatter and the dependence on other parameters, e.g. incidence angle, is not clear. Nevertheless conservative estimates of the

depolarisation ratio together with theoretical polarimetric modelling will allow to include this option in the RFSCAT simulator.

A first impact study of the different design options for RFSCAT indicates that an HH-polarisation channel will be the minimum enhancement of the system. The question whether a polarimetric option is feasible can be answered only with the results of the RFSCAT-simulator, especially when considering the low back scattering at cross-polarisation and the related signal to noise problems within the system.

The K_u -band option might support the wind retrieval at low wind speeds. Figure 6.1 depicts the difference in radar backscatter at VV-polarisation between C- and K_u -band. This difference is a strong function of wind speed for wind speed below 10 m/s. Therefore this option should be included in the simulator and its impact on wind retrieval should be studied in detail.

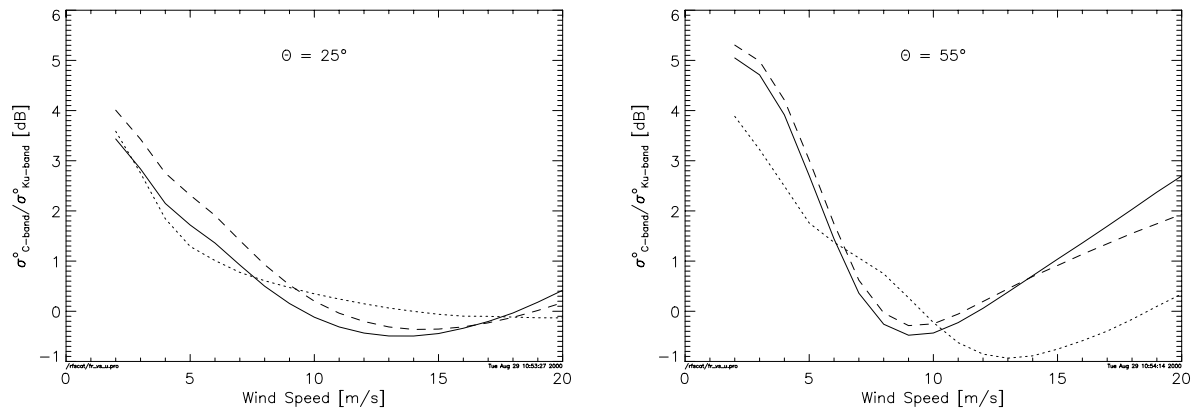


Figure 6.1: Difference between σ_{VV}° for C- and K_u -band as a function of wind speed for 25 and 55 degrees of incidence angle. Solid, dotted and dashed lines for up-, down-, and crosswind direction.

In developing a simulation tool, the most critical issue is properly defining the scope of simulation which is determined by carefully balancing the needs for realistic simulation versus complexity of the simulation modules. A preliminary discussion are given in Section 5. Some of key issues are listed in Table 6.1.

Table 6.1: Critical issues in simulation tool development

Simulation modules	Key issues
Simulation scenario	Open sea, Near coastal region Wind speed range
Input data set	Measured or model based Pixel resolution and spatial extent Dual frequency HH and polarimetric Geophysical noise
GMF	How critical is to use realistic GMF ? Availability or derivation of GMF for different simulation scenarios
Measurement geometry	Number and location of ground scattering cells; entire viewing area or selected sets of local areas Rotating beam geometry; Tx/Rx beam mismatch
Instrument models	Instrument noise and calibration; system noise and SNR, satellite and antenna pointing errors Doppler compensation errors Instrument sensitivity; Radiometric resolution
Retrieval algorithm	Ambiguity removal Quality control procedure
Analysis outputs	Level 1: Analysis at scatterometer output data level; number of samples, incidence and azimuth angle distribution. SNR and radiometric resolution Level 2: Simulated NRCS to be compared with true NRCS Level 3: Retrieved wind vector compared with input wind
Software interface and integration	Format of software modules to be supplied to MPBT; Fortran, IDL

7. References

- Atlas, R., and R.N. Hofman, 1999, The use of satellite surface wind data to improve weather analysis and forecasting, To appear in "Satellites, Oceanography, and Society".
- Attema, E.P.W., A.E. Long, and A.L. Gray, Results of the ESA airborne C-band scatterometer campaigns, Proceedings of the International Geoscience and Remote Sensing Symposium IGARSS'86, Zürich, 8-11. Sept. 1986, ESA Publications Division, SP-254, 1986.
- Cavanié A., An Empirical C-band Backscatter Model over Artic Sea Ice from ERS-1 AMI-Wind Data, Proc. ESA/EUMESTSAT Workshop on Emerging Scatterometer Applications, ESTEC, Noordwijk, The Netherlands, 5-7 Oct. 1998, ESA Publication SP-424, pp 99-106, Nov. 1998
- Courtier et al, 1998, The ECMWF implementation of three dimensional variational assimilation (3D-Var). Part I: Formulation, Quart. J. Royal Meteorol. Soc. 124, 1783-1808.
- Donelan, M.A. and W.J. Pierson, Radar scattering and equilibrium ranges in wind-generated waves with application to scatterometry, Journal of Geophysical Research, Vol. 92, pp. 4971-5029, 1987.
- Donnelly, W.J., J.R. Carswell, and R.E. McIntosh, Revised ocean backscatter models at C and Ku band under high-wind conditions, Journal of Geophysical Research, Vol. 104, No C5, 11,485-11,497, May 15, 1999.
- ESA, Proceedings of the International Workshop POLRAD'96 Polarimetric Radiation Experiment, ESTEC, Noordwijk, The Netherlands, April 29, ESA Publication Division WPP-135, 65-70, 1997.
- ESA, "The nine candidate earth explorer missions: Atmospheric Dynamics Mission", ESA SP1196(4), ESA/ESTEC, Noordwijk, the Netherlands, 1996.
- Figa, J. and A. Stoffelen, On the Assimilation of Ku-Band Scatterometer Winds for Weather Analysis and Forecasting, IEEE Transactions On Geoscience and Remote Sensing, Vol. 38, No.4, 1893-1902, 2000.
- Gade, M., W. Alpers, H. Hühnerfuss, V. Wismann, and P. A. Lange, On the reduction of the radar backscatter by oceanic surface films: scatterometer measurements and their theoretical interpretation, Remote Sensing Environment, 66, 52-70, 1998.
- Guinard, N.W., J. T. Ransone Jr., and J. C. Daley, Variation of the NRCS of the sea with increasing roughness, Journal of Geophysical Research, Vol. 76, 1525-1538. 1971.
- Haskell, A., The ERS-1 programme of the European Space Agency, ESA Journal, 7-1, ESA Scientific and Technical Publications Branch, ESTEC, Noordwijk, The Netherlands, 1983.
- Hauser, D., G. Gaudal, and P. Dubious, Polarimetric wind-scatterometer measurements during POLRAD'96, Proceedings of the International Workshop POLRAD'96 Polarimetric Radiation Experiment, ESTEC, Noordwijk, The Netherlands, April 29, ESA Publication Division WPP-135, 55-64, 1997.
- Hollingsworth, A., and P. Lönnberg, 1986, The statistical structure of short range forecast errors as determined from radiosonde data. Part I: The wind field, Tellus 38A, 111-136.
- Hovanesian, S.A., Radar System Design and Analysis, Artech House Inc., 1984
- IEEE, Special issue on SIR-C/X-SAR, IEEE Transaction on Geoscience and remote sensing, Vol. 33(4), 1995.
- Jones, W.L. and L. C. Schroeder, Radar backscatter from the ocean: Dependence on surface friction velocity, Boundary-Layer Meteorology, Vol. 13, pp. 133-149, 1978.
- Jones, W.L., L. C. Schroeder, and J. L. Mitchell, Aircraft measurements of the microwave scattering signature of the ocean, IEEE Journal of Oceanic Engineering, OE-2(1), 52-61, Jan.1977.
- Isaksen, Lars, and Stoffelen Ad, 2000, IEEE-IGARS special issue on scatterometer applications, in print.
- Keller, W.C., V. Wismann, and W. Alpers, Tower-based measurements of the ocean C band radar backscattering cross section, Journal of Geophysical Research, Vol. 94, 924-930, 1989.

- KNMI, 2000, <http://www.knmi.nl/scatterometer> or <http://www.knmi.nl/~stoffele>.
- Lilley, D. K. and E. L. Petersen, 1983, Aircraft measurements of atmospheric kinetic energy spectra, *Tellus, Ser. A*, 35, 379-382.
- Lin, C.C., Rommen, B., Wilson, J., Peter, P., An analysis of a rotating, range-gated, fanbeam spaceborne scatterometer concept, 2000
- Lin, C.C., Rommen, B. Rotating, range-gated, fanbeam radar – A new spaceborne scatterometer concept, Ocean Winds workshop, Ifremer, Brest, 19-22 June, 2000
- Long, D.G., M.W. Spencer, Radar backscatter measurements accuracy for a spaceborne pencil-beam wind scatterometer with transmit modulation, *IEEE Transactions on Geoscience and Remote Sensing*, Vol. 35, No. 1, pp. 102-114, 1997.
- Lorenc, A.C. , 1988, Optimal non-linear objective analysis, *Q. J. R. Meteorol. Soc.*, 114, 205-240.
- Lorenc, A. C., R. J. Graham, I. Dharssi, B. Mcpherson, N. B. Ingleby and R.W. Lannon, 1992, Study of preparation for the use of Doppler Wind Lidar information in meteorological assimilation systems, Final report on ESA study contract 9063/90.HGE-I, published by U. K. Meteorol. Office, Bracknell, England.
- Le Meur, Didier, Lars Isaksen, and Ad Stoffelen, 1997, Impact of ERS-1/ERS-2 scatterometer tandem on the ECMWF 3D-var assimilation system, Proc. Of the third ERS symposium – space at the service of our environment, Florance, 17-21 March 1997, ESA special report, ESTEC, Noordwijk, the Netherlands
- Masuko, H.K., K. Okamoto, M. Shimada, and S. Niwa, Measurement of microwave backscattering signatures of the ocean surface using X-band and Ka-band airborne scatterometers, *Journal of Geophysical Research*, Vol. 91, 13065-13083, 1986.
- Moore, R.K., and A.K. Fung, Radar determination of winds at sea, *Proc. IEEE*, 67, 1504-1521, 1979.
- MPBT, Proposal for Optimisation of Rotating, range-Gated, Fanbeam Scatterometer for wind Retrieval, MPBT Ref. ER00-003S, 2000
- Nieghem, S.V., S.H. Yueh, R. Kwok, and F.K. Li, Symmetry properties in polarimetric remote sensing, *Radio Science*, Vol. 27, No. 5, 693-711, 1992.
- Plant, W.J. and W. Alpers, An introduction to SAXON-FPN, *Journal of Geophysical Research*, Vol. 99, 9699-9703, 1994a.
- Plant, W.J. and W. Alpers, SAXON-FPN Final Report, Applied Physics Lab. University of Washington, Seattle, 1994b.
- Plant, W.J., A two-scale model of short wind-generated waves and scatterometry, *Journal of Geophysical Research*, Vol. 91, 10735-10749, 1986.
- Romeiser, R., W. Alpers, and V. Wismann, An improved composite surface model for the radar backscattering cross section of the ocean surface 1. Theory of the model and optimisation/validation by scatterometer data, *Journal of Geophysical Research*, Vol. 102, C11, 25237-25250, 1997.
- Schroeder, L.C., W.L. Jones, P.R. Schaffner, and J.L. Mitchell, Flight measurement and analysis of AAFE RADSCAT wind speed signatures of the ocean, *NASA Tech. Memo.*, TM 85646, 144 pp. 1984.
- Snoeij, P., P.J.F. Swart, C.M.H. Unal, Study on the Response of the Radar Echo from the Ocean Surface to the Surface Wind Vector at Frequencies between 1 and 18 GHz, Final report for ESA contract 8722/89/F/FL(SC), Delft University of Technology, 1992a.
- Snoeij, P., E.v. Halsema, J. Vogelzang, S. Waas, S. Zecchetto, H. Jansen, W. Oost, B. Jähne, and Ch. Calkoen, VIERS-1 Final Report Phase 3, Report No. 92-94 Dutch National Remote Sensing Board BCRS, 1992b.
- Spencer, M.W., C.Wu, and D.G. Long, Tradeoffs in the design of a spaceborne scanning pencil beam scatterometer: applications to SeaWinds, *IEEE Transactions on Geoscience and Remote Sensing*, Vol. 35, No. 1, pp. 115-126, 1997.

- Statement of Work, Optimisation of Rotating, Range-gated, Fanbeam Scatterometer for wind Retrievals, ESA, APP-FP/99-10-222/CL/cl, 1999
- Stoffelen, Ad, Aart Voorrips, and John de Vries, 2000, BCRS project report.
- Stoffelen, A. and A. Voorrips, On the Assimilation of QuikSCAT Winds, Contribution to the QuikSCAT cal/val and science meeting, Arcadia, Los Angeles, USA, November 1999.
- Stoffelen, Ad, "Scatterometry", thesis RUU, ISBN 90-393-1708-9, 1998;
<http://pablo.ubu.ruu.nl/~proefsch/01840669/inhoud.htm>.
- Stoffelen, Ad and David Anderson, Scatterometer Data Interpretation: Transfer Function Estimation and Validation, Journal of Geophysical Research, 102(C3), 5767-5780, 1997b.
- Stoffelen, Ad and Paul van Beukering, 1997, "The impact of improved scatterometer winds on HIRLAM analyses and forecasts", BCRS study contract 1.1OP-04, report published by BCRS, Delft, The Netherlands, and HIRLAM technical report #31, published by IMET, Dublin, Ireland.
- Stoffelen, A.C.M. and G.J. Cats, 1991, "The impact of Seasat-A scatterometer data on high-resolution analyses and forecasts: The development of the QEII storm", Monthly Weather Review, Feb. 1991.
- Tsai, W.Y., S.V. Nghiem, J.N. Huddleston, M.W. Spencer, B.W. Stiles, and R.D. West, Polarimetric Scatterometry: A promising technique for improving ocean surface wind measurements from space, IEEE Transactions on Geoscience and Remote Sensing, Vol. 38, No. 4, 1903-1921, 2000.
- Unal, C.M.H., P. Snoeij, and P. J. F. Swart, The polarization-dependent relation between radar backscatter from the ocean surface and surface wind vector at frequencies between 1 and 18 0Hz, IEEE Transactions on Geoscience and Remote Sensing, Vol. 29, no. 4, pp. 621-626, July 1991.
- Ulsby, F.T., Elachi, C., Radar polarimetry for geoscience applications, Editors, Artech House, Inc. 1990
- Wentz, F.J. and D.K. Smith, A model function for the ocean normalized cross section at 14 GHz derived from NSCAT observations, Journal of Geophysical Research, Vol. 104, No. C5, 11499-11507, 1999.
- Wismann, V., HELISCAT – The multi-frequency multi-polarisation helicopterborne scatterometer of the University of Hamburg. Technical Report, 20 pages, 1994a.
- Wismann, V., SIR-C/X-SAR Messungen der Radarsignaturen von Oberflächenfilmen in der Nordsee mit dem HELISCAT der Universität Hamburg, Report to the University of Hamburg, 100 pages, 1994b.
- Wismann, V., Polarimetric Radar Backscatter from the Ocean Surface, Report to the European Space Agency AOP/WK/33591, 1997.
- Wismann, V., Polarimetric Radar Response from the Ocean Surface for Wind Direction Retrieval, Proceedings of the International Workshop POLRAD'96 Polarimetric Radiation Experiment, ESTEC, Noordwijk, The Netherlands, April 29, ESA Publication Division WPP-135, 65-70, 1997.
- Wismann, V., Land Surface monitoring with Spaceborn Scatterometers, Proc. ESA/EUMESTSAT Workshop on Emerging Scatterometer Applications, ESTEC, Noordwijk, The Netherlands, 5-7 Oct. 1998, ESA Publication SP-424, pp 25-31, Nov. 1998
- Wismann, V., Monitoring of seasonal thawing in Siberia with ERS scatterometer data, IEEE Transactions on Geoscience and Remote Sensing, Volume 38, No. 4, 1804-1809, 2000.
- Wismann, V., M. Gade, W. Alpers, and H. Hühnerfuss, Radar signatures of marine mineral oil spills measured by an airborne multi-frequency radar, International Journal of Remote Sensing, Vol. 19, 3607-3623, 1998.
- Wismann, V., M. Gade, W. Alpers, and H. Hühnerfuss, The Radar signatures of mineral oil spills measured by an airborne multi-frequency multi-polarization microwave scatterometer, Proceedings of the OCEANS-93 Conference Engineering in Harmony with Ocean, Oct. 18-21, 1993, Victoria, Canada, Vol. II, 348-353, 1993.
- Yueh, S.H., R. Kwok, and S.V. Nghiem, Polarimetric scattering and emission properties of targets with reflection symmetry, Radio Science, Vol. 29, No. 6, 1409-1420, 1994.

8. Acronyms

ADEOS	Advanced Earth Observation Satellite
ASCAT	Advanced ESA C-band scatterometer
C-band	Radar wavelength at about 5 cm
CLIVAR	Programme on Climate Variability
ECMWF	European Centre for Medium-range Weather Forecasts
ENSO	El Niño Southern Oscillation
EPS	EUMETSAT Polar System
ERA	ECMWF Re-analysis
ERS	European Remote-sensing Satellite
ESA	European Space Agency
EUMETSAT	European organisation for Meteorological Satellites
GCM	General atmospheric Circulation Model
GCOS	Global Climate Observing System
GMF	Geophysical Model Function
GOS	Global Observing System
GOOS	Global Ocean Observing System
GSFC	Goddard Space Flight Center
KNMI	Royal Netherlands Meteorological Institute
Ku-band	Radar wavelength at about 2 cm
LOS	Line Of Sight
METOP	Future European meteorological polar orbiting satellite
NCEP	National Center for Environmental Prediction (USA)
NSCAT	NASA fan-beam Ku-band scatterometer on ADEOS-I
NWP	Numerical Weather Prediction
QC	Quality Control
QuikSCAT	NASA dedicated SeaWinds scatterometer mission
RFSCAT	Rotating Fan Beam Scatterometer
RMS	Root Mean Square
SATOB	WMO code for cloud motion wind satellite observation
SCAT	ESA C-band scatterometer on ERS
SeaWinds	NASA conical pencil-beam Ku-band scatterometer

SSM/I	Special Sensor Microwave / Imager
TEMP	WMO code for conventional wind, temperature and humidity sounding
TOVS	TIROS-N Operational Vertical Sounder
USA	United States of America
WMO	World Meteorological Organisation
WWB/E	Westerly Wind Burst / Events
4D-var	Four dimensional variational assimilation